STUDIES OF COMBUSTION AND CREVICE GAS MOTION

IN A FLOW-VISUALIZATION SPARK-IGNITION ENGINE

by

MEHDI NAMAZIAN

B.S., Tehran University, Iran
(1975)

M.S., Massachusetts Institute of Technology
(1977)

SUBMITTED IN PARTIAL FULFILLMENT
OF THE REQUIREMENTS FOR THE
DEGREE OF

DOCTOR OF PHILOSOPHY

at the

MASSACHUSETTS INSTITUTE OF TECHNOLOGY

February 1981

Signature of Author_____
Department of Mechanical Engineering
February , 1981

Certified by_____
John B. Heywood
Thesis Supervisor

Accepted by_____
Warren M. Rohsenow
Chairman, Department Graduate Committee

STUDIES OF COMBUSTION AND CREVICE GAS MOTION
IN A FLOW-VISUALIZATION SPARK-IGNITION ENGINE

by

Mehdi Namazian

Submitted to the Department of Mechanical Engineering on January 28, 1981 in partial fulfillment of the requirements for the Degree of Doctor of Philosophy.

ABSTRACT

The flow field through the entire operating cycle of a spark-ignition engine has been studied, using a square cross-section cylinder engine with two parallel quartz glass walls which permit optical access to the entire cylinder volume. Schlieren short-time exposure photographs and high speed movies were taken to define the details of the flow. Many of the flow features during intake, compression, combustion, expansion and exhaust were observed.

The combustion process was studied more extensively. Details of ignition, flame propagation, and the extent of cycle-by-cycle variations are presented. It is shown that the flame zone is thick, the front-to-back distance being 10-15 mm, and is expected to contain unburned fuel.

During expansion, a jet-like flow is observed emanating from the piston top land crevice. The top land crevice and the regions behind and between the rings are connected through ring gaps. A system model of orifices and volumes was developed to describe the observed jet-like flow. It is concluded that this jet is the flow through the ring gap. In addition, the model predicts that some of the gas trapped in the top land crevice should expand into the combustion chamber prior to the appearance of the jet-like flow through the ring gap. It is believed that this expanding gas flow may remain close to the wall because it leaves the crevice at low velocity and it is obscured from observation by the thick dark thermal boundary layer on the wall. This expanding gas flow was observed with a simulated top land

crevice removed from the wall, and hence from the obscuring thermal boundary layer.

The flow model was coupled with a ring motion model and extended to a real engine geometry. This model predicts the amount of unburned fuel trapped in the crevice regions, and calculates the portion of this trapped unburned fuel that is lost to the crankcase and the portion that returns to the combustion chamber. The significance of this trapped unburned fuel in regards to fuel economy and hydrocarbon emissions is discussed. The effect of ring gap area, volume of the crevice regions, wall temperature, load and piston speed on the amount of unburned fuel returning to the combustion chamber is related to exhaust hydrocarbon emission trends.

Thesis Supervisor: John B. Heywood
                Title: Professor of Mechanical Engineering
                        Director, Sloan Automotive Laboratory

To my love, Nikoo

THIS PAGE WAS INTENTIONALLY LEFT BLANK

ACKNOWLEDGMENTS

Mehdi Namazian
February, 1981

THIS PAGE WAS INTENTIONALLY LEFT BLANK

TABLE OF CONTENTS

THIS PAGE WAS INTENTIONALLY LEFT BLANK

LIST OF TABLES

THIS PAGE WAS INTENTIONALLY LEFT BLANK

LIST OF FIGURES

CHAPTER 1

INTRODUCTION

1.1 Scope of This Study

This thesis reports on the flow field in the combustion chamber of a spark-ignition engine. A flow-visualization engine was used to observe the flow through the entire operating cycle of the engine. The primary scope of this study was to visualize those aspects of the flow which relates to the formation of hydrocarbon emissions [1], e.g.: flows from the top land crevice (the crevice between the piston crown and cylinder wall is believed to be a significant source of unburned hydrocarbon); the entrainment of the layers off the cylinder head and cylinder wall during exhaust stroke; the vortex roll up in the piston-crown-surface, cylinder-wall corner during exhaust stroke. Another important goal of this study was to observe the flame development process from the spark-discharge through establishment of a stable flame kernel and growth to a fully-developed turbulent flame structure. An additional

goal was to identify within an operating engine cylinder the rotational motions set up by intake stroke, which were observed by Ekchian and Hoult [2] in a study of a water-analog of the flow into the cylinder.

The flow-visualization engine used for this study has a square cross section piston-cylinder with two parallel quartz windows. Schlieren short-time exposure photographs and high speed movies were taken to define the details of the flow. Descriptive and quantitative models of the motion of the flow are given. The flow into the crevice regions caused by piston-cylinder-rings of the flow-visualization engine is studied more extensively. The flow model is coupled with a ring motion model and extended to a real engine geometry. This model predicts the amount of unburned fuel trapped in the crevice regions and calculates the portion of this trapped unburned fuel that is lost to blowby and the portion that returns to the combustion chamber. The significance of this trapped, unburned fuel in regard to fuel economy and hydrocarbon emissions is discussed.

1.2 Background

1.2.1 Background on visualization study

Visualization of the flow in a practical device is a powerful technique for developing conceptual models for the important physical processes. The geometry of conventional internal combustion engines—circular cross-section cylinder, complex combustion chamber shape, valves, spark plug, fuel injector in the cylinder head—makes complete flow visualization extremely difficult. Nonetheless, there is a long and productive record of such efforts.

Examples of such experiments are the following. In spark-ignition engines: Rassweiler and Withrow [3] used high speed movies of the flame taken through a quartz cylinder head to determine flame front location and correlate volume enflamed with cylinder pressure records. A recent example of the use of high speed color movies to examine flame front location and structure is the excellent work of Nakanishi, et al. [4] with an L-head engine with a flat quartz cylinder head. In diesel engines Alcock and Scott [5] have pioneered the use of high speed color movies, taken through windows in the cylinder head, to define details of the engine combustion process with realistic engine geometries and operating conditions.

To obtain details of the flow field in addition to that provided by direct radiation from the flame front, visualization techniques such as Schlieren must be used, which respond to refractive index gradients in the flow that result from density gradients. However, optical access on both sides of the region observed must be provided. In rapid compression machines, designed to simulate certain aspects of an operating engine, this has been achieved. Taylor, et al. [6] with a piston in a circular-cylinder rapid compression machine used Schlieren photographs to study flame propagation and autoignition. The disc-shaped combustion chamber was viewed along the cylinder axis through a transparent flat cylinder head (which had no valves), and a mirror was placed on the piston. A similar approach was used recently by Matekunas [7]. Oppenheim, et al. [8], and Ishikawa and Daily [9] also in a rapid compression machine, used a square cross-section "cylinder" with two quartz walls to view the cylinder contents at right angles to the cylinder axis to obtain Schlieren movies of the flow.

Schlieren photographs and movies have been taken in an operating spark-ignition engine by Iinuma and Iba [10], [11]. To achieve the required optical access, an L-head engine was used, and a long rectangular slot combustion

chamber was designed into the cylinder head to permit observations perpendicular to the cylinder axis and centerline of the cylinder head.

Significant contributions have been made by these and other engine-related visualization studies. The following difficulties have yet to be resolved, however. Conventional photography, which presents the least difficult optical access problems, only determines the shape and location of the flame front. Rapid compression machines cannot fully simulate the intake and exhaust processes, nor the timing of events in the engine operating cycle. Full access for Schlieren in a conventional circular cross-section cylinder overhead-valve engine is not feasible.

At M.I.T. in the Sloan Automotive Laboratory a new flow-visualization spark-ignition engine was designed to resolve the above difficulties. The engine was designed and partially built by S. Hansen [12]. This engine was designed to operate for several consecutive cycles. The Schlieren technique was chosen as the best means available for flow visualization during both combustion and non-burning parts of the cycle. To provide the necessary optical access, a square cross-section cylinder was chosen, with two parallel glass side walls and two parallel metal side walls. This permitted a conventional cylinder head and

valve geometry to be used. The other aspects of engine design and operation were made as close to conventional practice as feasible.

1.2.2 Background on hydrocarbon emissions

Lean operation of spark ignition engine, at part load, or dilution of the mixture with recycled exhaust is desirable from a fuel economy point of view and for reduced CO and NO_x emissions. Unfortunately, the concentration of unburned fuel pollutants (HC) is higher in the fuel-lean, as well as the fuel-rich region, and dilution of the charge which reduces the level of NO_x significantly, also results in more unburned fuel in the exhaust. The HC emission rise in the lean region and with dilute charge results from incomplete oxidation of the fuel. Hydrocarbon compounds unlike other exhaust products, are formed principally in the quench regions of the combustion chamber. Daniel [13] was the first to demonstrate the existence of a quench layer on the combustion chamber surfaces. By a photographic technique, he observed a decrease in flame laminosity close to the wall. As the flame propagates toward the chamber wall, removal of heat and the disruption of chemical processes quench the flame. The thickness of this quench layer, which covers the cylinder head, cylinder wall and

piston crown depends on the engine operating conditions, at the time of quenching and can vary from hundredths to tenths of a millimeter.

For many years the quench layers on the combustion surfaces were considered to be an important source of hydrocarbon emissions and extensive research was performed concerning the flame quenching distance associated with cool surfaces. However, the recent theoretical works of A. Adamczyk et al. [14] and C. Westbrook et al. [15] predict virtually complete oxidation of the quench layer hydrocarbon due to the post flame oxidation. Fast sampling experiments of J. LoRusso et al. [16] and P. Weiss, J. Keck [17] supported these predictions. These predictions are also confirmed by the experiments performed in the combustion bombs having very small crevice volumes [18,19,20].

Other sources of unburned fuel are crevices in the combustion chamber which are too narrow for the flame to enter. The flame is quenched by heat transfer to the cold wall at the crevice entrance. The volume between the piston and cylinder wall above the top piston ring, known as top land crevice, is the most important crevice in the engine. Tabaczynski et al. [21] propose that the top land crevice gas expands out of this crevice and is laid along the cylinder walls. In the exhaust stroke this layer is scraped

off the wall and rolled into a vortex. This vortex is considered to entrain into the exhaust port at the end of exhaust stroke. Time-resolved HC measurements in the exhaust port [21,22,23] support this idea by showing a peak in the hydrocarbon level at the end of the exhaust stroke.

Other potential sources of hydrocarbon are oil layers containing absorbed fuel [24] and bulk quenching in the burned gas [25]. K. Goto et al. [26] show that the HC concentration increases when maximum combustion pressure becomes low. The low combustion pressure is an indication of incomplete combustion.

The relative importance of crevice regions is evident from the experiments of Wentworth [27] who reports 47-74% reduction of hydrocarbon emissions when the top land crevice is virtually eliminated. The sampling of the gas in the piston top land crevice was performed by Furuhama [28] and the results prove that the flame does not reach the combustible gas mixture in this crevice region.

A major part of this thesis is devoted to studying the flow in and out of the crevice regions in the combustion chamber. Besides the top land crevice, other crevice regions created by piston rings are also considered.

1.3 Layout of Thesis

After this introductory chapter the experimental setup is described in Chapter 2. The engine design, Schlieren system and photographic technique, operating procedure and test conditons and finally engine performance are described in this chapter.

In Chapter 3 all the in-cylinder processes, i.e., intake, compresssion, combustion, expansion and exhaust are discussed. Prints of photographs which illustrate important features of each process are presented. The key features observed from these photographs are described and where feasible a quantitative interpretation is given.

In Chapter 4 a detailed study of the combustion process is illustrated. The flame structure, ignition, establishment of a stable flame kernel, and finally the effect of gas motion on the flame and hence on the cycle-by-cycle variation are discussed.

In Chapter 5 the flow into and out of the crevice regions of the transparent engine is discussed. A model is presented which describes the observed flows.

In Chapter 6 the flow model for the crevice regions of the transparent engine is extended to a real engine. A ring motion model is coupled with the flow model to provide the flow passages in a real engine. The model is verified by comparing the experimental data on blowby with the predicted ones. Finally, the model is used to study the variation of the mass flow of unburned fuel from crevice regions with geometry, piston speed, load and wall temperature. Experimental data are used to verify the trends predicted by the model.

CHAPTER 2

EXPERIMENTAL SETUP AND OPERATION

2.1 Engine Design

The transparent engine is designed to allow complete visualization of the various processes in the combustion chamber of a four-stroke spark-ignition engine. A removable head, Cooperative Fuel Research (CFR), engine is used as a basis for the new engine. As shown in Figure 2.1, the completed visualization engine uses the crankcase and internal parts of the CFR engine as its lower half. The CFR engine is split between the cylinder and head, and the existing CFR piston and cylinder act as a type of crosshead. The new portion of the visualization engine is the square cross-section assembly, positioned as shown in the figure.

The square piston is attached to the CFR piston below by a connecting rod through a hole in the adaptor base plate. The adaptor base plate mounts the square cylinder assembly to the CFR cylinder. The base plate is sealed to the connecting rod with a felt seal to prevent oil from

passing up from the crankcase to the square assembly. To avoid compression above the CFR piston, a 10 mm diameter hole was drilled through the CFR piston crown.

The original CFR engine cylinder-head, valves, and valve mechanism are used on top of the square cross-section assembly. The valves are activated from the camshaft of the base CFR engine by elongated push rods. Use of the original head and valve mechanism allows the standard valve dimensions and lift to be used, thereby assuring realistic inlet and exhaust flows.

Figure 2.2 shows additional aspects of the construction, and geometric details of the square cross-section transparent cylinder assembly are given in Table 2.1. Table 2.2 compares the geometry of a typical conventional engine with that of the transparent engine.

The square cylinder is comprised of two parallel steel walls and two parallel quartz glass walls. The glass walls are attached to the cylinder by means of steel walls (see Fig 2.3). Silicon rubber gaskets, 0.38 mm thick, are used at the interfaces of glass and steel to avoid contact between the two surfaces and to prevent gas leakage. Two steel spacers, 0.5 mm thicker than the glass walls, are placed on either side of the glass side walls to obtain 35

percent compression of the gaskets and also to avoid uneven loading of the glass during assembly.

The piston is made from two separate pieces of aluminum. The crown bolts onto the main piston and ring assembly to allow compression ratio changes to be made easily. Details of the piston and ring designs are shown in Fig 2.4. Three sets of "rings," which operate without lubrication, provide the gas seal. The rings overlap at the corners to minimize the effective area of the gas leakage path. Several ring materials were tested: two types of graphites, pure Teflon, graphite filled Teflon, and polymer filled Teflon (RULON J). A hard graphite (ATJ) was found the most effective material for keeping the windows clean and free of any film which produces optical interference over a reasonable engine operating period. Each ring segment is pressed against the cylinder walls by two 6 mm diameter coil springs.

The cavity within the square cross-section assembly below the piston is vented to the atmosphere to prevent significant compression above the adapter base plate.

An air surge tank is used to damp out the intake flow pulses and permit an orifice plate to be used upstream of the surge tank to measure air flow rate. The fuel, propane

in this study, is fed from the fuel tank through a regulator, rotometer flowmeter, control valve, and solenoid shutoff valve to an atomizing nozzle in a fuel-air mixing tank. The mixing tank is jacketed and can be steam-heated to vary the inlet mixture temperature.

A "MOBELEC" capacitor discharge electronic system is used for ignition.

A Star dynamometer is mounted next to the engine, coupled to the engine via a toothed belt and pulleys system. Speed is controlled by variable resistors. The dynamometer has a standard hydraulic scale and manometer to obtain brake and friction torque readings.

The inlet mixture temperature is measured with a thermocouple in the intake manifold 50 mm upstream of the inlet valve. The inlet system pressure is measured with a mercury manometer connected to the mixing tank.

The pressure in the combustion chamber is measured by an AVL pressure transducer, which is mounted flush with the steel cylinder wall, 15 mm below the cylinder head. A pulse generator is mounted on the half speed shaft, which generates one pulse every crank angle degree. The pressure transducer signal is sampled every degree and the data stored on the laboratory computer, a DEC PDP-11/10.

2.2 Schlieren System and Photographic Technique

The Schlieren technique was chosen for flow visualization. This technique is based on the principle of refraction of the light beam from its original direction by an angle proportional to the gradient of the index of refraction normal to the light path. The index of refraction gradient results from and is proportional to the density gradient in the test section [29]. The Schlieren system used is of the Z type configuration. It consists of two spherical and two flat mirrors, a point source, and knife edge as shown in Fig 2.5. Light from the point source is collimated by the first spherical mirror, and passed through the flow field. The image of the light source is then brought to focus on the knife edge by the second spherical mirror, and is recorded with a camera. The recorded image will appear uniform if there are no density gradients in the test section. Conversely, if local density gradients are present, the light will refract and will be intercepted by the knife edge, and hence the recorded image will contain corresponding local changes in illumination. The knife edge used is a circular aperture that provides sensitivity in all directions; sensitivity being a measure of change in local illumination of the image for a given local density gradient in the test section.

Two types of photographs have been taken: still pictures and high-speed movies. The still pictures are taken with a microflash unit with a 549-11-11 EG and G point source. The flash is triggered by a micro-circuit at a preset crank angle and lasts a fraction of a microsecond. Before the flash is triggered, the circuit triggers the scope and computer to record the pressure trace for the cycle when the picture is taken. A Polaroid camera with a one meter focal length optically corrected lens is used. The 100 mm by 125 mm pictures obtained are very sharp due to the short duration and high intensity of the light source and the large depth of field of the camera lens. The movies are taken with a 16 mm Hycam camera capable of speeds up to 9000 frames per second. A continuous light source is used with a 1/10 speed shutter in the camera to control the exposure of each frame.

2.3 Operating Procedure and Test Conditions

Because the square assembly and cylinder-heat are not water cooled, the engine was only fired for short periods. Checks were always made first, during motored operation, to ensure that there was no external leakage past the glass wall seals (using soap solution) and that the internal leakage past the piston rings (using PV^{γ} curves and peak

pressure location obtained from the pressure transducer data) was negligible.

In addition, some Schlieren movies were also taken of the region below the piston during firing to check whether flow past the piston rings was visible. No flow was detected up to 120 degrees after TC, when the clamping plates obscured the bottom of the piston.

The operating procedure is as follows. The engine is motored at preset operating conditions and the above checks made. The fuel is turned on for at least 15 seconds to assure a homogeneous mixture in the air-fuel mixing tank. For still pictures the spark is then turned on and the engine permitted to fire for about 10 cycles before the timing sequence for recording the pressure data for the particular cycle under study, and the flash unit (set at a previously chosen crank angle) is initiated. For Schlieren movies one motored cycle was filmed and its pressure data was recorded at the start of the filming process to provide a reference. The spark was then switched on automatically, and about 16 additional cycles were filmed and the pressure data recorded. Timing markers on the film permitted the film and pressure data to be synchronized. A mass fraction burned analysis was carried out for each run (see following section). The engine operating conditions are given in

Table 2.3. A part-load condition was selected to avoid higher than necessary pressure conditions during firing. A slightly rich-of-stoichiometric mixture was used to avoid misfiring due to low compression pressures.

2.4 Engine Performance

An existing computer code [30] was used to obtain mass fraction burned curves from measured cylinder pressure data. The assumptions made in the thermodynamic model used for this purpose were: frozen composition for the unburned mixture; equilibrium composition for the burned mixture; ideal gas behavior for each component species in these mixtures; heat transfer predicted by Nusselt-Reynolds No. correlation; negligible volume for the actual reaction zone in the flame.

Figure 2.6a shows measured cylinder pressure traces from six consecutive cycles; the first firing cycle after motoring is the one with the highest peak pressure, followed by the cycle with the second highest peak pressure, after which the engine stabilizes. The standard deviation in peak pressure is 1 atm, which is about 10 percent of the mean peak pressure of 9.7 atm. This deviation is larger than normal engine values. Also, occasional partial-burn and misfire cycles were observed, both from pressure traces and

the Schlieren movies. The calculated mass fraction burned profiles corresponding to Fig 2.6a are shown in Fig 2.6b. The mass fraction burned curves show a standard deviation in X_{max} , the maximum predicted mass fraction burned, of 0.03. The mean value is 0.90 which, when allowance is made for quenching and blowby, is at the expected level.

In selecting cycles for analysis only those cycles which showed normal burning characteristics and had peak pressures at about 17 degrees after TC (typical of MBT timing) were used.

THIS PAGE WAS INTENTIONALLY LEFT BLANK

CHAPTER 3

DESCRIPTION AND ANALYSIS OF IN-CYLINDER PROCESSESS

In this section we present prints of the photographs which illustrate important features of the flow inside the cylinder during the complete engine cycle. The key features observed from these photographs (and discernible from viewing the movies) are described and, where feasible, given a quantitative interpretation.

3.1 Intake Process

Figure 3.1 shows six photographs taken at different crank angles during the intake process. The crank angle and pressure in the cylinder for each picture are shown in Fig 3.2. Figure 3.1a, which was taken at 30 degrees ATC, does not show any flow into the chamber even though the inlet valve nominally opens at 10 degrees after TC. But 5 degrees later, Fig 3.1b, at 35 degrees after TC, a clearly delineated front is seen as the fresh charge enters the cylinder volume. Pictures c, d, and e, taken at 36 degrees,

39 degrees, and 41 degrees after TC, indicate the trajectory of the inlet jet until it reaches the cylinder wall. The velocity of leading edge of the jet is about 23 m/s. Fig 3.1f shows the jet when it is fully developed.

The intake valve opens at 10 degrees after TC but the jet always appears slightly later than 30 degrees after TC for these conditions. The pressure trace during the intake process, Fig 3.2 , explains this delay. Since the engine is throttled, following inlet valve opening the pressure in the chamber decreases from the exhaust system pressure to the intake system pressure over an interval of about 20 degrees. During this period when the cylinder pressure is higher than that of the intake manifold, a back flow into the intake occurs. This back flow was observed in the movies. As the intake valve opens, the back flow is slight and involves only the gas around the valve. But as the valve continues to open further, the bulk of the gas in the cylinder which was following the intake-stroke piston motion down the cyinder is drawn towards the intake valve. This takes place close to 24 degrees after TC.

As the intake jet develops, a downward flow close to the cylinder wall below the point the jet impinges on the wall can be observed in the Schlieren movies. Above the jet impingement point, a vortex flow in the top left and right

hand corners of the combustion chambers, shown schematically in Fig 3.3, can be observed. These vortices are present through the intake process and persist during compression. Ekchian and Hoult [2] have previously demonstrated the existance of the vortex in the top corner of the cylinder in water analog intake flow studies. They also showed that a large vortex flow was set up below the valve in the bulk of the cylinder. We did not observe this lower vortex in these experiments. This does not necessarily say such flows are not present; the flow beneath the valve was difficult to discern in our current movies.

Another phenomenon observed during the start of intake is the flow of gas out of the piston top land into the cylinder. It is best visualized on the right hand side piston cylinder-wall crevice of the pictures of Fig 3.1. The right hand side flow is more visible because of the larger crevice on that side. The left crevice is smaller than the dark layer on the combustion chamber wall, interpreted as thermal boundary layer. This layer therefore obscures the flow out of the left crevice. Part of left side crevice flow can be seen in Fig 3.1a. The flow out of the crevice occurs because the gas expands into the cylinder as the cylinder pressure decreases following intake valve opening. This expansion starts at around 24 degrees after

TC. As discussed above, at this time the bulk gas moves towards the intake valve as a backflow. The flow out of the crevice is laminar (Reynolds number is 250 based on piston velocity at 60 degrees after TC and hydraulic diameter of the crevice).

During intake this crevice flow probably has little significance. During the expansion stroke a similar crevice flow is expected, which is likely to be important in the hydrocarbon emission mechanism as discussed later.

3.2 Compression Process

At the beginning of the compression stroke, the gas motion is difficult to discern due to the lack of density gradients in the bulk gas with which to identify the fluid motion. As the piston moves up during the compression stroke, a marble-like structure becomes apparent in the Schlieren pictures, which helps visualize the flow. Halfway through the compression stroke, top corner vortices can be observed in the Schlieren movies as sketched in Fig 3.4. This vortex is the one set up by the intake jet as explained in the previous section which persists through the compression and combustion processes. The flow in the upper right corner of the cylinder influences the flame development in the vicinity of the spark plug, and the flow

in the upper left corner influences the motion of the fully developed flame as discussed in Chapter 4.

During the compression stroke no vortex was observed in the corner of the piston crown and the cylinder walls, although such vortices have been visualized in rapid compression machines in which the gas was compressed from rest [8,9].

3.3 Combustion Process

Figure 3.5 shows a set of photographs of the entire combustion process for one typical operating cycle from a movie. Following the spark discharge at 55 BTC, a flame kernel develops at the spark plug at the upper right corner of the combustion chamber, rapidly (within about 3 degrees) assumes a turbulent flame structure, propagates as a roughly spherical flame front until the front intersects the right cylinder wall and the piston, and eventually (after Fig 3.5i) shows fully burned gas filling the space between the glass walls behind the flame. There are larger scale (of order 10 mm) and smaller scale (of order 2.5 mm) irregularities to the flame front.

The flow field in the cylinder at the end of compression influences the flame propagation process. The later pictures in the sequence in Fig 3.5 show that flame propagation is influenced by the gas motion which exists in the left side of the cylinder. The bottom half of the flame front, once it is halfway across the piston, starts to move faster than the top part. We believe this motion results from the vortex set up in the upper left corner of the cylinder by the intake jet as described previously. The upper right corner vortex-flow was also observed to affect the motion of the flame in the vicinity of the spark plug. In some cycles (though not the one shown here) the flow detaches the growing flame kernel from the spark plug and moves it towards the center of the cylinder. This observation is discussed further in Chapter 4.

Our interpretation of the different zones within the cylinder during combustion is illustrated in Fig 3.6. Three distinct zones are identified: an unburned fuel-air mixture zone ahead of the flame front; a flame zone (which appears in the photographs as a superposition of a large number of thin irregular dark lines); and a fully burned zone behind the flame zone. We will discuss the structure of the flame zone in more detail in Chapter 4. It has a thickness of 10 to 15 mm. We will show that it contains unburned, burning,

and fully burned mixture. Note that burning continues for a long time after the front of the flame has reached the cylinder wall opposite the spark plug. The schematic in Fig 3.6 helps the interpretation of the photographs of the flame. The burned zone cannot be visualized until the back of the flame zone reaches the glass windows. The last few photographs in Fig 3.5 show the irregular shape of this flame "back", and the final burn-up of mixture in the corners of the chamber.

A detail study of the combustion process is presented in Chapter 4.

3.4 Expansion Process

During the expansion process the falling pressure in the combustion chamber causes any trapped gas in the crevices in the combustion chamber walls to expand out into the cylinder. For example, one or more dark streaks are observed in the Schlieren movies emanating from the spark plug as the cylinder pressure falls (see upper right hand corner of pictures in Fig 3.7). This streak is presumed to be an unburned and burned mixture pushed into this crevice prior to time of peak pressure, cooled by heat transfer to the plug surfaces to a higher density than the bulk cylinder

burned gas, and expanded out of the crevice after peak pressure.

Another flow observed expanding into the cylinder is the flow from the crevices at the piston-crown corners. At about 120 degrees after TC (see Fig 3.7c) two jet-like expansion flows can be seen emanating from this crevice (engine operating at half throttle and at 1380 rpm). The jets spread axially and transversely into the cylinder (Fig 3.7d). The front of the jet first accelerates, then loses speed, and then accelerates again with the opening of the exhaust valve (the velocity normal to the jet front is shown in Fig 3.8). The gas in the jet reaches the exhaust valve when the piston is near BC.

To interpret this flow, it is necessary to examine the design of the piston and rings in this engine. Figure 3.9 shows the piston ring assembly with arrows indicating the passages through which the charge can flow to the region behind and between the rings. These passages are at the corners where the ring sections overlap. The flow area of these orifice type passages at each corner is almost the same as the ring gap area of a conventional engine (see Table 2.2).

In Chapter 5 we will present a model to describe this flow. Using this model we conclude that as the presure in the cylinder increases during compression and combustion, first unburned and then burned mixture is pushed into the region behind and between the rings [28,31]. The flow of the charge into these regions continues in the expansion stroke until the increasing pressure within this crevice region becomes equal to the decreasing pressure in the cylinder. At this point (120 degrees ATC for this engine operating at discussed conditions) the flow reverses direction, and the trapped gas flows out of the volume behind and between the rings into the cylinder.

The same model predicts that during the expansion stroke, while part of the gas in the top land crevice is pushed into the regions behind and between the rings, other parts of the gas in this crevice should expand out into the combustion chamber. Therefore, a flow back into the cylinder as early as 30-50 degrees ATC is expected. But this flow is not observed. We believe that this gas expanding out of the top land crevice occurs at low velocity and remains against the wall; it is obscured from observation by the dark thermal boundary layer.

The flow out of the top land crevice prior to the observed jet flow from the region behind the top ring is expected to be a laminar flow. The Reynolds number of this flow is of order 100, based on piston speed, and of order 10, based on the velocity of the expanding gas relative to the piston. The nature of this expanding gas is expected to be similar to the observed slowly moving, expanding gas out of the top land crevice during the intake stroke at part load (Fig 3.1). But during the intake stroke, the dark thermal boundary layer on the combustion chamber wall is 0.5 mm thick [32,33] while the piston cylinder clearance is of order of 1 mm. Therefore, we are able to recognize this flow during intake. However, during the expansion stroke, the thermal boundary layer is about 2 mm, which fully obscures the piston cylinder clearance. Note that even during the intake stroke it is hard to recognize the flow out of the left crevice, which has a clearance of 0.4 mm.

During the expansion stroke the gas expanding out of the crevice which is expected to stay on the wall and the gas that jets from the region behind the ring, is partially unburned. These flows contribute to the hydrocarbon emission and inefficiency of the engine. Similar flows are expected in a real engine. This will be discussed in Chapter 5 and 6.

3.5 Exhaust Process

The exhaust process starts when the exhaust valve opens at 140 degrees after TC during the expansion stroke. There is a delay of about 10 degrees before the burnt gases are observed to move in the direction of the valve. Then, it takes an additional 10 degrees for gas close to the valve to accelerate to a maximum velocity of about 12 m/s. Such vigorous gas motion persists through blowdown until the cylinder pressure approaches the exhaust presure. The rapidity with which the blowdown flow is established is visualized by the entrainment of the denser (dark) thermal boundary layers on the cylinder head and upper part of the cylinder wall by the outgoing gases which "sweep" these surfaces clean. (This entrainment continues after blowdown through the entire exhaust process). In addition, long vertical dark streaks that were observed expanding downwards from the spark-plug crevice earlier during the expansion stroke are also displaced rapidly towards the exhaust valve. These denser regions are likely to contain unburned hydrocarbons and contribute to the peak in hydrocarbon emissions measured in the exhaust gases during the blowdown process in time-resolved exhaust sampling experiments [21,22,34].

The jets observed emanating from crevices between the cylinder wall and the piston and behind the piston rings during the expansion process, which are just visible before the exhaust valve opens, move through the cylinder during the blowdown process. The jets accelerate to a maximum velocity of 18 m/s at about 15 degrees before BC and reach the exhaust valve a few degrees after BC. Some of the gas in the jets leaves the cylinder directly, while part of it stays circulating under the valve, as shown in Fig 3.10, until pushed out by the approaching piston. This gas is also expected to have a high unburned hydrocarbon concentration.

During the exhaust stroke, vortices in the corner of the piston crown and cylinder wall were observed, which grow in size as the exhaust stroke proceeds. The existence of this vortex flow within an engine cylinder was first observed by Tabaczynski et al. [35] in water analog experiments, who concluded that the vortex is generated by the scraping off and rolling-up of the boundary layer on the cylinder wall by the piston crown. Such a vortex has been visualized in a square cross-section rapid compression machine where the gas was initially at rest. Schlieren movies of that rapid compression machine flow showed the vortex to be stable and grow uniformly [8,9].

In our engine the vortex was observable both when viewed in cross-section along the vortex axis in the steel-sidewall piston-crown corners and when viewed perpendicular to the vortex axis in the glass-sidewall piston corners. Figure 3.11 shows a Schlieren photograph and an explanatory sketch of the vortex. However, the vortex was not always stable and sometimes broke up soon after it had formed (e.g.: the left hand side vortex of Fig 3.12). The instability could result from the residual turbulent flow in the cylinder, from the square cross-section geometry, or from the different size crevice on the right and left sides of the piston (see Table 2.2).

We expect the layer which is scraped off the wall and rolled up into this vortex to contain the unburned fuel which is held against the cylinder wall. As discussed in Section 3.3, this unburned fuel is expected to be from the top land crevice gas.

As the piston approached TC, the vortex was observed to distort and break up; its top sections lift off and move towards the still-open exhaust valve. Whether part of the vortex exits the cylinder at the end of the exhaust process in this engine with its higher than normal clearance height could not be discerned from the movies.

Time-resolved exhaust sampling experiments [21-23,34] in conventional engines indicate a peak in the hydrocarbon level at the end of the exhaust stroke. This peak is expected to be the contribution of the unburned fuel in these vortices [21].

CHAPTER 4

DETAILED STUDY OF THE COMBUSTION PROCESS

In Section 3.3 we presented a set of photographs (Fig 3.5) of the entire combustion process for one typical operating cycle. We discussed how a flame kernel initiated by the spark plug develops into a turbulent flame with a thickness of 10 to 15 mm. We also mentioned how cylinder gas motion affects flame propagation. In Section 4.1 we will discuss the flame velocity and show that the thick flame is expected to contain unburned, burning, and fully burned mixture. In Section 4.2 we will discuss ignition, and in Section 4.3 we will elaborate on the effect of gas motion on the cycle-by-cycle variation.

4.1 Flame Velocity and Flame Structure

The apparent flame velocity was measured from successive frames of two individual cycles from one of the movies, and the results are shown in Fig 4.1. This velocity was determined from the average observed flame travel between frames, normal to the flame front. This velocity rises to a maximum of about 55 degrees after the spark (i.e. at TDC) and then decreases. Determining the actual flame front speed relative to the unburned mixture ahead of the flame (variously called the turbulent flame speed, entrainment speed [36] etc.) required that the rate of compression of the unburned gas ahead of the flame be estimated so that the unburned gas velocity at the flame front could be calculated. Using a spherical flame front assumption, centered at the spark plug, this was done for a few cycles at the time the flame was about halfway across the combustion chamber, and the actual flame speed was found to be about 8 m/s.

Figure 4.2 displays the measured pressure trace and the calculated mass fraction burned profile of the cycle shown in Fig 3.5. Five stages of flame development of Fig 3.5 are indicated on the pressure trace. This figure reveals that the rate of enflamation of the charge is faster than the rate of burning. The position of the flame as seen from the

movies is misleading because we are viewing across an approximately spherical flame front. Therefore the estimated volume percentage of charge enflamed V_f is shown in Fig 4.3 with the mass fraction burned profile of the previous figure. The calculated mass fraction in the enflamed region X_f is also displayed; X_f is computed from the density of the unburned charge (calculated in the thermodynamic model) and the non-enflamed volume. The enflamed volume is determined from the position of the flame in the movies, with the assumption of a spherical flame front. Comparison of X_b, the mass fraction burned and X_f, the mass fraction enflamed, indicates that only a fraction (between 50 and 70 percent) of the enflamed mass is burnt. This observation is consistent with the engine turbulent flame models of Blizard, Keck [36] and Tabaczynski, et al. [37,38], where within the enflamed charge, fuel-air mixture burns in a laminar combustion process though the entrainment of the unburned gas into the flame is turbulent [39].

A characteristic burning time can be obtained from the data in Fig 4.3. It is defined by

$$\tau \frac{dm_b}{dt} = m_e - m_b$$

where m_e is the mass entrained and m_e the mass burned at any crank angle [36]. It is a function of crank angle and has an average value of about 1.8 ms for this engine at the operating conditions considered. This time gives a characteristic turbulent flame thickness of 1.8 (ms)x8 (m/s)=14 mm, which is comparable to the observed thickness of the flame, front to back. A characteristic laminar length scale can also be obtained $\ell_L = S_L \tau$, where S_L is the laminar flame speed. For a propane-air mixture at appropriate unburned mixture conditions, S_L=70 cm/s [40] and ℓ_L=1.3 mm.

Observations of the flame structure can best be made at the leading edge of the flame front where the superposition of reaction zones along the line of sight is at a minimum. It has been shown by Weinburg [41] that the darkest regions in Schlieren flame photographs correspond to the point in the flame where the temperature is 1.5 times the unburned mixture temperature. At the mid-point in the burning process, the unburned mixture temperature is about 900 K and the burned mixture temperature is about 2600 K; the dark lines would correspond to about 1350 K.

Figure 4.4 shows an enlargement of a region of the flame front. The photograph was taken with reduced Schlieren system sensitivity to eliminate effects other than those caused by the thin flame reaction regions. The dark boundary at the flame front represents the start of the actual burning zone; the outer flow region is unburned and the inner region is burned gas. The typical size of these individual structures (a burned gas zone surrounded at least in part by a thin reaction zone) is 2.5 mm. Assuming equal expansion in all directions, this corresponds to an unburned gas region of size 1.5 mm, which is close to the characterisitic length scale obtained from the burning time and laminar flame speed.

Figure 4.5 shows the back side of the flame zone enlarged to the same magnification as Fig 4.4. Here it is unburned regions that are "enclosed" by thin reaction zones. Due to the higher cylinder pressure at this point, and because the "enclosed" gas is now unburned, the scale appears considerably smaller.

4.2 Ignition

To examine the ignition process and flame kernel growth, spark photographs of different cycles were taken at selected times after the spark discharge. The delay unit on the strobe flash was used to control the delay to intervals of 0.01 msec (about 0.08 deg) after the time the spark was triggered. These pictures are shown on Figure 4.6. The first picture is for reference, taken with the engine static. A small vertical line just to the left of the spark plug is either a deposit on the windows or a flaw in the glass. The spark plug is the same one used for the movies, but it is now oriented so that the full length of the bottom electrode can be seen.

Pictures 4.6b and c were both taken at the time of the spark. They show clearly the spark discharge between the electrodes. In 4.6b the discharge is at the edge, but in 4.6c it is at the center of the electrodes. In this engine the spark discharge duration varies between 1.5 to 5 degrees from cycle to cycle, as measured by the voltage of the igition system.

Picture 4.6d was taken 0.5 degrees (0.06 ms) after the spark of a firing cycle and shows the appearance of the spark and a kernel (high temperature zone around the

discharge) which has filled up less than 1/2 of the electrode spacing. Pictures 4.6d through 4.6i show the slow growth of the kernel. At 2 degrees after the discharge the spark cannot be seen anymore (Fig 4.6i) and the kernel has filled up all the electrode gap space. Picture 4.6j (2.5 degrees after the spark) shows a flame structure similar in appearance to the fully developed flame. Pictures 4.6k to 4.6s show how this flame grows and enflames the region around the spark plug.

Figure 4.6t shows a still picture taken 1.5 degrees (0.18 msce) after the spark in a motoring cycle without fuel. The spark is still apparent with a kernel (hot region around spark) as a white zone around it.

4.3 Cycle-by-Cycle Variation

The origin of cycle-by-cycle combustion variations is believed to be close to the ignition site. For example, the photographic studies of Nakanishi, et. al. [4] have shown that dispersion in the volume enflamed is present from the start of combustion. These factors have been found to influence cyclic dispersion:

(i) The variation in gas motion at the spark plug location at time of ignition.

(ii) The variation in air-fuel ratio supplied to a given cylinder for each cycle (due to variations in fuel distribution and vaporization in the manifold).

(iii) Nonuniform mixture composition in the cylinder due to incomplete mixing between air, fuel, and burned gases (recycled exhaust and residual).

(iv) Variation in the amount of residual gas in the cylinder, cycle-by-cycle.

In the current experiments with a uniform premixed propane-air unburned mixture, only (i), incomplete mixing with residual in (iii), and (iv) can contribute.

The process of flame initiation as discussed in the previous section consists of the spark discharge, creation of a kernel around the spark, and the subsequent emergence of a turbulent flame front from the kernel. The cycle-by-cycle variation as seen by variations in the timing of flame emergence in flame growth rates and in flame shape was observed to depend strongly on these initial stages of combustion. While we could not observe whether nonhomogeneity of the fuel-air and residual gas mixture

around the spark plug was a significant factor, we were able to observe the effects of variations in the mixture motion close to the electrodes. We will now review sets of still photographs taken at selected times after spark discharge (each photograph is from a different cycle).

Figures 4.7a and b, both taken at 9.5 degrees after spark, show that substantial differences in kernel development exist between cycles. The kernel in 4.7b seems to be moving to the center of the chamber. The numbers beneath each picture are the peak cylinder pressure in atmosphers for each cycle. Figures 4.8a and b, taken at 12 degrees after spark, illustrate the effect of variations in mixture motion moving the developing flame to the left or the right at about the same degree of development. Figure 4.9 shows three photographs at 14 degrees after spark. Figure 4.10 shows nine photographs at 31 degrees after spark. Substantial differences in flame front size and shape and location and motion of flame center are evident (e.g.: Fig 4.10h shows the flame blown off the spark plug). Figures 4.10a and h show the flame center moving towards the center of the combustion chamber. As a result the flame front area is increased and fresh mixture can be entrained across the front faster. Faster combustion combined with a shorter flame travel path gives a rapid rate of pressure

rise for these cycles and a higher peak pressure. The average peak pressure of blown-off cycles is about 11.5 atm (the lower pressure of 4.10h [10.5 atm] is due to the delay in flame initiation of this cycle). Figure 4.10i also shows a detached flame from the spark plug, but the enflamed region is very small. A cycle such as 4.10i was rare in this engine. Also observed, although not shown in the pictures, was the situation when two flame fronts developed from the spark plug.

The flame-center motion towards the cylinder center is believed due to the corner vortices generated during the intake process which produce velocities of order 6 ms around the spark at the ignition time. We noted that the blow-off of the flame was significantly influenced by spark plug orientation. The fraction of cycles where the flame was blown-off the plug towards the cylinder center was much higher with the plug orientation of Fig 4.4 (the bottom electrode support is between the cylinder axis and the spark plug axis; the bottom electrode makes an angle of about 45 degrees to the plane joining these two axes), than for the orientation of Fig 4.6 to 4.10 (the bottom electrode support is on the opposite side of the plug axis to the cylinder axis and the bottom electode is parallel to the plane joining these two axes). In the latter position the kernel

is protected by the electrode support from the gas motion toward the cylinder center set up during intake.

Figure 4.11, with three sets of pictures at 46 degrees, 60 degrees and 65 degrees after spark respectively, indicates the effect of cyclic dispersion when the flame is fully developed. Both flame front location and flame shape show substantial variations.

To expand our analysis of cycle-by-cycle variations, a plot was made of flame front position at fixed crank angle intervals for three consecutive cycles. These drawings are shown in Fig 4.12 with the corresponding pressure traces in Fig 4.13. Each number indicates crank angle degree referred to TC. The bottom horizontal line is the piston top, and its irregularity is due to the thermal boundary layer that covers it. Although the three cycles show variations in maximum pressure and crank angle at which the peak pressure occurs, it is difficult to observe variations at the start of combustion from the pressure trace. But observation of the flame diagrams (Figs 4.12a, b, c) show two distinctive flame growth patterns. In Figs 4.12a and 4.12c the flame spreads first along the top of the combustion chamber, and then progresses outward from the flame center, resulting in a larger flame surface area than in Fig 4.12b. In the last case the flame advances outwards from the spark plug, and,

once the flame reaches the piston crown, propagates from right to left with its height and hence flame surface area, controlled by the space between piston and cylinder head. By selecting a fixed crank angle (e.g.: -7.6 degrees) and observing the position of the flame front, it is seen that Fig 4.12a has the largest flame area, while 4.12b has the smallest. This is in agreement with the fact that 4.12a has a higher and earlier occuring peak pressure than 4.12b. The slower burning of 4.12b is also verified by the last traces of the front. At +7.6 degrees 4.12b still shows an unburned zone ahead of the flame, while in 4.12a and 4.12c the flame fronts have already reached the cylinder wall opposite the spark plug.

To examine the effect of slow initial flame growth on the propagation of the fully developed flame, a normal cycle and slow-burning cycle were analyzed in more detail. Figures 4.14a and b show the flame location of two successive cycles; Fig 4.14a is a normal cycle with peak pressure 10.7 atm at 15 degrees ATC, Fig 4.14b is a slow burning cycle with 4.85 atm peak pressure at 47 degrees ATC. Figure 4.15 shows the average flame radius versus time for these two cycles and reveals two important points. The first is that for both cycles the flame becomes fully developed (reaches a constant apparent flame speed) when the

flame has traveled a distance of about 2 cm. This is consistent with the idea that the fully turbulent flame starts when a few eddies the size of the chamber height are burned [37]. (In this engine the clearance volume height is 3 cm.) The second point from Fig 4.15 is that differences in the initial stages of combustion, before the flame is fully developed, lead to substantial variations in flame front location. Note that the actual flame velocity in the fully developed region of the two cycles is affected by the unburned gas velocity. A better measure of the difference between fully developed flame regions of these two cycles is to compare the turbulent or entrainment velocity which is 8.4 m/s for normal cycle and 8.0 m/s for late cycle, both calculated at TDC.

THIS PAGE WAS INTENTIONALLY LEFT BLANK

CHAPTER 5

CREVICE GAS MOTION STUDIES IN THE FLOW VISUALIZATION ENGINE

In Section 3.4 we discussed that, during the expansion process of the flow-visualization engine, two jet-like flows are observed emanating from the top land crevice (Fig 3.7). This flow is believed to be from the regions behind and between the rings. As the pressure in the cylinder increases during compression and during combustion, burned and unburned mixture is pushed into these regions. The flow into these regions continues into the expansion stroke until the increasing pressures within these crevice regions becomes equal to the decreasing pressure of the combustion chamber. At this point the flow reverses direction and the trapped gas jets into the cylinder. For the case that was presented in Section 3.4, this jet was observed at 120 degrees ATC.

The timing of the jet-like reverse flow is predicted by a model which will be described in the following section. For all cases studied which are presented in this chapter,

the model predicts that this reverse flow is observed when the pressure of the region behind the top ring exceeds the cylinder pressure.

The timing of the reverse flow is controlled by the engine operating conditions, the volume of the regions behind and between the rings, and by the passage area connecting these regions. By increasing the passage area into the region behind the top ring, we were able to change the timing of this reverse flow to 45 degrees ATC.

In addition, there is a second flow phenomenon which occurs. During expansion the falling pressure of the cylinder causes the gas trapped in the top land crevice to expand into the combustion chamber. The model predicts that some of the gas trapped in the top land crevice should expand out prior to the reverse jet-like flow from the region behind the ring. However, this expanding flow is not observed in this engine. To further investigate this expanding flow, we performed an experiment which simulates the piston and ring geometry of a real engine. This experiment is discussed in Section 5.2. Finally in Section 5.3, we present the experiment which convinced us that the heat transfer from the gas in the regions behind and between the rings was sufficiently rapid so that the flows could be assumed isothermal.

5.1 Modeling the Flow in the Crevice Regions of the Flow-Visualization Engine

As discussed in Section 3.4, in the flow-visualization engine the regions behind and between the rings are connected by the orifice-like passages where the ring segments overlap (Fig 3.9). The model geometry of the crevice regions in this engine is presented in Fig 5.1. Piston top land crevice is defined as region 1, the volume behind the top ring as region 2, and so on. Plane (a) is located at the entrance to the top land crevice. Plane (b) separates region 1 from region 2.

The flow in the top land crevice is a fully developed laminar flow. The drop in the dynamic pressure along this crevice is negligible; thus the dynamic pressure at plane (b) is assumed to be the same as the combustion chamber pressure. It is also assumed that each other region has a uniform pressure.

The continuity equation for each region is:

$$\frac{dm_i}{dt} = \dot{m}_{i-1,i} - \dot{m}_{i,i+1} \qquad i = 1 \text{ to } 6 \qquad (\text{eq } 5.1)$$

The flow between regions was modeled as orifice flow:

$$\dot{m}_{i,i+1} = fC_d A_i \rho_i C_i \eta_i \qquad i = 1 \text{ to } 6 \qquad (\text{eq } 5.2)$$

f = friction coefficient

C_d = discharge coefficient

for all cases fC_d =0.6 was used

A_i = area of the orifice connecting the regions

ρ_i = density of the ith region

C_i = sound speed in the ith region

η_i = compressibility effect

$$= \frac{2}{\gamma-1} \left[(\frac{P_{i+1}}{P_i})^{2/\gamma} - (\frac{P_{i+1}}{P_i})^{(\gamma+1)/\gamma} \right]^{\frac{1}{2}}$$

$$= (\frac{2}{\gamma+1})^{\frac{\gamma+1}{2(\gamma-1)}} \qquad \text{when } \frac{P_{i+1}}{P_i} \leq 0.52$$

For heat transfer from the gas to the walls of the regions, two extremes of adiabatic and isothermal flow were considered. For the adiabatic case, the continuity equation becomes:

$$m_{o_i} \frac{d(P_i/P_{o_i})^{1/\gamma}}{dt} = \dot{m}_{i-1,i} - \dot{m}_{i,i+1} \qquad \text{(eq 5.3)}$$

and for the isothermal case $(P/\rho = \text{const})$ the continuity equation becomes:

$$m_{o_i} \frac{d(P_i/P_{o_i})}{dt} = \dot{m}_{i-1,i} - \dot{m}_{i,i+1} \qquad \text{(eq 5.4)}$$

where

P_i = pressure of region i

P_{o_i} = initial pressure of region i

m_{o_i} = initial mass in region i

Solving either equations 5.3 or 5.4 coupled with mass flow rate equation 5.2, the pressure of all the regions behind and between the rings (regions 2, 3, 4, 5 and 6 in Fig 5.1) and the mass flow rate between adjacent regions can be calculated. A result of special interest is the mass flow rate crossing the entrance of the top land crevice (plane (a) in Fig 5.1) because it should predict the timing of the flow from this crevice region. In Fig 5.2 this mass flow rate is plotted versus crank angle for the engine operating at 1380 rpm and at half throttle. This is the same condition as for pictures in Fig 3.7 which showed that the jet out of piston crevice corner to occur at 120 degrees ATC.

Figure 5.3 shows the measured pressure of the main chamber (highest curve) and the calculated pressure of the region behind the top ring for adiabatic flow (middle curve) and isothermal flow (lowest curve) for the same condition. The point at which the pressure of the region behind the top

ring, region 2, equals the pressure of the combustion chamber corresponds to the time at which the flow across the plane (b), initially from region 1 to region 2, reverses direction (plane (b)).

Table 5.1 summarizes the predicted timing of the flow through plane (a) and (b) toward the combustion chamber for the isothermal and adiabatic cases. Flow out of plane (a) top land crevice entrance is predicted to occur at about 40 degrees ATC. The timing at which jets in the corners of the piston crown were observed is 120 degrees ATC, which is far from this prediction. However, this observed timing is close to the predicted time when the flow across plane (b) reverses direction, which is about 110 degrees ATC. This phenomenon was examined at other engine operating conditions. The operating conditions considered were a speed of 1380 rpm with inlet pressures of 0.5 and 0.7 atm, and also a speed of 810 rpm with an inlet pressure of 0.7 atm. Figure 5.4 shows the comparison between the observed timing of the jet-like flow out of top land crevice and predicted timing of the flow out of plane (b). This figure presents only the result for the isothermal flow because, by other experiments, we concluded that the flow is best approximated by the isothermal model (we present this experiment later). The different timing of the flow for a

given engine operating condition is caused by cycle-by-cycle variation. The predicted timing of the flow reversal at plane (a) for the presented cases (Fig 5.4) was always earlier than 50 ATC. The observed timing of the jet-like flow out of plane (a) ranged from 100 degrees to 140 degrees ATC. Each observed timing of the flow out of plane (a) agreed well with the predicted timing of the flow reversal at plane (b).

The timing of the flow out of the top land crevice for a given engine operating conditon is controlled by the volume of the regions behind and between the rings and by the passage area connecting these regions. In order to change this timing substantially for a given engine operating condition, we performed an experiment in which the passage area into the region behind the top ring was increased by a factor of four. To do so, as shown in Fig 5.5, an additional channel of 0.25 mm by 25 mm was created on one of the four segments of the top ring.

The pictures in Fig 5.6a show the result of this experiment for the engine operating conditions of 1380 rpm and 0.7 atm inlet pressure. Figure 5.6b shows the schematic of the flow from the top land crevice. Other phenomena on the pictures of Fig 5.6a, which are not shown on the schematic of Fig 5.6b, are due to effects which will be

discussed later(section 5.2). These effects do not change the nature of the crevice flow. The flow from the left side, the side with the ring having the additional channel, appeared at about 42 degrees ATC, and the flow from the right side appeared at about 45 degrees ATC. The model predicted the flow out of plane (a) to occur around 25 degrees ATC and that out of plane (b) to occur around 40 degrees.

From this evidence we conclude that the observed timing of the jet-type flow out of the top land crevice does not correspond to the predicted timing of this flow. However, the flow appears to jet out of the top land crevice corner when the pressure behind the top ring exceeds the combustion chamber pressure. The question arises as to why the expanding gas out of the top land crevice is not observed prior to the appearance of the jet out of the region behind the top ring. We believe that this expanding gas may remain close to the wall because it leaves the crevice at low velocity, obscured from observation by the dark thick thermal boundary layer. The thermal boundary layer thickness in this engine during the expansion stroke is of order of 2 mm [32,33], while the piston cylinder clearance is of order of 1 mm. The flow out of the top land crevice prior to the jet flow from the region behind the top ring is

a laminar flow with Reynolds number of order 100, based on piston speed and Reynolds numer of order 10, based on the relative expanding gas velocity with regard to the piston.

Througout the intake process a similar flow (Rey=250 based on piston speed) was observed expanding out of the top land crevice (right side crevice of Fig 3.1). In contrast to the expansion stroke the dark thermal boundary layer on the combustion chamber wall is thin(0.5 mm thick), and therefore, part of the top land crevice exit is visible(see schematic in Fig 5.7). Note that even during the intake stroke it is hard to recognize the flow out of the left crevice which has a clearance of 0.4 mm.

In the next section we discuss experiments which further explore the viscous expanding flow out of the top land crevice simulated for a real engine.

5.2 Crevice Flow from a Simulated Real Engine Crevice Region

The objective of this experiment was to examine a geometry having crevice volumes and passage areas connecting the crevice regions similar to that of a real engine. Furthermore, we wanted to remove the top land crevice exit from the vicinity of the obscuring thermal boundary layer so we could investigate the expanding flow out of this region.

We chose a piston from a small displacement engine having a bore less than the bore of the square piston engine (see Table 5.2 for geometry of this piston). As shown in Fig 5.8, the ring belt of this piston was cut just above the oil ring. This ring belt with both compression rings in place was press fit into a square piston holder having an inner circular bore corresponding to the conventional cylinder size. This assembly was then secured to the top of the square piston. The compression ratio of the square piston-cylinder engine was raised to 5.2.

This assembly had five regions as shown on Fig 5.9. Only region 1, the top land crevice, was connected to the combustion chamber. Since the ring is split, any two adjacent regions were connected through the ring gap. Depending on the position of the ring in the groove, these regions might also be connected by the ring side clearance.

The second ring was fixed against the lower surface of the groove. In two different experiments, the top ring was held first against the lower surface of the groove and then against the upper surface of the groove.

A model to describe the flow in these crevice regions was developed. This flow model is similar to the one which is developed for a real engine and is presented in next Chapter. It was found that the pressure in region 1, the top land crevice, is uniform and equal to the pressure of the combustion chamber. Furthermore, it was found that two adjacent regions connected by the ring side clearance had essentially equal pressures (i.e., $P_1 = P_2$, $P_3 = P_4$ in Fig 5.9a, and $P_2 = P_3 = P_4$ in Fig 5.9b).

Figure 5.10a shows two Schlieren pictures of the experiment with the top ring of the conventional piston held against the lower surface of its groove (corresponding to Fig 5.9a). Fig 5.10b shows the schematic of the flow from the newly added crevice regions. In the center of the picture a jet is observed which is the flow through the top ring gap of the inner, circular piston. We made sure that this jet was indeed from the top ring end gap by rotating the ring to change the position of this gap. Thus, we were able to visualize this jet at different positions corresponding to the top ring gap orientation. This jet

continued to flow until about 40-50 degrees after the exhaust valve opened. A comparison between the observed timing of this flow, and the model's prediction is shown in Fig 5.11.

The other flow marked as "expanding flow" on the schematic was presumed to be from the top land crevice of the inner piston. This flow is the expansion of fluid, trapped in the inner-piston top-land crevice, into the combustion chamber. This crevice flow was visualized at about 30-50 degrees ATC and could not be followed after 120 degrees ATC when the piston disappeared from the camera's field of view. An uncertainty of 10 crank angle degrees is involved in recognizing the start of this flow. This was due to the sluggish nature of this flow and its interference with the thermal boundary layer on the piston top. This flow had a Reynolds number of 10 and had a maximum velocity of 1 m/sec as measured from the high speed movies. This measured velocity agreed well with the calculated velocity for the expanding gas out of the inner piston top land crevice.

Figure 5.12 shows Schlieren pictures and a schematic for the flow which occurred when the top ring of the inner piston was held against the upper surface of its groove. The flows shown in these pictures (also observed in

high-speed movies) appeared similar to the flows for the case when the ring was held against the inner surface of the groove. However, there is a timing difference for the jets in each case. When the ring was held against the upper surface of its groove, on average the jet appeared 10 degrees later than when the ring was held against the lower surface of the groove. Furthermore, holding the ring against the upper surface caused the flow out of the top land crevice of the inner piston to be slower than when the ring was staked to its lower surface. Both of these observations were in agreement with the model's predictions. (Incidentally, the pictures which were presented on Fig 5.6 of previous sections were taken at similar test conditions, with the inner piston top ring staked to the upper surface of its groove.)

From these observations we conclude that with the geometry of a real piston assembly, jet flow similar to the one in the square piston engine occurs. The jet type flow is from ring gap. Furthermore, we observed an additional flow expanding out of the topland crevice for the inner piston. This flow, unlike the jet flow through the gap, is a laminar flow. It is likely that this viscous, expanding gas remains against the cylinder wall in a real engine. This layer is expected to be scraped off the wall by the

upward moving piston during the exhaust stroke.

5.3 Crevice Gas Heat Transfer Assumptions

In the previous sections we showed that the predicted flow timing out of the crevice regions in a square piston engine for the isothermal flow differs by a few crank angle degrees from the adiabatic case (refer to Fig 5.3). However, the amount of the mass trapped in the regions behind and between the rings for these two cases differs by as much as 30% . We would like to extend the previously discussed crevice flow model to a real engine and calculate the amount of the mass trapped in the crevice regions. The following experiments verify that the flow behind and between the rings can be satisfactorily approximated as isothermal flow.

In order to alleviate complications associated with analyzing experimentally the flow through a moving piston crevice volume, we designed an independent experiment to check the model's heat transfer assumptions. A brass plug of fixed internal volume was inserted into one of the available pressure transducer ports. Figure 5.13 illustrates this plug. A standard pressure transducer was then mounted inside the plug. A passage of fixed volume connects the pressure transducer sensor to the combustion

chamber. A plate with a known orifice diameter is secured to the cylinder side of the brass plug. A series of different orifice sizes was used to vary the residence time of the flow inside the plug for a fixed passage volume. In addition, the interval passage volume of the plug was varied for a fixed orifice size. This was accomplished by repositioning the pressure transducer.

Similar to the previously discussed model, the continuity equation for this single volume orifice system is:

$$V_p \frac{d\rho_p}{dt} = C_d A \rho C \eta \qquad \text{(eq 5.5)}$$

V_p = plug volume

ρ_p = density of the gas inside the plug

C_d = discharge coefficient

A = area of the orifice

ρ = density downstream

C = sound speed downstream

η = compressibility effect

Let us define the residence time of the flow by:

$$\tau = \frac{1}{C_d \eta C} \left(\frac{V_p}{A}\right) \qquad \text{(eq 5.6)}$$

For the isothermal flow (P/ρ = const) the equation
5.5 reforms to:

$$m_o \frac{d(P/P_o)}{dt} = C_d A \rho C \eta \qquad \text{(eq 5.7)}$$

and for the adiabatic flow it becomes:

$$m_o \frac{d(P/P_o)^{1/\gamma}}{dt} = C_d A \rho C \eta \qquad \text{(eq 5.8)}$$

P = pressure in the plug

P_o = reference pressure of the plug

m_o = reference mass in the plug corresponding to P_o

The pressure inside the plug was calculated for both
the isothermal and adiabatic cases . The calculated
pressure was then compared to the measured pressure.

The orifice area and the volume of the plug were chosen
so that the residence time of the flow (eq 5.6) was similar
to that for a real engine. The ratio of the volume behind
and between the rings to the area of the ring gap in the
square piston engine as well as in a real engine, is of
order of 100 cm. In our experiment with the plug we covered
a volume to area ratio ranging from 80 to 1000 cm.

Figure 5.14 shows a measured pressure trace inside the plug for a volume to area ratio of 100. On the same figure, the calculated pressure inside the plug for the isothermal and adiabatic cases are shown.

It is clear that the isothermal assumption results in a calculated pressured close to the measured one for this volume to area ratio. This was typical of all 12 volume area ratios within the range studied. Figure 5.15 shows the measured pressure and the isothermally based calculated pressure for a volume to area ratio of 220, representative of a real engine geometry.

THIS PAGE WAS INTENTIONALLY LEFT BLANK

CHAPTER 6

REAL ENGINE MODEL

In the previous sections we demonstrated that in the square piston-cylinder engine the burned and unburned gas which is pushed into the regions behind and between the rings flows back into the cylinders about half-way through the expansion stroke. The timing of this flow was predicted using a system model of orifices and volumes for an isothermal flow. In the following sections we will attempt to extend this model to a real engine.

In the square piston-cylinder engine the area of the passages conncting the crevice regions was constant over the portion of the cycle of interest (until the flow returned back to the cylinder). However, for the real engine this area varies during the entire cycle due to the ring motion in the groove. Therefore, the flow model must be coupled with a model for ring motion.

This model will be presented in the next section. It will then be validated by comparing verified experimental data on blowby with predictions. In the last section the model will be used to study the variation of the mass flow of unburned fuel from crevice regions with geometry, piston speed, load, and wall temperature. Experimental data will be used to verify the trends predicted by the model.

6.1 Crevice Gas Flow in a Real Engine

6.1.1 Gas passages

Figure 6.1 shows a schematic of a piston with two compression rings, which is representative of the spark-ignition engines of today. Numbers 1 through 5 identify regions we will refer to later. Region 5 is located just above the oil ring and is assumed to be at crankcase pressure. The arrows between regions show possible flow passages.

Since the ring is split, any two neighboring regions are always connected by the ring end gap. Depending on the position of the ring in the groove, they may also be connected by ring side clearance. For example, consider region 1 (top land crevice) and region 2 (behind top ring) on the compression stroke. It will be shown later that on

the compression stroke the top ring sits on the lower surface of the groove, and therefore, there is a flow over the ring from 1 to 2. At the same time, regions 2 and 3 are connected only through the ring gap. But as the direction of the force acting on the ring changes, the ring lifts from the lower surface of the groove, and regions 2 and 3 as well as regions 1 and 2 are connected by side clearance until the ring approaches the other side of the groove and blocks that passage. The transition of the ring to the other side is not instantaneous and takes 20-60 crank angle degrees, as will be demonstrated later. It is therefore necessary to model the ring motion in order to determine the side clearance passage area as a function of crank angle.

6.1.2 Ring motion model

There is considerable evidence of ring motion in the groove [42,43]. The ring can tilt or move axially up and down in the groove. Experimental evidences of Furuhama [44] and theoretical works of Rungert [45] show that the ring tilt angular displacement is of order 5 minutes--not enough to have a marked effect on the flow passsage area. The ring must tilt of order 1 degree (60 minutes) to fully block both ring side clearances (see Fig 6.2). Therefore, we will consider only the axial motion of the ring in the groove and

assume that groove surfaces are flat.

The forces that act on the ring in axial direction are shown in Fig 6.3. They are as follows:

-pressure forces F_p

-friction forces F_f

-inertia forces F_i

-resistance of the squeezed oil F

The detailed calculation and assumptions involved are summarized in Appendix (6.1). Below are the final equations for the forces acting on the top ring.

The pressure force:

$$F_{P_1} = A_{r_1} \frac{P_1 - P_3}{2}$$

where A_{r_1}: first rings area in radial direction

$\quad\quad$ P_1: pressure above the top ring

$\quad\quad$ P_3: pressure below the top ring

Friction force:

$$F_{f_1} = P_2(\pi d_{r_1} T_{r_1}) \ f_1$$

$$f_1 = 4.8(\frac{\mu_{oil} U_p}{P_2})^{\frac{1}{2}}$$

P_2: pressure behind the top ring

d_{r_1}: diameter of the top ring in radial direction

T_{r_1}: thickness of the top ring

f_1: friction coefficient

μ_{oil}: oil viscosity

U_p: piston speed

Inertia force:

$$F_i = M_r a_p$$

M_r: ring mass

a_p: piston acceleration

Force due to resistance of squeezed oil:

$$F_s = \beta \mu_{oil} L_r V_r \left(\frac{W_r}{h_s}\right)^3$$

h_s: squeezed ring side clearance

W_r: ring width in radial direction

L_r: ring length in perimeter direction

V_r: ring velocity with respect to piston

$\beta = 0.1$ For partial area covered with oil

This force exists only when the ring is settling on the groove surface, and it always acts against the sum of the other three forces. This force was suggested by Furuhama

[43] to describe his experimental observation of the floating ring slowing down as it approached the groove surface.

Thus the ring motion equation becomes:

$$(F_p + F_f + F_1) - \beta \mu_{oil} L_r \frac{dh}{dt} \left(\frac{W_r}{h_s}\right)^3 = M_r \frac{d^2h}{dt^2} \quad (eq\ 6.1)$$

where h is the top side clearance as identified in Fig 6.3.

Solving this equation for h determines the ring position in the groove as a function of crank angle. The passage areas connecting the regions follow from h.

6.1.3 Gas flow equations

To model the flow, we follow the flow from the combustion chamber, plane (a), (Fig 6.4), to the crankcase, plane (d). The flow in the piston-cylinder crevice, region 1, is a fully developed laminar flow in a channel; hence it is a Coutte flow problem. Solving this problem for the presssure drop along crevice, plane (a) to plane (b), indicates 0.1-0.2% normalized presssure drop for the typical crevice size used in engines today. Therefore the pressure in region 1 can be assumed to be uniform and equal to the

cylinder pressure. We also assume that regions 2, 3, and 4 each have a uniform pressure.

It is assumed (justified in the previous sections), that the flow in regions behind and between the rings, regions 2, 3 and 4, is isothermal. The flow in the piston cylinder crevice region is assumed to be isothermal. This assumption is justified by the estimate of the characteristic time it takes for the gas to reach wall temperature; this characteristic time is 2 crank angle degrees. This finding is consistent with the measurements of Furuhama [46], who found the gas temperature in the piston cylinder crevice region to differ from the piston temperature by only a few degrees.

With the above assumptions, the continuity equations for the regions 2, 3 and 4 can be written:

$$\frac{m_{c_2}}{P_{o_2}} \frac{dP_2}{dt} = \dot{m}_{12} - \dot{m}_{23}$$

$$\frac{m_{o_3}}{P_{o_3}} \frac{dP_3}{dt} = \dot{m}_{13} + \dot{m}_{23} - \dot{m}_{34} - \dot{m}_{35} \qquad \text{(eq 6.2)}$$

$$\frac{m_{o_4}}{P_{o_4}} \frac{dP_4}{dt} = \dot{m}_{34} - \dot{m}_{45}$$

91

where:

P_i: i = 2,3,4   pressure in region i as in Fig 6.4

P_{oi}: i = 2,3,4   reference pressure in region i

m_{oi}: i = 2,3,4   reference mass in region i

$\dot{m}_{ij}$: mass flow rates through ring gap or ring side clearances.

In addition, we define:

$$\dot{m}_a = \frac{m_{o_1}}{P_{o_1}} \frac{dP_1}{dt} + \dot{m}_b$$

$$\dot{m}_b = \dot{m}_{13} + \dot{m}_{12}$$

$$\dot{m}_c = \dot{m}_{13} + \dot{m}_{23}$$

$$\dot{m}_d = \dot{m}_{35} + \dot{m}_{45}$$

where P_1: cylinder pressure

$\dot{m}_a$: mass flow rate through plane (a) as in Fig 6.4

$\dot{m}_b$: mass flow rate through plane (b)

$\dot{m}_c$: mass flow rate through plane (c)

$\dot{m}_d$: mass flow rate through plane (d); blowby

The mass flow rate through the ring gap is calculated by the orifice flow equation.

$$\dot{m} = C_d A g \rho C \eta \qquad (eq\ 6.3)$$

where C_d: discharge coeficent = 0.86

Furuhama [46]

Ag: ring end gap area

ρ: density downstream

C: sound speed downstream

η: compressibility factor

$$= \frac{2}{\gamma - 1} \left[(\frac{P_d}{P_u})^{2/\gamma} - (\frac{P_d}{P_u})^{(\gamma+1)/\gamma} \right]^{\frac{1}{2}}$$

$$= (\frac{2}{\gamma+1})^{\frac{\gamma+1}{2(\gamma-1)}} \quad \text{for choked flow}$$

As shown on Fig 6.5, the ring end gap area is the area bounded by the ring gap, the cylinder wall and the piston wall. To calculate this area, the effect of the chamfer between the piston surface and ring groove surface must be considered.

Fig 6.6 shows the ring side clearance flow model. To determine the mass flow rate through the ring side clearances, the flow is treated as a flow through a narrow channel of width h, length Wr, where Wr is the ring width (h/Wr= 0.01). The isothermal compressible flow through a differential length of this channel can be formulated as:

$$AdP - \tau_o dA_w = \dot{m}dU$$

$$\dot{m} = \rho Ua$$

$$P/\rho = \text{const}$$

$$\tau_o = 4f \cdot \frac{\rho U^2}{2}$$

where   A: area of the flow normal to flow

A_w: wetted area

U: velocity of the flow

f: friction coefficient

The solution of the equation for a channel of length Wr and pressures upstream and downstream of P_u and P_d is [47]:

$$(\frac{\dot{m}}{A})^2 = \frac{P_u{}^2 - P_d{}^2}{RT(\frac{4fW_r}{D} + 2\ell n \frac{P_u}{P_d})} \qquad \text{(eq 6.4a)}$$

where D=2h   hydraulic diameter

The flow through the ring side clearance is laminar (Rey (0)10) and therefore f = 24/Rey. Generally, $2Ln(P_u/P_d)$ <<$4fW_r/D$; therefore the above equation reduces to

$$\frac{\dot{m}}{A} = \frac{h}{24L_r} \frac{1}{\mu RT} (P_u - P_d{}^2) \qquad \text{(eq 6.4b)}$$

which can be derived from Poiseuille flow equation, i.e.,:

$$\frac{\dot{m}}{A} = \frac{h}{12L_r} \frac{\rho}{\mu} \frac{dP}{dx}$$

combined with P/ρ = const to allow for compressibility effects.

In summary, the problem has been formulated in terms of equation 6.1 for two compression rings and set of equations 6.2, which determine the pressures for regions behind and between the rings. These five differential equations, coupled with mass flow rate equations of 6.3 and 6.4 and ring force equations given in Appendix (6.1), were solved using a Runge-Kutta integration method.

6.1.4 Inputs and outputs of the model

The inputs to the computer include the pressure versus crank angle curve, engine geometry, and other relevant parameters, as all of which are shown in Table 6.1. The viscosity of the gas was found by [48]

$$\mu_{gas} = 3.3 \times 10^{-7} \times T^{0.7} \qquad \text{kg/ms}$$

and the viscosity of the oil by [45]

$$\mu_{oil} = e^{(\frac{1036}{T-178} - 9.84)} \qquad \text{NS/m}^2$$

The latter was checked against Streeter's data [49] and was found to be satisfactory.

The program outputs as a function of crank angle consist of the pressure trace for regions behind and between the rings, the mass flow rate between adjacent regions, the

forces on the rings and the position of the rings. Outputs of special interests are the net mass flow in or out of planes (a), (b), (c), and (d) (see Fig 6.4). The net mass flow through the ring gap is defined as g. The reader is urged to become familiar with the above notation in order to interpret the presented results.

Let us now present and discuss the following outputs: forces on the ring, ring motion, pressures of the regions, and integrated mass flow through the regions.

The engine is a V-6 231 cubic inch GM engine. This engine was used because simulation program results for this engine were available for use as input to the discussed model, and some experimental data were available for comparison to the model's predictions. The experimental work is the work of Wentworth [31] and the simulation program consists of work done at M.I.T [50]. The specifications of this engine are shown in Table 6.2. Unless otherwise stated, a midrange ring gap area, as specified in Table 6.2, is used.

Figure 6.7I shows pressure force, inertia force, friction force, and the sum of these forces acting on the top ring at engine operating condition of 2000 rpm and wide open throttle. The motion of both rings, the pressure in

the regions, and integrated mass flow through the planes are also shown in Fig 6.7II through 6.7VI for the same engine condition. Figure 6.7VI gives the net mass trapped between planes. It is evident from Fig 6.7I that of all of the forces acting on the ring, the pressure force has the highest magnitude and the friction force the lowest magnitude. Comparing the sum of forces acting on the top ring (Fig 6.7I) with the top ring motion (Fig 6.7II), it is apparent that as long as the sum of forces is positive, the ring seats in the bottom of the groove. As the sum becomes negative, the ring moves upward and finally settles on the top side of the groove. The slow motion of the ring as it approaches the other side of the groove is due to the retarding force of the oil film as the film is squeezed (this force is not shown in Fig 6.7I).

The top ring remains on the upper surface of the groove until the midpoint of the intake stroke; it then moves to the lower surface. For this engine condition the lower ring does not move to the upper surface until just after the end of the exhaust stroke, and it returns to the lower surface during the intake stroke.

97

The pressure trace (Fig 6.7III) indicates that during the compression stroke and first part of the expansion stroke, the pressure in the region behind the top ring (region 2) is the same as the combustion chamber pressure until the top ring moves upward. When the ring settles on the upper surface, the mass in region 2, as well as in regions 3 and 4, can return to the chamber through the ring gap only.

Figure 6.7IV shows the net mass that moves past into planes (a), (b), (c) and (d). The lowest curve is the blowby mass which crosses plane (d). For this geometry and set of operating conditions, about 1.3% of the combustion chamber mass is lost to the crankcase. The curve labled c,g shows the net mass that goes into the ring gap, which is the only flow across plane (c) when the ring sits in the bottom of the groove. Curve (a) shows the total mass which is trapped in all the crevice regions or lost to the crankcase; this mass is as high as 8% of the total mass in the combustion chamber.

Figure 6.7V displays the net mass flow out of planes (a) and (b) and through gap (g). Curve (a) indicates that 7% of the total combustion chamber mass returns to the cylinder. The amount which returns through the ring gap (curve g) is 0.7% of the combustion chamber mass (i.e.: 10%

of the total mass returned). These presented data are for the engine operating with top and bottom rings both having midrange gap size (Table 6.2). If the top ring gap size is large and the second ring gap size is small, the mass returning through the ring gap will be about 30% of the total mass returned to the combustion chamber.

Figure 6.7VI gives the net mass trapped between the different planes identified in Fig 6.4. The vertical difference between each curve at any crank angle is the mass which is trapped between these two planes at that crank angle. Obviously the top land (between planes (a) and (b)) crevice contains most of the mass. This is due to the large volume of crevice region and unrestricted connection to the main chamber cylinder. In contrast, the region behind the top ring is not always connected to the main chamber through the ring side clearance because of the ring motion.

The sum of the volumes of the regions between the rings and the region behind the second ring is more than the volume of the top land crevice, yet, due to the restriction of the ring gap, these regions together contain a smaller amount of mass than the mass of the top land crevice.

Let us emphasize that the above discussions apply to a particular engine geometry and set of engine operating conditions. Some of the above arguments will change if any of the conditions are changed. For example, a change in either ring gap area changes the amount of blowby, the amount of gas which flows back into the cylinder, and the ring motion. The temperature of the wall not only affects the amount of mass in each region (due to the isothermal assumption), but it also changes the oil viscosity which affects the ring motion. For a lower temperature, the top ring flutters longer than for the case studied. The longer the top ring flutters the more gas returns to the combustion chamber and the less gas escapes to the crankcase.

The results for a case of 4000 rpm are shown in Fig 6.8. Note that the wall temperature for this case is 470 K as compared to 450 K for the previous 2000 rpm case. This temperature is calculated using the outputs from the previously discused simulation program for the V-6 engine.

At this speed the inertia forces acting on the top ring is large enough to stop the top ring from moving during the expansion stroke. However, the second ring flutters at this speed. This fluttering causes a greater portion of the blowby to occur during this ring motion period. In fact for this case, 65% of the total blowby occurr up to 60 degrees

ATC, on expansion stroke, while for the previous case, 2000 rpm, only 25% of the total blowby occurred during this interval. As a result less gas returns to the cylinder through the ring gap (Fig 6.8V).

6.2 Verification of the Model

Let us now compare the available blowby data with the predictions of the model. Figure 6.9 shows how the blowby flow rate varies with the changes in the smaller ring gap area when two compression rings are used. The circles and the line through them are the experimental results of Wentworth [31] and the triangles are the model's prediction. For the model input, two combinations of three ring size gaps were used in the range of the actual production engine (refer to Table 6.2). There is good agreement between the model predictions and Wentworth's experimental results.

Figure 6.10 presents the model's prediction for one V-6 cylinder blowby as a function of engine speed at wide open throttle. The experimental results of Furuhama [51] in a smaller single cylinder engine (bore = 73 mm) are shown in the right lower corner of the figure. Both trends indicate that initial increase in speed decreases blowby slightly. As the speed further increases, blowby increases. Blowby finally drops if the speed is still further increased. The

sudden rise in blowby, as also discussed by Furuhama, is due to the fluttering motion of the second ring at higher speed. When the second ring flutters it loses its seal with the groove surface and, depending on duration of the fluttering period, some of the gas between the rings and behind the second ring is lost to the crankcase. At 5000 rpm for the engine used in our study, all the gas which passes through the top ring gap is lost to the crankcase--as if there was no second ring. Further increase in speed results in less blowby because the gas has less time to escape through the top ring gap.

Note that the amount of blowby could be in error as much as 50% if no ring motion was allowed; if on the other hand ring motion was allowed but the ring was assumed to jump instantaneously to the other side of the groove, an error as high as 30% could result in the amount of blowby.

6.3 Unburned Fraction of the Gas Trapped

In previous sections it was demonstrated that, in a typical case, the mass trapped in the crevice regions was as high as 8% of the mass inside the cylinder. Now the unburned and burned portion of this gas will be estimated. In order to do this, the composition of the gas flow across

plane (a) was considered separately from the gas which flows into the ring end gap.

6.3.1 Unburned fraction of gas into plane (a)

The gas which flows across plane (a) is the sum of all the gases which crosses the crevice entrance and accumulates in the regions 1,2,3 and 4 or escaped into the crankcase. The crevice entrance at plane (a) was modelled as shown on Fig 6.11. The portion of the crevice entrance which is exposed to burned gas is defined as length L_b and the rest of the crevice entrance which is exposed to unburned gas is defined as length L_u.

It was assumed that the mass flow rate per unit area into crevice is uniform over the entire crevice entrance. With this assumption, the unburned and burned portions of the mass flow rate into plane (a) are:

$$\dot{m}_u = \dot{m}_a \frac{L_u}{L_t}$$

$$\dot{m}_b = \dot{m}_a \frac{L_b}{L_t}$$

where $\dot{m}_a$: total mass flow rate into plane (a)

$\dot{m}_u$: unburned mass flow rate into plane (a)

$\dot{m}_b$: burned mass flow rate into plane (a)

L_u: the length of crevice exposed to unburned gas

L_b: the length of crevice exposed to unburned gas

$$L_t = L_u + L_b$$

To find L_u and L_b, assume that (Fig 6.12)

1 - Mean flame front is defined by mass fraction burned.

2 - Mean flame is a vertical plane.

3 - Unburned charge is compressed isetropically.

With the first two assumptions and only from geometry the volume of unburned gas is found to be

$$V_u(t) = \left[\frac{2L_u(t)}{B} - \sin\left(\frac{2L_u(t)}{B}\right) \right] V_t(t) \qquad \text{(eq 6.5a)}$$

B: bore

$V_u(t)$: volume at time t

$L_u(t)$: portion of crevice lenth exposed to unburned gas.

$V_t(t)$: total volume of the combustion chamber at time t

Due to Assumption 3, the volume of unburned gas could also be represented as:

$$V_u(t) = \frac{V_o}{(\frac{P(t)}{P_o})^{1/\gamma}} (1-x_b(t)) \qquad \text{(eq 6.5b)}$$

x_b: mass fraction burned

P(t): presssure at time t

P_o: a reference pressure before combustion

V_o: reference volume corresponds to P_o

Combining the above equations L_u can be calculated as function of time.

6.3.2 Unburned fraction of the gas in the regions beneath top ring

In Fig 6.11 the position of the ring gap with respect to the spark plug is marked by Lg. It was assumed that the gas flowing into the ring gap is unburned when $L_b/2 < L_g$ and is burned when $L_b/2 > L_g$. We further assumed that the contents of region 2, behind the top ring, mixes with that of regions 3 and 4 when the top ring is pushed to the upper surface of the groove.

Using this approach, we established that the unburned portion of the gas in the regions beneath the top ring was 80-95% when the gap was farthest from the spark plug, and it was 40-60% if the gap was just under the spark plug. (Benett [52] reported 85% of the blowby as unburned fuel)

6.3.3 Significance of the unburned fuel trapped in the crevice regions

Table 6.3 summarizes the total amount of gas which flows in and out of the crevice regions over one cycle with the engine operating at wide open throttle and at 2000 rpm. (This is the same case that was presented on Fig 6.7.) The same table also displays our estimate of the unburned gas which is lost to blowby or returns back to cylinder for the

two cases of ring gap being farthest from or closest to the spark plug.

The results shown in this table indicate that when the gap is farthest from the spark plug, about 4% (5360 ppm HC, when diluted with the burned gas) of the unburned fuel returns back to the cylinder and 1% is lost to the crank case. This indicates that a total of 5% of the fuel has escaped combustion. In the case where the gap is closest to the spark plug, the amount of unburned fuel back to the cylinder is 3.7% (4960 ppm); the amount into the crank case is 0.5%, and the sum of fuel that escapes combustion is 4.2%. Since today's engines return the blowby gas back into the intake manifold, the above data indicate that 4% of the fuel could escape efficient combustion. If these data are assumed to be correct, the crevice regions inside this engine could be responsible for a 4% loss in the efficiency of the engine. Other calculations we have done show that the percentage of the fuel escaping efficient combustion ranges from 3% to 8%. The highest percentage results from the engine operating with cold walls (Section 6.5.3) and large size ring gap (Table 6.2).

Parse and coworkers [53] designed a new ring mounted directly at the top of the piston which reduced both hydrocarbon emission and blowby. They also observed 10% power improvement. A part of this power improvement could be due to the recovery of the fuel.

6.4 Comparison Between The Predicted HC And Experimental HC

To assess the validity of the data discussed above, let us now compare our calculations of unburned fuel flow back to the cylinder with the exhaust hydrocarbon measurements of Wentworth. For this comparison to be meaningful, the incylinder oxidation and exhaust system oxidation should be considered. The theoretical work of Caton [54] verified by the experimental work of Mendillo[55] indicates that at the conditions considered about 50% of the hydrocarbons are oxidized in the exhaust system. Therefore as shown in Table 6.4, an additional factor of 2 reduction incylinder oxidation is required to bring the level of our estimate of 4940 ppm (incylider hydrocarbon) to the Wentworth exhaust measurments of 1320 ppm for the same condition. This level of incylinder oxidation is in the range estimated by Daniel[56]. Note that, Wentworth[31] reported 100 ppm C6 measured with a nonedispersive infrared(NDIR). However, in

a later paper[57], he measured 220 ppm C6 using a flame ionization (FI) analyzer.

The same table shows another comparision between the model predictions and exhuast measurments. The data are for a 1.6 liter Toyota engine operating at 1600 rpm and 390 kPa load and equivalence ratio 0.98. The hydrocarbon levels at exhaust tale and exhuast valve are both experimental results of Matsumoto et al[23]. This comparison indicates that a 20% incylinder oxidation is required to bring the level of ppm (model prediction) to 3400 ppm measured at the exhaust valve. The lower percentage of the incylinder oxidation for this case is due to different engine operating conditions, especially lower speed.

6.5 Parametric Study

In this section we use the model to study the variation of the hyrocarbon flow from the crevice regions with geometry, wall temperature, piston speed and load. Wherever possible, experimental data will be used to verify the predicted trend.

6.5.1 Gap area

Figures 6.13A,B, and C show the amount of hydrocarbon returning to the combustion chamber (curve a) as a function of ring gap area. Each figure displays the effect of the ring gap area on this hydrocarbon flow when the top ring gap area is held fixed. Curves (g) and (d) on each figure represent the amount of hydrocarbon returning through the top ring gap (g) and the amount that is lost to blowby (d).

The following conclusions can be drawn from these figures:

I. Increasing the second ring gap area when the top ring gap area is fixed causes:

    A. The mass of unburned fuel returning through the top ring gap (curve g) decreases.

    B. The total mass of unburned fuel returning to the combustion chamber (curve a) decreases.

    C. The mass of unburned fuel lost to blowby increases. This increase is such that the total unburned fuel escaping efficient combustion (sum of curves a and b) remains nearly constant.

II.   Regardless of the ring gap size the unburned fuel

escaping efficient combustion (sum of curves a and b) is minimum when the top ring gap area is small and is maximum when the top ring gap area is large.

III. The total unburned fuel returning to the combustion chamber (a) is minimum when the top ring gap area is in the mid range, and the lower compression ring gap area is large.

IV. The unburned fuel lost to blowby is maximum when both the top ring and second ring gap areas are large.

Figure 6.14 is generated using the data from the previous figure, and it shows the amount of unburned fuel returning to the combustion chamber versus the amount of fuel lost to blowby. Each line is for a given top ring area. Similar trends were observed experimentally by Wentworth[27,31].

6.5.2 Volume reduction

Figure 6.15 shows the effect of reduction in piston top land crevice volume on the HC returning to the cylinder (a) and lost to blowby (d). Reducing this volume has a significant effect on the former, but no effect on the latter. This figure indicates that if in this engine top land crevice volume is removed, a 70% reduction in HC

returning to the combustion chamber could be achieved. Wentworth [27] observed a 50% reduction in HC emission of the same engine when piston cylinder crevice volume was virtually eliminated.

Figure 6.16 displays the effect of reduction in volume of the region behind the top ring (Vol 2) on hydrocarbon returning to the combustion chamber (a) and to blowby (d). This figure indicates that a 75% reduction in this volume results in a 20% reduction in HC. The reduction is not linear with volume, as it was for Vol 1. This is due to ring motion. The unburned fuel lost to blowby slightly decreases with a reduction in this volume.

Figure 6.17 shows the result of a reduction in Vol 3 and Vol 4 of 2000 rpm. The graph is plotted versus the sum of these two volumes because they have equal pressures at this condition. Apparently, the reduction of these volumes slightly reduces the HC returninng to the cylinder, but at the same time the blowby is increased at the same rate. In fact, the sum of fuel lost remains nearly the same.

112

6.5.3 Wall temperature

Figure 6.18a displays the predicted amount of hydrocarbon returning to the cylinder versus the wall temperature for the two orientations of the top ring gap. The solid line and the dashed line represent the gap located closest to and farthest from the spark plug, respectively. Fig. 6.18b shows the measurements of Lavie et al. [58] in a CFR engine operating at 1250 rpm, 310 kPa load, and equivalence ratio of 0.9. The experimental data are hydrocarbon measurements at the exhaust tale and plotted versus the coolant wall temperature. These experimental data are presented to illustrate the trend of the curve and should not be compared to the calculations which are in cylinder hydrocarbon, in another engine, and operating at different operating conditions. The calculated trend shows that a one degree reduction in wall temperature results in 20 ppm increase in the hydrocarbon returning to the combustion chamber. This increase is largely due to the rise in the gas density (isothermal assumption effect) and partially due to the longer ring fluttering period at lower temperatures (oil viscosity effect). Another parameter, ring gap area change, is neglected in these calculations. At lower temperatures the ring gap area is larger; thus the slope of the curve should further increase.

6.5.4 Engine speed

Figure 6.19 shows that as the engine speed is increased, the amount of hydrocarbon returning to the combustion chamber initially increases and then decreases. The experimental results indicate that the hydrocarbon out of the exhaust pipe always decreases as the engine speed is increased. The disagreement between the predicted trend and experimental trends could be due to the substantial variation of incylinder oxidation and exhaust system oxidation with speed. Caton [54] predicts 30% more exhaust oxidation for 2000 rpm than for 1200 rpm.

6.5.5 Load

Figure 6.20 shows the variation of hydrocarbon returning to the cylinder (white triangles) as a function of intake depresssion for a V-6 engine operating at 1200 rpm. The dark triangles represent the calculated level of hydrocarbon when the exhaust system oxidation is considered. The circles illustrate the experimental results of Wentworth[31] in the same engine at the same operating conditions.

Note that the experimental data show a sharper increase in HC with intake depression than the calculated data. The reader should be reminded that the combustion chamber pressure trace and other pertinent parameters used as input to the computer model are generated by a simulation program[50] and are not actual measurements. This factor may therefore account for part of the disagreement between the calculated and the experimental trend.

THIS PAGE WAS INTENTIONALLY LEFT BLANK

CHAPTER 7

CONCLUSIONS

7.1 Visualization of the Flow

The use of a square cross-section transparent side-wall spark-ignition engine for flow visualization through the complete engine cycle has been successfully demonstrated. The engine operating characteristics were shown to be sufficiently close to those of a conventional spark-ignition engine for the results to provide useful insights into the flow fields and the flame structure in real engines. The observations and insights are summarized below.

(i) For throttled operation when the intake valve opens, the backflow from the cylinder into the intake system is evident, and the bulk gas in the cylinder is drawn towards the valve. Also, the gas in the top land crevice is observed to expand out slowly into the cylinder. This flow has a Reynolds number of order 100.

(ii) The intake flow enters the cylinder as a conical jet which travels to and interacts with the cylinder wall.

(iii) A vortex type flow in the upper corners of the cylinder, set up by the intake jet, is visible in the Schlieren movies. This rotating motion in the upper corners persists through compression, combustion, and expansion.

(iv) The turbulent flame which develops from the spark discharge propagates as an approximately spherical though irregular front. The flame zone is thick, the front to back distance being 10-15 mm, and a detailed internal flame structure is evident.

(v) Only a fraction (of order one half during the earlier part of the burning process) of the mixture contained behind the propagating flame front is fully burned.

(vi) The characteristic burning time of mixture within the flame is of order a few milliseconds (average 1.8 ms). This gives a characteristic turbulent flame length scale of 14 mm (which is comparable to the observed flame thickness), and a characteristic laminar burning length scale of 1.3 mm.

(vii) The flame front shows both larger scale irregularities and a smaller scale structure. The larger scale irregularities are of order 10 mm in size (about 1/3 the clearance height) and smaller scale structure at the flame front appears to be of order 2.5 mm in dimension.

(viii) The spark discharge is observed as a thin column between the electrodes which then grows as a flame kernel develops around the spark. Once the kernel fills the electrode gap, it develops irregularities. Once it extends beyond the electrodes (scale 5 mm or greater), its appearance is similar to that of a fully developed turbulent flame.

(ix) A comparison of pictures from different cycles shows different degrees of flame development at early times, and different flame center motion and front shape. These initial differences lead to substantial later differences in fully developed flame front position and shape. The effect of cycle-by-cycle variations in mixture motion on the flame can be observed. These differences in flame development and propagation can be related to the value and time of occurrence of peak pressure.

(x) During expansion (following time of peak cylinder pressure) flow of denser gas out of the spark plug crevice and the region between the piston and the cylinder walls was observed. Gas from the crevice volume behind and between the rings issued from the corners of the gap between the piston crown and the walls as a jet, late in the expansion process, when the cylinder pressure fell below the pressure in this crevice region. These crevice gases are expected to have a high unburned hydrocarbon concentration.

(xi) The blowdown flow was observed to entrain the denser thermal boundary layer gas off the cylinder head and upper part of the cylinder wall. Some of the gas from the crevice between the piston crown and cylinder wall also leaves the cylinder during blowdown.

(xii) During the exhaust stroke, the roll-up of a vortex in the corner between the cylinder-wall piston-crown-surface was observed, though the vortex was not always stable in this engine geometry.

7.2 Modeling the Flow-Visualization Engine's Crevice Flow

(i) The flow behind and between the rings was found to be satisfactorily approximated as an isothermal flow.

(ii) A system model of orifices and volumes for the regions behind and between the rings is found to predict the timing of the jet out of these regions.

(iii) The model predicts that some of the gas trapped in the top land crevice should expand out prior to the observed jet from the regions behind and between the rings. We believe that this slow moving flow (Reynolds number of order 100) may remain close to the cylinder walls and be obscured from observation by the thick thermal boundary layer. This layer is observed being scraped off the wall and rolled into vortex during exhaust stroke.

7.3 Crevice Flow from Simulated Real Engine Crevice Regions

The crevice regions of a real engine were simulated as follows: The ring belt of the conventional piston was cut just above the oil ring and then fitted into a piston holder having an inner circular bore corresponding to the conventional cylinder size. This assembly was then secured on the top of the square piston engine. The assembly was designed such that the entrance to the inner piston top land crevice was removed from the obscuring thermal boundary layer. The following conclusions were possible from this experiment and from the flow model for these simulated crevice regions.

(i) With the geometry of a real piston assembly, a jet flow similar to the one in the square piston engine occurs. This jet type flow is from ring gap.

(ii) A flow is observed expanding out of the top land crevice of the inner circular piston of this assembly. This flow is similar to the one that was predicted for the square piston engine but was obscured from observation by the dark layer on the wall.

7.4 Real Engine Model

The following conclusions are obtained from an isothermal flow model coupled with a ring motion model for a V-6 engine:

(i) The calculated blowby flow rate versus ring gap area agrees well with the experimental results in the same engine.

(ii) The blowby flow rate trend with speed is similar to the one that is observed experimentally in another engine.

(iii) At typical engine operating conditions about 8% of the combustion chamber mass is trapped into crevice regions. From this amount about 6% returns back to

cylinder, and the remaining 2% is lost to blowby.

(iv) The portion of the fuel that is trapped in the crevice regions or lost to blowby is about 5% of the fuel.

(v) About 4% of the fuel trapped in the crevice regions returns to the combustion chamber.

(vi) Recovery of the fuel lost into the crevice regions signifies a 4% recovery in fuel economy for typical engine operating conditions. If the engine walls are cooler and ring gap size larger (still in the engine operating conditions range and production range), the percentage loss in efficiency will be as high as 8%.

(vii) Increasing the second ring gap area when the top ring gap area is fixed causes:

A. The mass of unburned fuel returning through the ring gap decreases.

B. The total mass of unburned fuel returning to the combustion chamber decreases.

C. The mass of unburned fuel lost to blowby increases. This increase is such that the total unburned fuel escaping efficient combustion remains nearly constant.

(viii) Regardless of the ring gap size the unburned fuel escaping efficient combustion (sum of the amount of fuel returning to combustin chamber and the amount lost to blowby) is minimum when the top ring gap area is small and is maximum when the top ring gap area is large.

(ix) The total unburned fuel returning to the combustion chamber is minimum when the top ring gap area is in the midrange and the lower compression ring gap area is large.

(x) The unburned fuel lost to blowby is maximum when both the top ring and second ring gap areas are large.

(xi) The model predictions on the effect of reducing the volumes of the crevice regions are as follows:

A. Reducing the top land crevice volume has the most significant effect on reduction of the unburned fuel trapped and returning to the combustion chamber, but it has no effect on the amount of blowby.

B. Reducing the volume behind the top ring has the second most important effect on the unburned fuel trapped and returning to the combustion chamber.

    C.   Reducing the volume of the regions beneath the top ring slightly reduces the amount of unburned fuel returning to the combustion chamber, but at the same time it increases the blowby at the same rate.

(xii) The model predicts an average 20 ppm increase in the amount of unburned fuel returning to the combustion chamber with one degree reduction in wall temperature.

(xiii) As the engine speed is increased, the amount of unburned fuel returning to the combustion chamber initially increases and then decreases.

(xiv) The amount of unburned fuel returning to the combustion chamber is predicted to increase with reduction in the engine load. But the predicted rate of increase is slower than the measurements.

THIS PAGE WAS INTENTIONALLY LEFT BLANK

REFERENCES

1. Heywood, J.B., "Pollutant Formation and Control in Spark-Ignition Engines", Progress in Energy and Combustion Science, Vol. 1, pp. 135-164, 1976.

2. Ekchian, A. and Hoult, D.P., "Flow Visualization Study of the Intake Process of an Internal Combustion Engine", SAE Paper 790095, 1979.

3. Rassweiler, G.M. and Withrow, L., "Motion Pictures of Engine Flames Correlated with Pressure Cards", SAE Transactions, Vol. 42, No. 5, 1938.

4. Nakanishi, K., Hirano, T., Inoue, T. and Ohigashi, S., "The Effects of Charge Dilution on Combustion and Its Improvement -- Flame Photograph Study", SAE Paper 750054, SAE Transactions, Vol. 84, p. 352, 1975.

5. Alcock, J.F. and Scott, W.M., "Some More Light on Diesel Combustion", Proc. Inst. Mech. Engrs. (A.D.), No. 5, pp. 179-200, 1962-63.

6. Taylor, C.F., Taylor, E.S., Livengood, J.C., Russel, W.A. and Leary, W.A., "The Ignition of Fuels by Rapid Compression", paper presented at the SAE Annual Meeting, Detroit, Michigan, January 9-13, 1950.

7. Matekunas, F.A., "A Schlieren Study of Combustion in a Rapid Compression Machine Simulating the Spark Ignition Engine", Seventeenth Symposium (International) on Combustion, p. 1283, 1978.

8. Oppenheim, A.K., Chong, R.K., Teichman, K., Smith, O.T., Sawyer, R.F., Hom, K. and Stewart, H.E., "A Cinematographic Study of Combustion in an Enclosure Fitted with a Reciprocating Piston", Conference on Stratified Charge Engines", Inst. Mech. Engrs., London, England, 1976.

9. Ishikawa, N. and Daily, J.W., "Observation of Flow Characteristics in a Model I.C. Engine Cylinder", SAE Paper 780230, 1978.

10. Iinuma, K. and Iba, Y., "Studies of Flame Propagation Process", JARI Technical Memorandum, No. 10, pp. 59-78, December, 1972.

11. Iinuma, K. and Iba, Y., "Studies of Flame Propagation (Structure of Flame Zone and Burning Velocity)", JARI Technical Memorandum, No. 15, pp. 44-51, December, 1973.

12. Hanson, S.P., "The Design and Testing of a Flow Visualization Engine", S.M. Thesis, M.I.T., 1978.

13. Daniel, W.A., Sixth Symposium (International) on Combustion, P. 886, Reinhold, New York, 1957.

14. Adamczyk, A.A. and Lavoie, G.A., "Laminar Head-On Flame Quenching--A Theoretical Study", SAE Transactions, Vol. 87, SAE Paper 780969, 1978.

15. Westbrook, C.K., Adamczyk, A.A. and Lavoie, G.A., The Combustion Institute, Eastern Section, Berkeley, October, 1979.

16. LoRusso, J.A., Lavoie, G.A. and Kaiser, E.W., "An Electrohydraulic Gas Sampling Valve with Application to Hydrocarbon Emissions Studies", SAE Paper 80045, 1980.

17. Weiss, P. and Keck, J.C., "Fast Sampling Valve Measurements of Hydrocarbons in the Cylinder of a CFR Engine", SAE Paper 810149, 1981.

18. Bregner, P., Eberino, H. and Pokorny, H., Third Alcohols Symposium, Asilomar, May, 1979.

19. Adamczyk, A.A., Kaiser, E.W., Cavolowsky, J.A. and Lavoie, G.A., 18th Symposium (International) on Combustion, Waterloo, Canada, August, 1980.

20. Sellnau, M.C., Springer, G.S. and Keck, S.C., "Measurements of Hydrocarbon Concentrations in the Exhaust Products from a Spherical Combustion Bomb", SAE Paper 810148, 1980.

21. Tabaczynski, R.J., Heywood, J.B. and Keck, J.C., "Time-Resolved Measurements of Hydrocarbon Mass Flow Rate in the Exhaust of a Spark-Ignition Engine", SAE Transaction Vol. 83, SAE Paper 72112, 1972.

22. Daniel, W.A., Wentworth, J.T., "Exhaust Gas Hydrocarbons-- Genesis and Exodus", SAE Technical Progress Series, Vol. 6, 1962.

23. Matsumoto, K., Inoue, T., Nabanishi, K. and Okumura, T., "The Effect of Combustion Chamber Design and Compression Ratio on Emissions, Fuel Economy and Octane Number Requirement", SAE Paper 770193, 1977. Also, SP-414.

24. Kaiser, E.W., Adamczyk, A.A. and Lavoie, G.A., 18th Symposium (International) on Combustion, Waterloo, Ontario, Canada, August, 1980.

25. Smith, O.I., Westbrook, C.,. and Sawyer, R.F., The Combustion Institute, Canadian Section, Branff, Alberta, Canada, May, 1977.

26. Goto, K., Ichimiya, T., Hirata, T. and Sato, Y., "Study on the Genisis of Hydrocarbons in the Combistion Chamber of a Gasoline Engine", JSAE (SAE of Japan) Review, No. 2, 1980.

27. Wentworth, J.T., "The Piston Crevice Volume Effect on Exhaust Hydrocarbon Emissions", Combustion Science and Technology, Vol. 4, pp. 97-100, 1971.

28. Furuhama, S., Tateishi, Y., "Gases in Piston Top-Land Space of Gasoline Engine", Bulletin of JSAE, No. 5, 1973.

29. Holman, J.P., "Experimental Methods for Engineers", 2nd Edition, McGraw-Hill, 1971.

30. LoRusso, J.A., "Combustion and Emissions Characteristics of Methanol, Methanol-Water and Gasoline-Methanol Blends in a Spark-Ignition Engine", M.S. thesis, Mech. Eng. Dept, M.I.T., 1976.

31. Wentworth, J.T., "Piston and Ring Variables Affect Exhaust Hydrocarbon Emissions", SAE Paper 680109, 1968.

32. Namazian, M., Hansen, S., Lyford-Pike, E., Sanchez-Barsse, J., Heywood, J., Rife, J., "Schlieren Visualization of the Flow and Density Fields in the Cylinder of a Spark-Ignition Engine", SAE Paper 800044, 1980.

33. Lyford-Pike, E.J., "Measurement and Analysis of Thermal Boundary Layer Thicknesses in the Cylinder of a Spark-Ignition Engine", S.M. Thesis, M.I.T., August, 1980.

34. Ekchian, A., Heywood, J.B., and Rife, J.M., "Time Resolved Measurements of the Exhaust from a Jet Ignition Prechamber Stratified Charge Engine", SAE Paper 770043, SAE Transactions, Vol. 86, 1977.

35. Tabczynski, R.J., Hoult, D.P., and Keck, J.C., "High Reynolds Number Flow in a Moving Corner", J. Fluid Mech. 42, pp. 249-255, 1970.

36. Blizard, N.C., and Keck, J.C., "Experimental and Theoretical Investigation of Turbulent Burning Model for Internal Combustion Engines", SAE Paper 740191, SAE Transactions, Vol. 83, 1974.

37. Tabaczynski, R.J., Fergason, C.R., Radhakrishnan, K., A Turbulent Entrainment Model for Spark-Ignition Engine Combustion", SAE Paper 770647, 1977.

38. Tabaczynski, R., Trinker, F.H., Shannon, B.A.S., "Further Refinement and Validation of a Turbulent Flame Propagation Model for Spark-Ignition Engines", Combustion and Flames 39, pp. 111-121, 1980.

39. Beretta, G.P., Rashidi, M., and Keck, J.C., "Thermodynamic Analysis of Turbulent Combustion in a Spark-Ignition Engine. Experimental Evidence", The Combustion Institute, Western State Section, April, 1980.

40. Metghalchi, M., "Laminar Burning Velocity of Mixtures of Air with Indolene, Isooctane, Methanol and Propane", Ph.D. Thesis, Mech. Eng. Dept., M.I.T., 1980.

41. Weinberg, F.J., "Optics of Flames", Butterworth and Co., Ltd., 1963.

42. Beaubien, S.J., Cattaneo, A.G., "Phenomena in a Motored Glass Cylinder Engine", SAE Journal, Vol. 54, October, 1946.

43. Furuhama, S., Hiruma, M. and Tsuzita, M., "Piston Ring Motion and its Influence on Engine Tribology", SAE Paper 790860, 1979.

44. Furuhama, S., Hiruma, M., "The Relationship Between Piston Ring Scuffing and the Formation of Surface Profile:, Piston Ring Scuffing Conference, C67175.

45. Rangert, B., "Hydrodynamic Piston Ring Lubrication with Reference to Lubricating Oil Consumption", Doctorsavhandlingar vid Chalmers Tekniska Högskola, 1974.

46. Furuhama, S. and Tada, T., "On the Flow of the Gas through the Piston-Rings", JSME, Bulletin, Vol. 4, No. 16, 1961.

47. Shapiro, A.H., "The Dynamics and Thermodynamics of Compressible Fluid Flow", Vol. I, pp. 182-183, The Ronald Press Company, New York, 1953.

48. Mansouri, S.H., Heywood, J.B., "Correlations for the Viscoscity and Prandtl Number of Hydrocarbon-Air Combustion Products", Combustion Science and Technonogy, Vol. 23, pp. 251-256, 1980.

49. Streeter, V.L., "Handbook of Fluid Dynamics", McGraw-Hill Publishing Company, Inc., 1961.

50. Heywood, J.B. and Watts, D.A., "Simulation Studies of the effect of Turbocharging and Reduced Heat Transfer on Spark-Ignition Engine Operation", SAE Paper 8000289, 1980.

51. Furuhama S., Hiruma, M., "Some Characteristics of Oil Consumption Measured by Hydrogen Fueled Engine", ASLE, Vol. 34, December, 1978.

52. Bennett, P.A., Murphy, C.K., Jackson, M.W. and Randall, R.A., "Reduction of Air Pollution by Control of Emission from Automotive Crankcases", SAE Transactions, Vol. 68, 1960.

53. Prasse, H.F., McCormic, H.E. and Anderson, R.D., "New Piston Ring Innovations to Help Control Automotive Engine Emissions", SAE Paper 730006, 1973.

54. Caton, J.A., Heywood, J.B., "Models for Heat Transfer, Mixing, and Hydrocarbon Oxidation in an Exhaust Port of a Spark-Ignited Engine", SAE Paper 8000290, 1980.

55. Mendillo, J.V., and Heywood, J.B., "Hydrocarbon Oxidation in the Exhaust Port of a Spark-Ignigion Engine", SAE Paper 810019, 1981.

56. Daniel, W.A., "Why Engine Variables Affect Exhaust Hydrocarbon Emission", SAE Paper 700108, 1970.

57. Wentworth, J.T., "More on Origins of Exhaust Hydrocarbons--Effects of Zero Oil Consumption, Deposit Location, and Surface Roughness", SAE Paper 720939, 1972.

58. Lavoie, G.A., LoRusso, J.A. and Adamczyk, A.A., "Hydrocarbon Emission Modeling for Spark Ignition Engines", Presented at the General Motors Symposium on Combustion Modeling as Reciprocating Engines, Warren, Michigan, 1978.

59. Aue, G.K., "About the Mechanism of a Piston Ring Seal", 10th International Congress on Combustion Engines, Cl MAC, 1973.

60. McGeehan, J.A., "A Literature Review of the Effects of Piston and Ring Friction and Lubricating Oil Viscosity on Fuel Economy", SAE Paper 780673, 1978.

TABLE 2.1

Geometric Details of Transparent Engine

Bore (square), mm	82.6
Stroke, mm	114.3
Compression Ratio	4.8-5.2
Connecting rod length, mm	254.0

Intake Valve
  Diameter, mm   31.5
  Maximum lift, mm   5.7
  Opens at 10° ATC
  Closes at 34° ABC

Exhaust Valve
  Diameter, mm   31.5
  Maximum lift, mm   6.0
  Opens at 40° BTC
  Closes at 15° ATC

TABLE 2.2

Comparison of Transparent Engine with Typical Current Production Engine

	Transp. Engine	Current Engines
Compression ratio	4.8–5.2	8.5
Bore, mm	82.5 (square)	100
Top Land height, mm	12	8
Groove width, mm	6.35	2.2
Piston cylinder clearance, mm at top land	0.38* left 1.4* right 0.9* window	0.38*
Volume behind 1st set of rings, cm^3	4.0	0.84
Passage area caused by ring gaps, mm^2	2.3	0.5

---

*Measured cold.

TABLE 2.3

Engine Operating Conditions

Engine speed	810, 1380 rev/min
Inlet pressure	0.5, 0.7, 0.9 atm
Inlet temperature	$25^{\circ}C$
Exhaust pressure	1 atm
Equivalence ratios (fuel/air)	1.15
Fuel	propane

Spark-timing:
1380 rpm, 0.5 atm inlet pressure	55° BTC
1380 rpm, 0.7 atm inlet pressure	44° BTC
1380 rpm, 0.9 atm inlet pressure	38° BTC
810 rpm, 0.7 atm inlet pressure	65° BTC

TABLE 5.1

Summary of the predicted flow timing (crank angle degrees ATC) through planes (a)* and (b) toward the combustion chamber

	Isothermal	Adiabatic
Flow out of plane (a) (top land entrance)	38	42
Flow out of plane (b) (plane separating top land crevice and region behind the ring)	116	106

*To identify planes (a) and (b), see Fig 5.1.

TABLE 5.2

Geometry of the Conventional Piston Used To Study Crevice Flow

Piston bore, mm	76.9
Cylinder bore, mm	77.5
Storke, mm	77.0
Top land, mm	6.8
Second Land, mm	3.
Ring side clearance, mm	0.05
Ring gap, mm	0.25
Top land crevice volume, cm^3	0.56
Volume behind the top ring, cm^3	0.27
Volume between top and second ring, cm^3	0.28
Clearance volume, cm^3	45.4

TABLE 6.1

Inputs to the Computer Program

Name used in the program	Description	Source of entry
BORE, m	Bore	V6DATA.FTN
RCR, m	Radius of the crank	V6DATA.FTN
CONLEN, m	Connecting rod length	V6DATA.FTN
DV, cc	Displacement volume	V6DATA.FTN
DELTA, cm	Piston cylinder crevice	DATA.DAT
CRVH, cm	Top land crevice height	DATA.DAT
VOL1, cc (calculated in the program)	Top land crevice volume	DATA.DAT
VOL2, cc	Volume of region behind the top ring	DATA.DAT
VOL3, cc	Volume of region between rings	DATA.DAT
VOL4,cc	Volume of region behind the second ring	DATA.DAT
A13, cm^2	Top ring gap area	DATA.DAT
A35, cm^2	Second ring gap area	DATA.DAT
RW1,RW2, m	Ring width of 1st and 2nd ring	V6DATA.FTN
RT1,RT2, m	Ring thickness of 1st and 2nd ring	V6DATA.FTN
RMASS1,RMASS2, kg	Mass of the 1st and 2nd ring	V6DATA.FTN
CT10,CT20, m	First and 2nd ring side clearance	V6DATA.FTN
TW, K	Wall temperature	DATA.DAT
NUO, m^2/sec	Dynamic viscosity of the charge at initial conditions	V6DATA.FTN
MUOIL, $N.S/m^2$ (calculated in the program)	Kinematic viscosity of the oil	V6DATA.FTN
WTMOL	Molecular weight of the charge	V6DATA.FTN
P1, atm	Pressure trace of the combustion chamber	P files
PIO,I=1,2,3,4, atm	Initial pressure of regions	Terminal
XB	Mass fraction burned trace	X file
RPM	Piston speed	Terminal

TABLE 6.2

Specifications of the V-6 Engine

Compression ratio	8.1
Bore, cm (in)	9.65 (3.8)
Stroke, cm (in)	8.64 (3.4)
Connecting rod length, cm (in)	15.15 (6.)
Displacement volume, cm^3	631.9
Ring gap area; production range [31], cm^2 small midrange large	1.4×10^{-3} 2.6×10^{-3} 4.1×10^{-3}
Dead volume	89. (100%)
Piston cylinder crevice volume, vol. 1, cm^3	0.93 (1.05%)
Region behind first ring, vol. 2, cm^3	0.467 (0.52%)
Region between rings, vol. 3, cm^3	0.681 (0.77%)
Region behind second ring, vol. 4, cm^3	0.467 (0.52%)
Total crevice volume	2.55 (2.86%)
Equivalence ratio	0.95

TABLE 6.3

Summary of the Amount of Gas in and out of Crevice Regions for a V-6

Operating at 2000 rpm and Wide Open Throttle

		% mass	ppm
	Total gas in all crevice regions	.8.23	
	Total gas back to combustion chamber	7.0	
	Total gas to blowby	1.23	
Ring gap farthest from spark plug	Unburned back to combustion chamber	4.	5360
	Unburned to blowby	1.05	
	Total unburned lost	5.05	
Ring gap closest to spark plug	Unburned back to combustion chamber	3.7	4960
	Unburned to blowby	0.5	
	Total unburned lost	4.2	

TABLE 6.4

Comparison Between Predicted and

Experimental Hydrocarbon Level

Engine	HC Returning to cylinder predicted	Incylinder oxidation	Exhaust port HC	Exhaust Oxidation	HC measured at exhaust
V-6	4960	50%	2640 Estimate	50% Estimate [54]	1320
Toyota	4300	20%	3400 Measured		2100

THIS PAGE WAS INTENTIONALLY LEFT BLANK
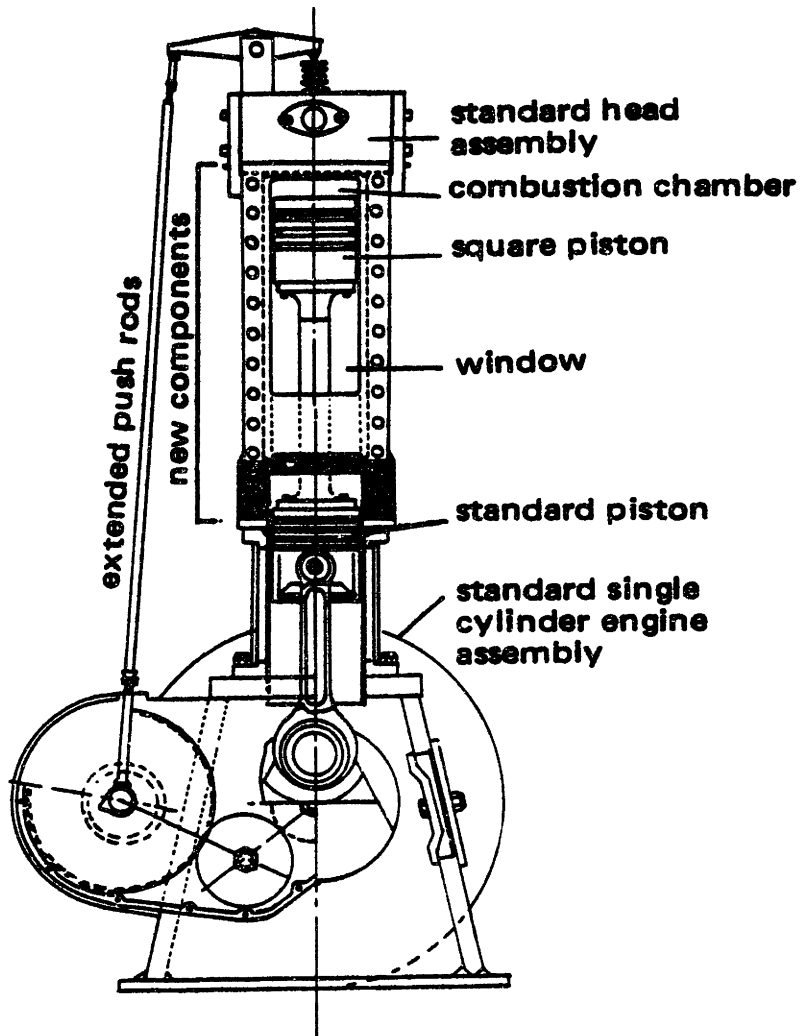
Fig 2.1 — Schematic of the new square piston
visualization engine

Head

Clamping Wall

Weld

Piston Rings

Aluminum Square Piston

Quartz Glass Walls

Split Connecting Rod

Weld

Felt Seal

Adaptor Base Plate

CFR Piston
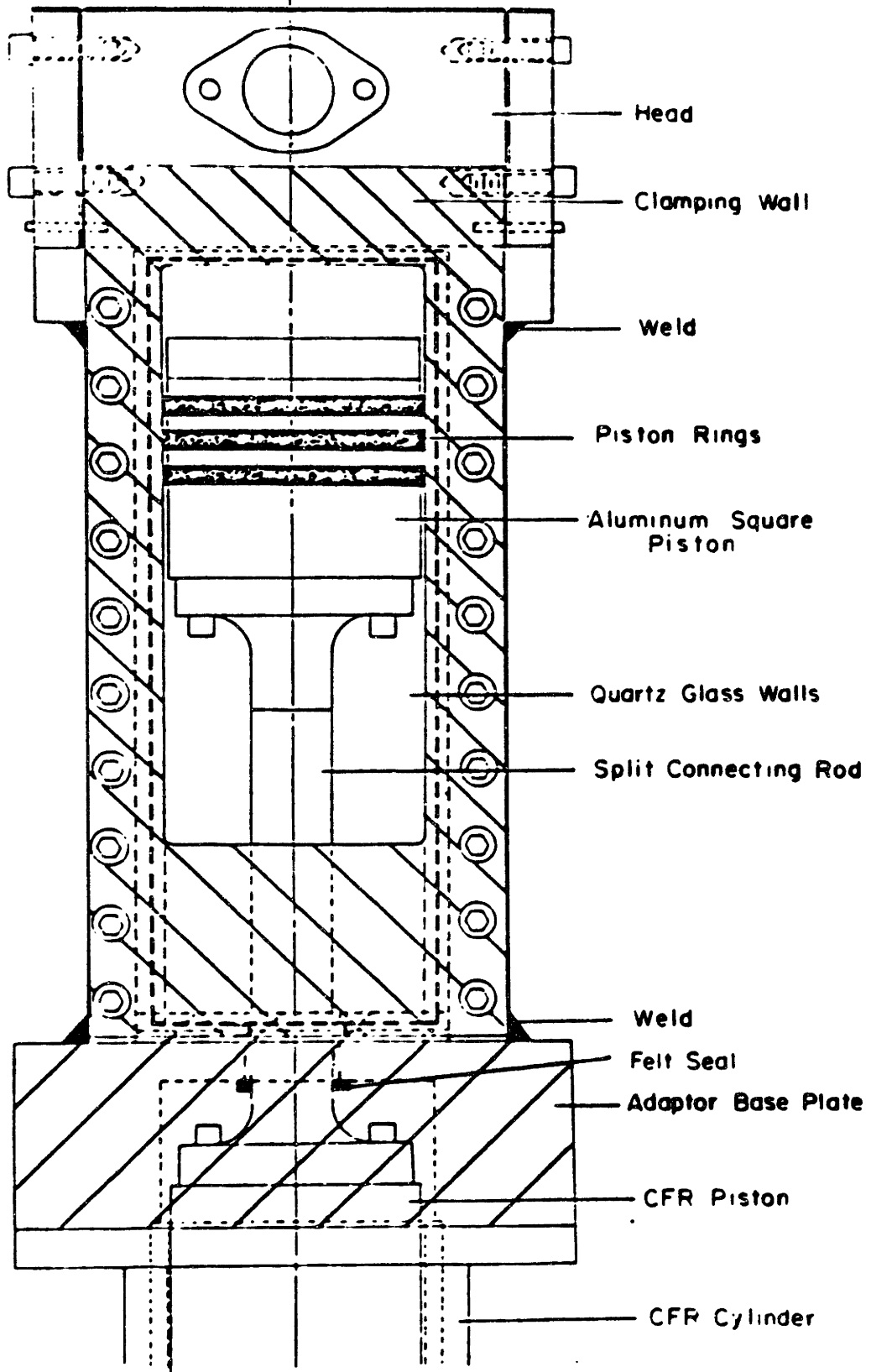
CFR Cylinder

Fig 2.2 - Detail of the engine head and square cylinder assembly
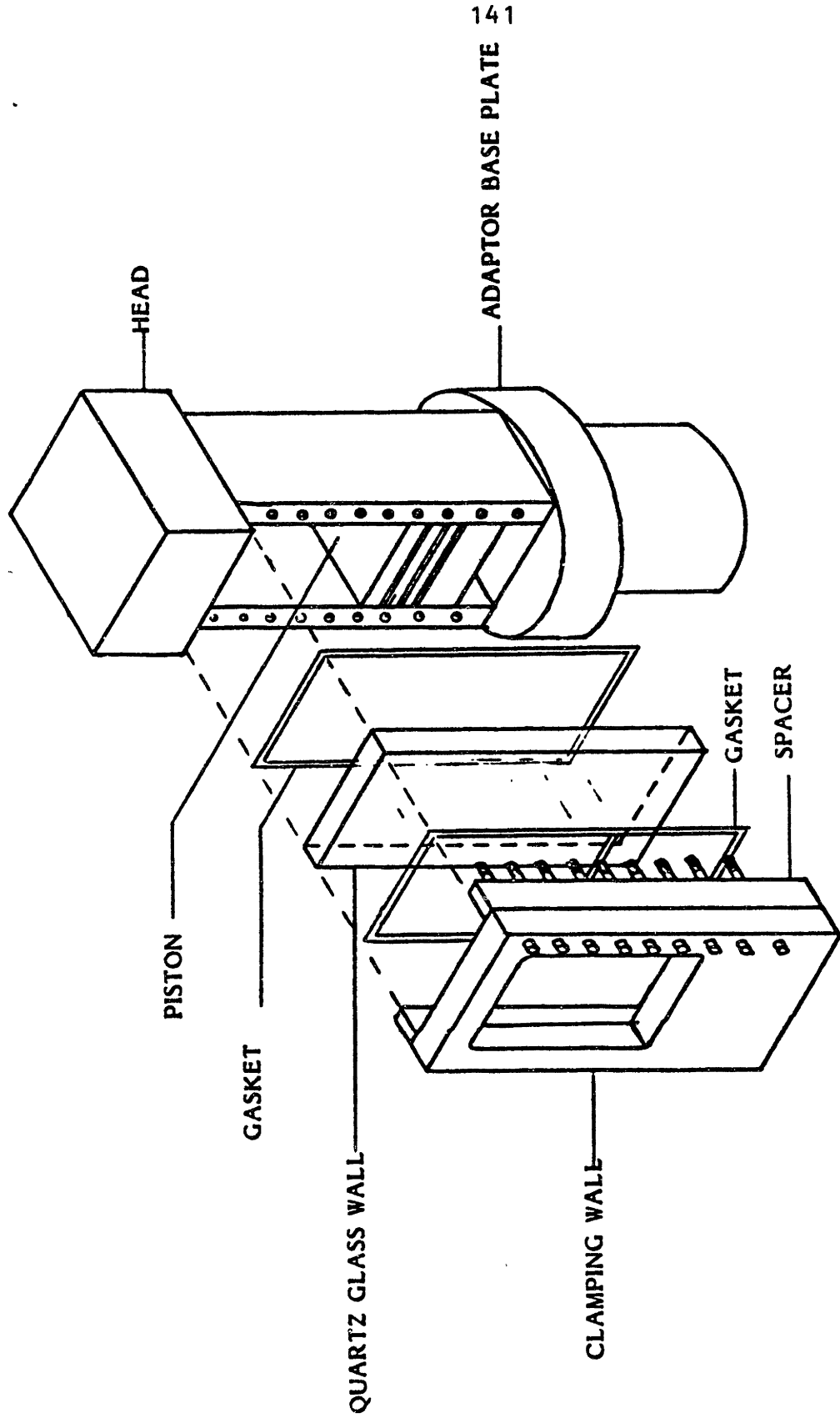
RECTANGULAR CROSS-SECTION

Fig 2.3 – Clamping and sealing arrangement of the quartz windows
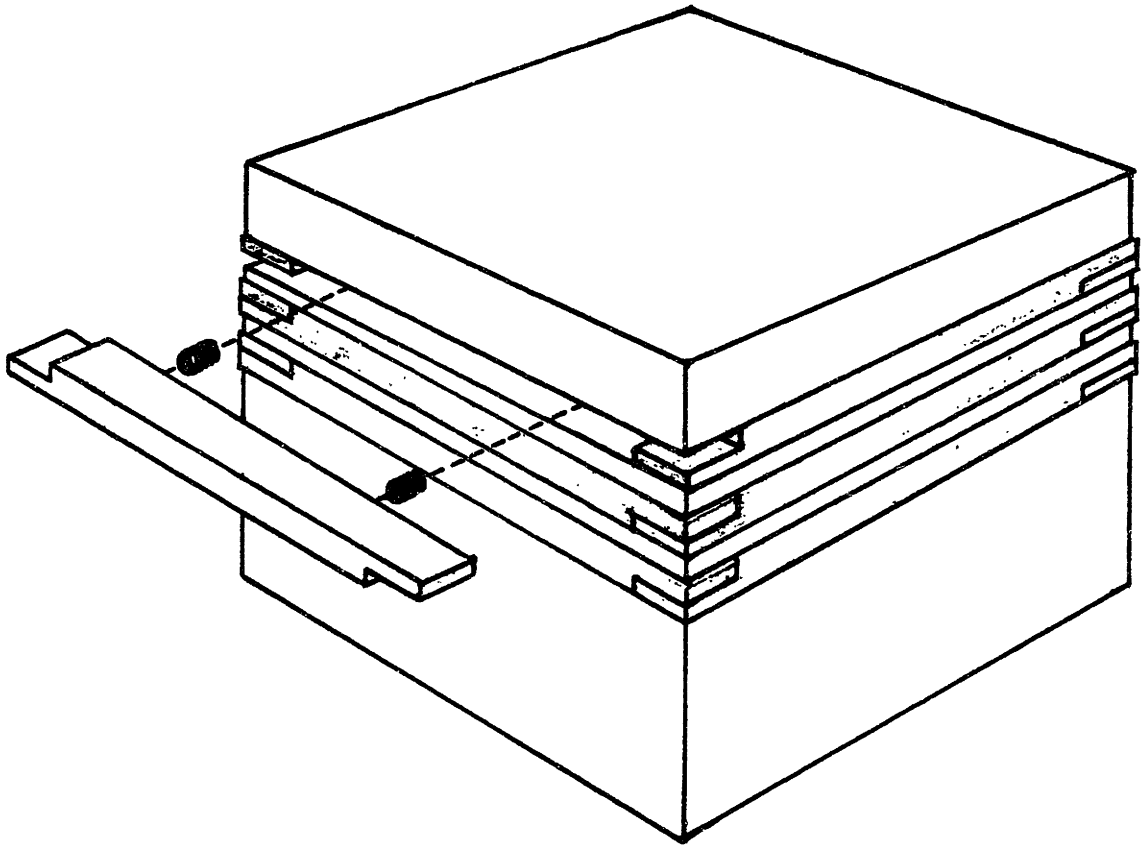
Fig 2.4 – Square piston "ring" assembly. The "rings" overlap at the corners and are pressed against the walls by coil springs

143
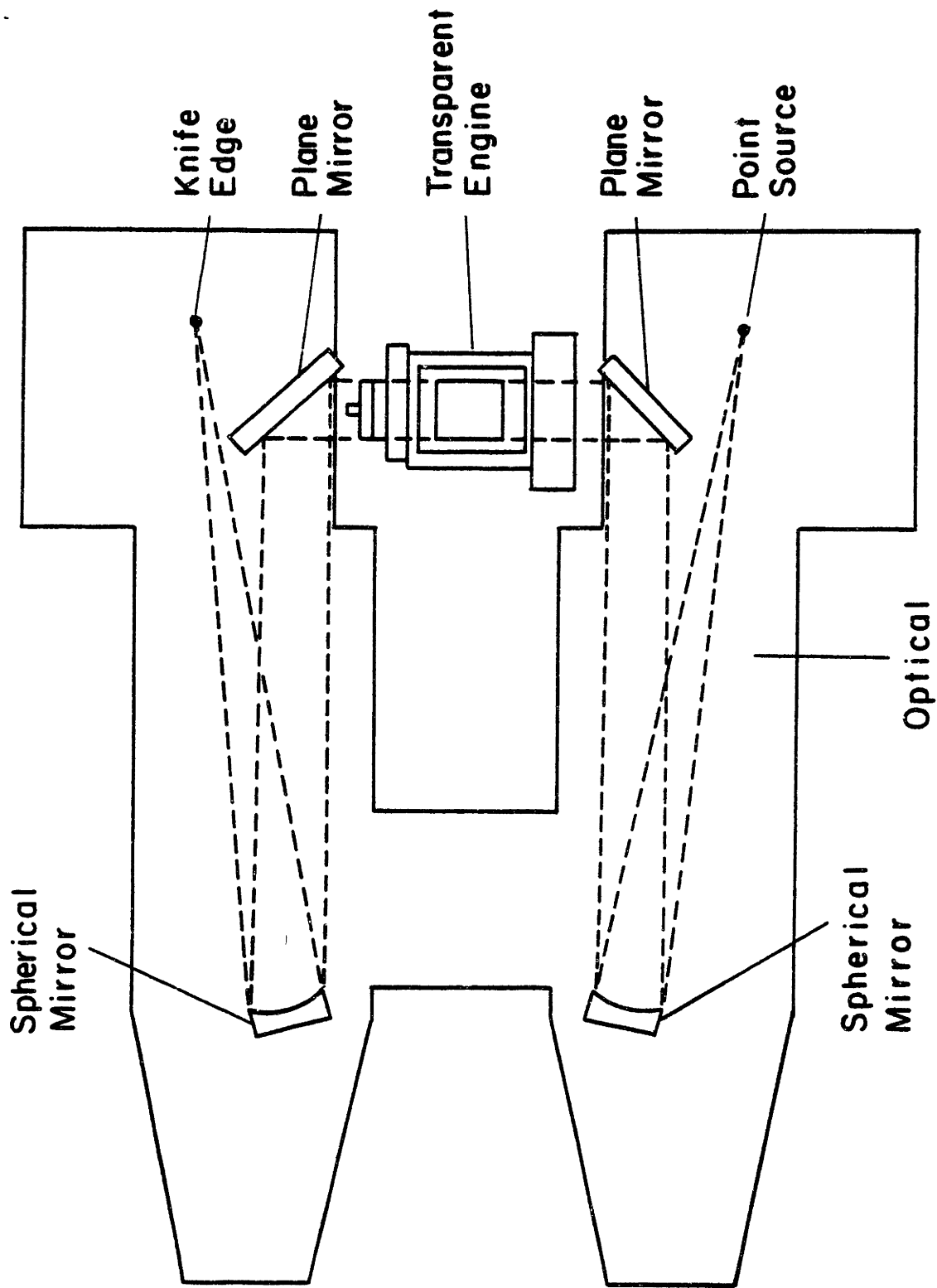
Fig 2.5 – Top view of the Schlieren set up
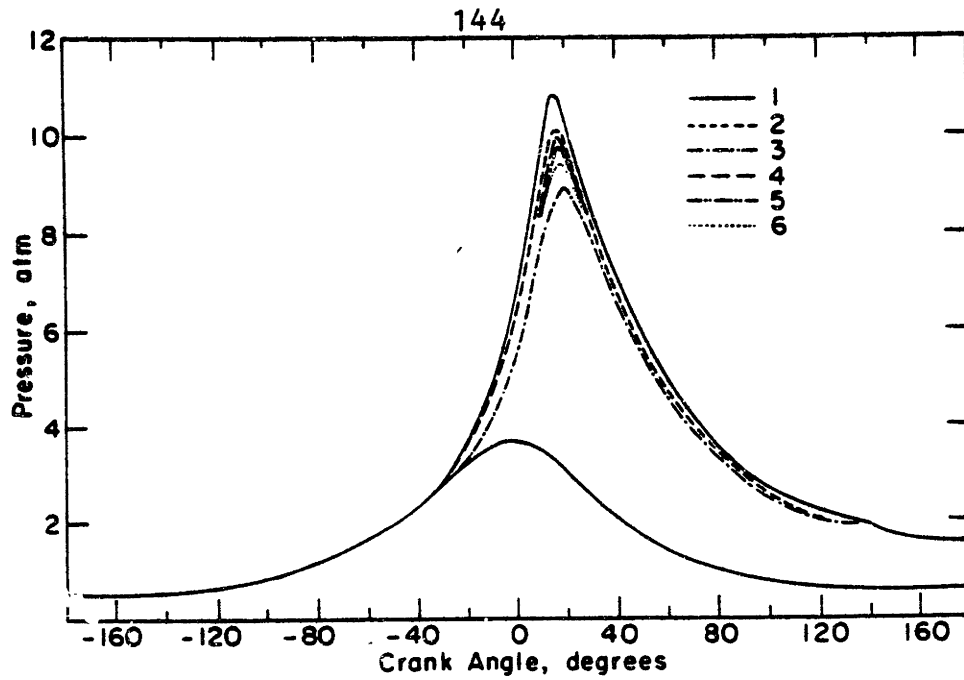
Fig 2.6a – Pressure traces of a motoring and six consecutive firing cycles
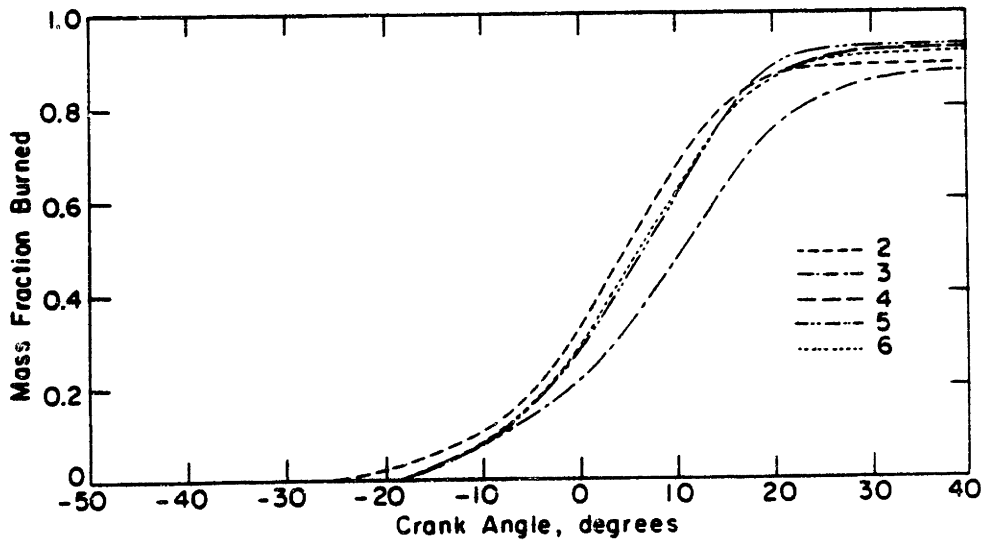
Fig 2.6b – The calculated mass fraction burned profiles corresponding to fig 2.6a. The traces become closer together as the engine stabilizes
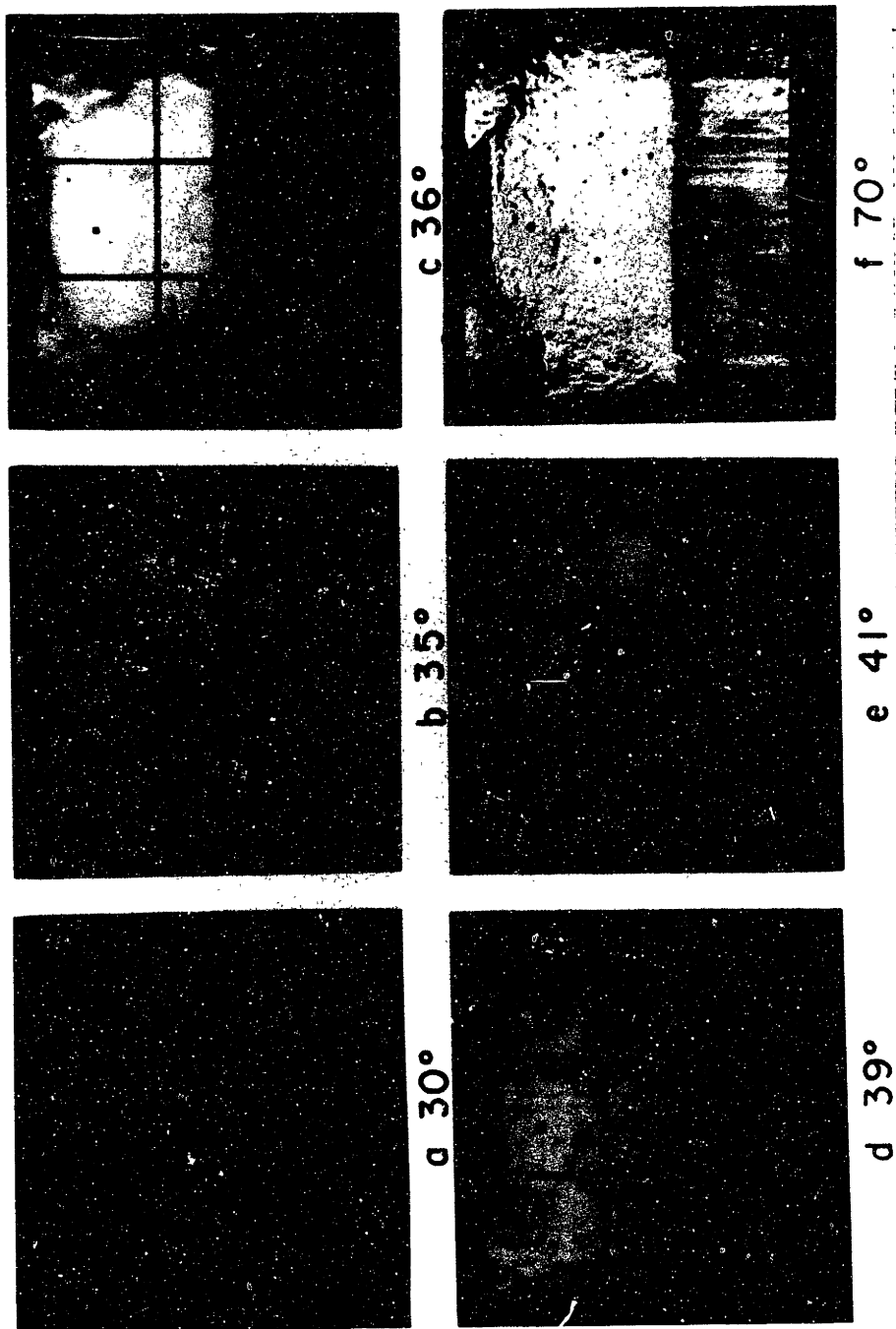
Fig 3.1 – Six still pictures of the intake process showing the different stages of development of the intake jet. The flow of the trapped gas out of the right crevice is observed in pictures a, b, c, d, and e, while the flow out of the left crevice in picture a. The numbers are the crank angle degrees ATC at which the picture was taken. The vertical and horizontal lines in b, c, d, and e are the reference wires placed on one side of the engine.

THIS PAGE WAS INTENTIONALLY
LEFT BLANK
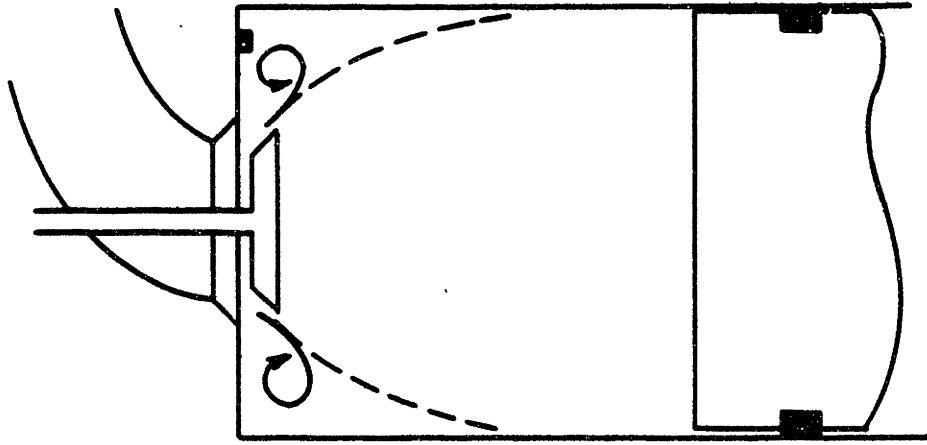
Fig 3.3 – Schematic of the corner vortices generated by the intake flow. The dashed line represents the downward flow of the bulk gas.
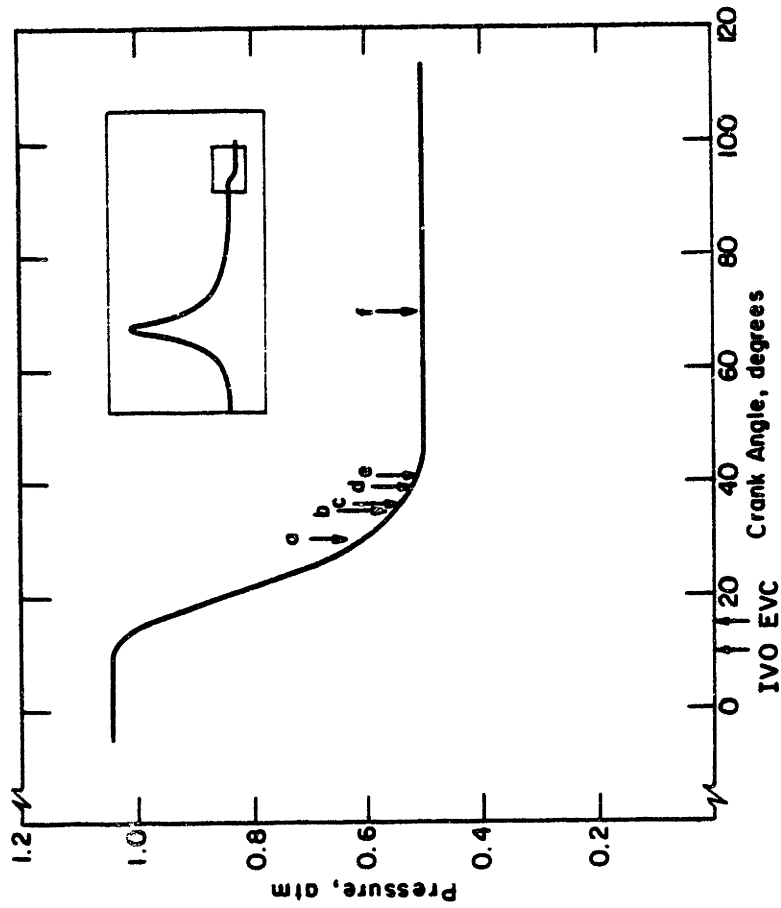
Fig 3.2 – Pressure during intake valve opening. The arrows indicate the timing of the pictures of Fig 3.1.
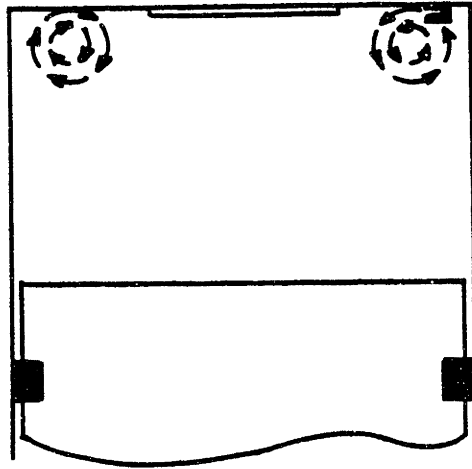
Fig 3.4 – Representation of the top corner vortices observed during compression in motoring cycles.
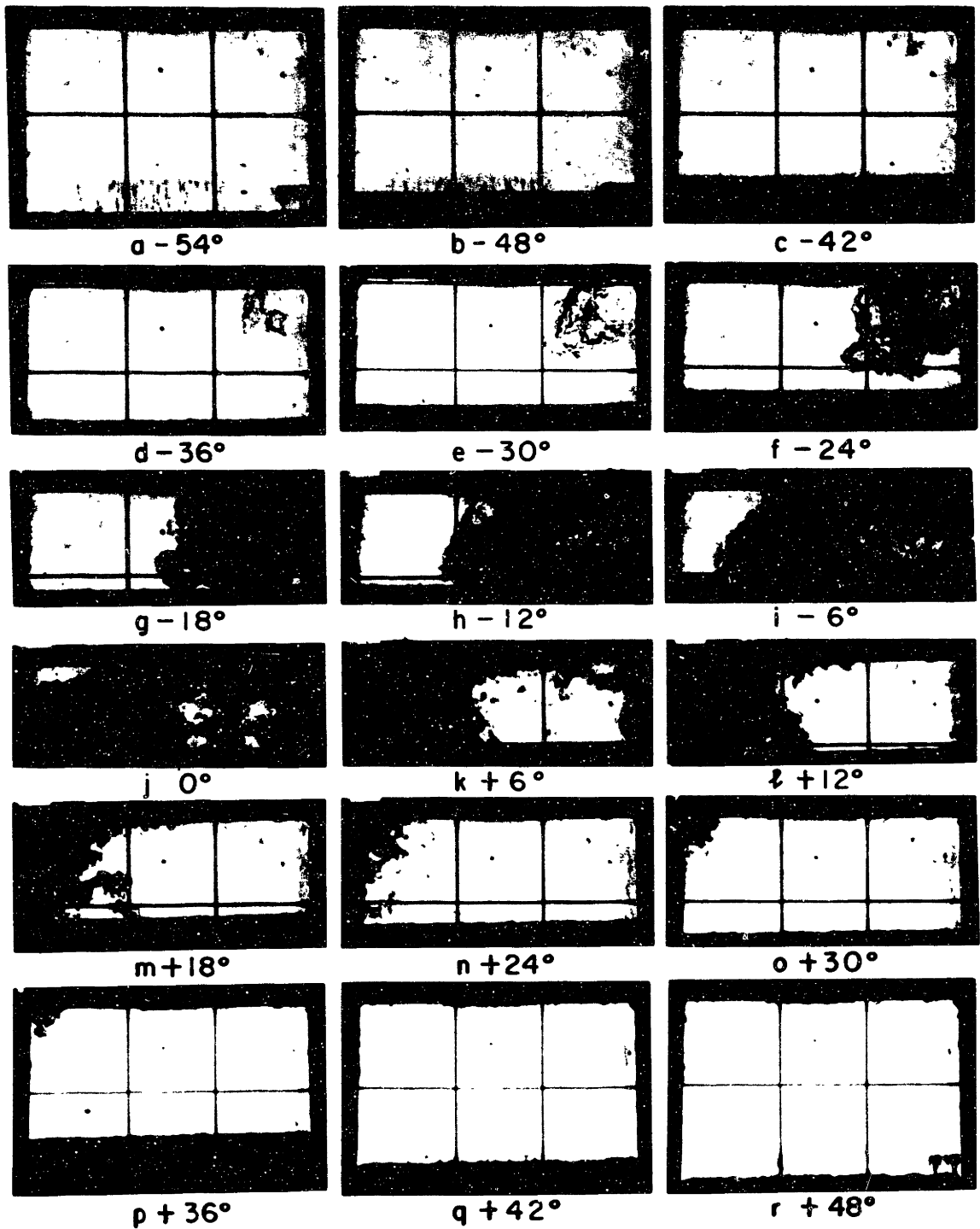
Fig 3.5 – Photographs of a typical combustion process reproduced from a movie with intervals of 6 degrees (0.72 ms). Spark timing is 55° BTC.

THIS PAGE WAS INTENTIONALLY
LEFT BLANK

Fig 3.6 – Interpretation of the Schlieren photographs showing the three distinct zones present during combustion
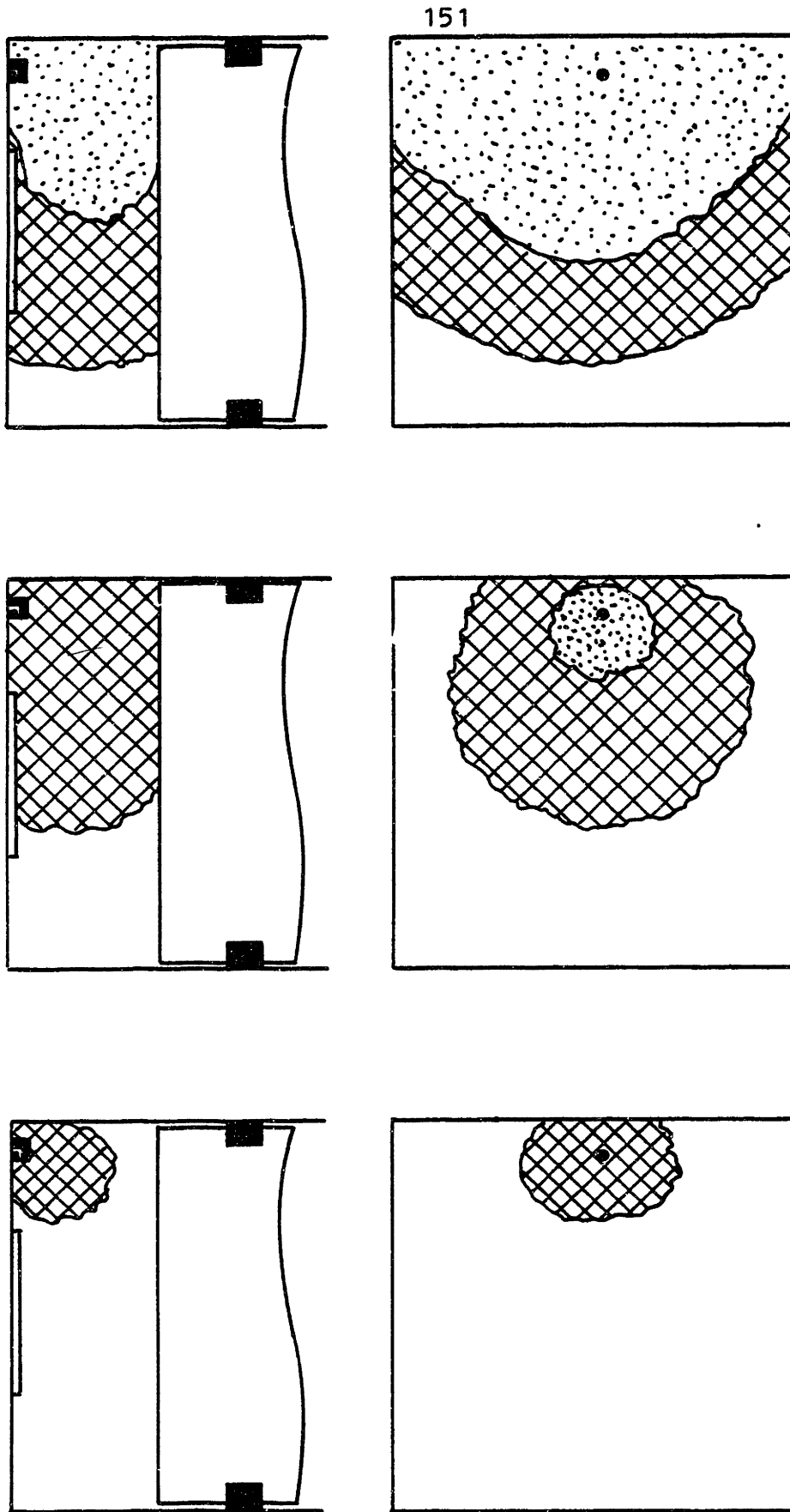
☐ Unburned Zone   ⊠ Flame Zone   ▨ Burned Zone

This page is intentionally left blank.
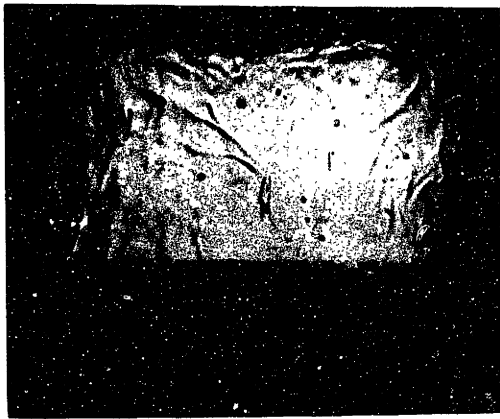
(a) 45° ATC
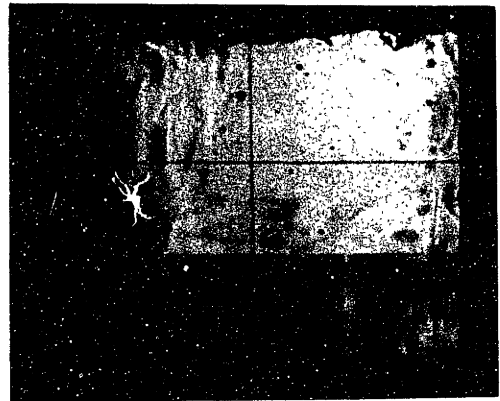
(b) 65° ATC
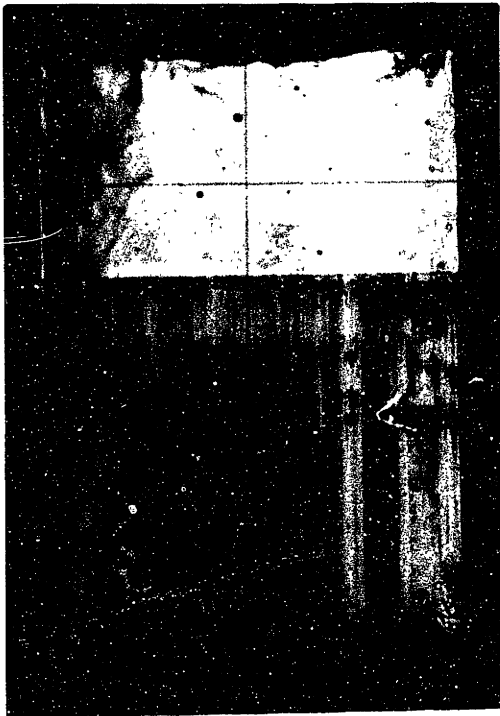
(c) 120° ATC
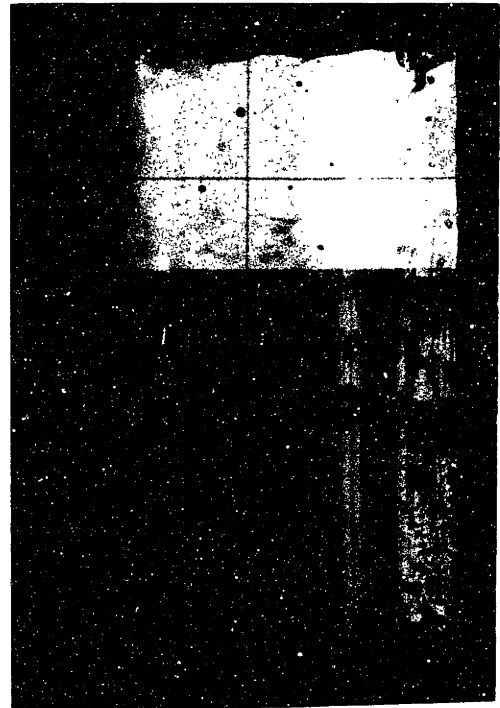
(d) 140° ATC

Fig. 3.7 - Expansion of gas out of crevices: flow out of spark plug crevice is visible in right hand side top corner of all pictures as dark streaks and the flow out of the crevices formed by piston, cylinder and rings is seen in pictures (c) as jets from piston crown corners which spread on the walls (d)

THIS PAGE WAS INTENTIONALLY
LEFT BLANK
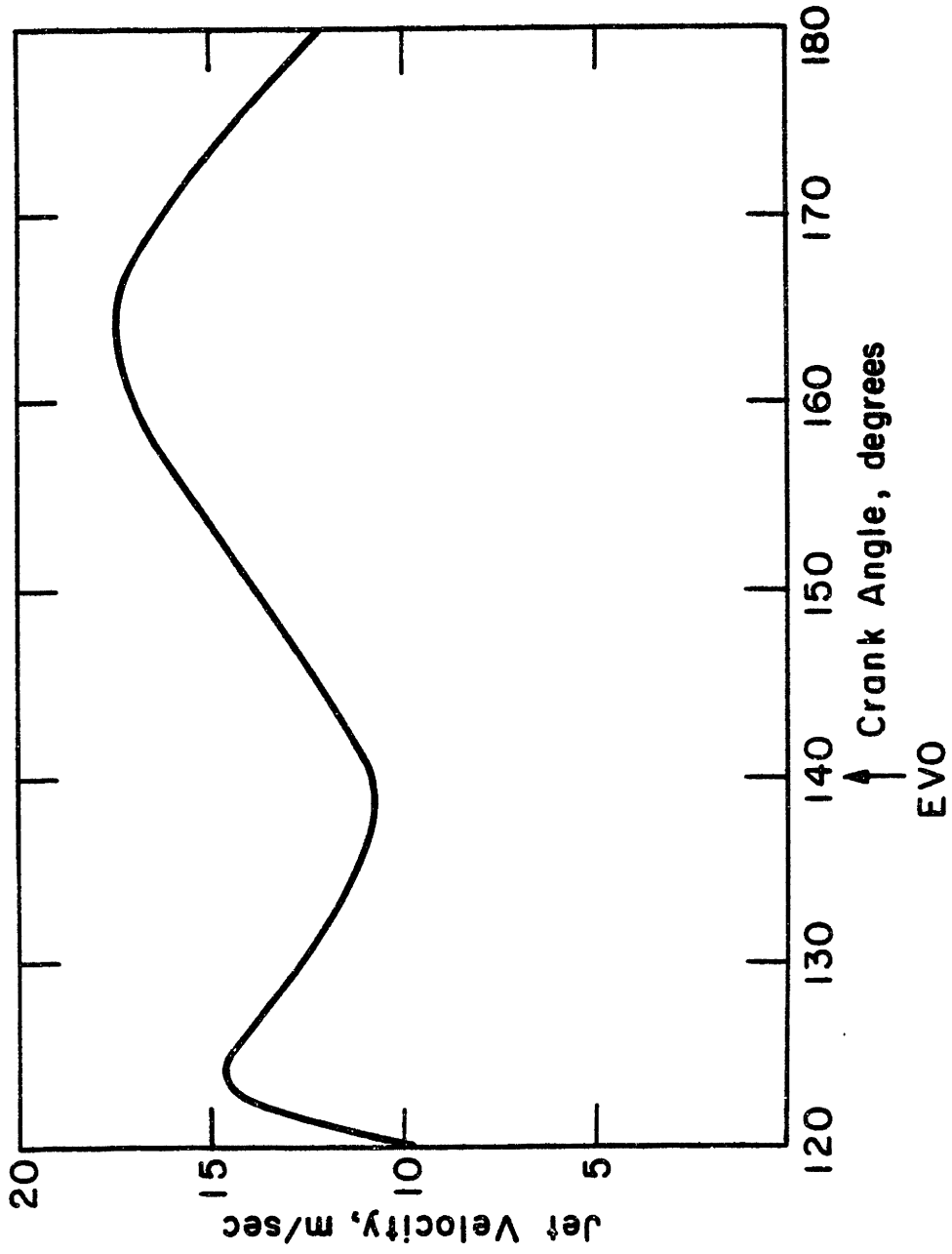
Fig 3.8 -- The crevice flow jet velocity, normal to the jet front, versus crank angle.
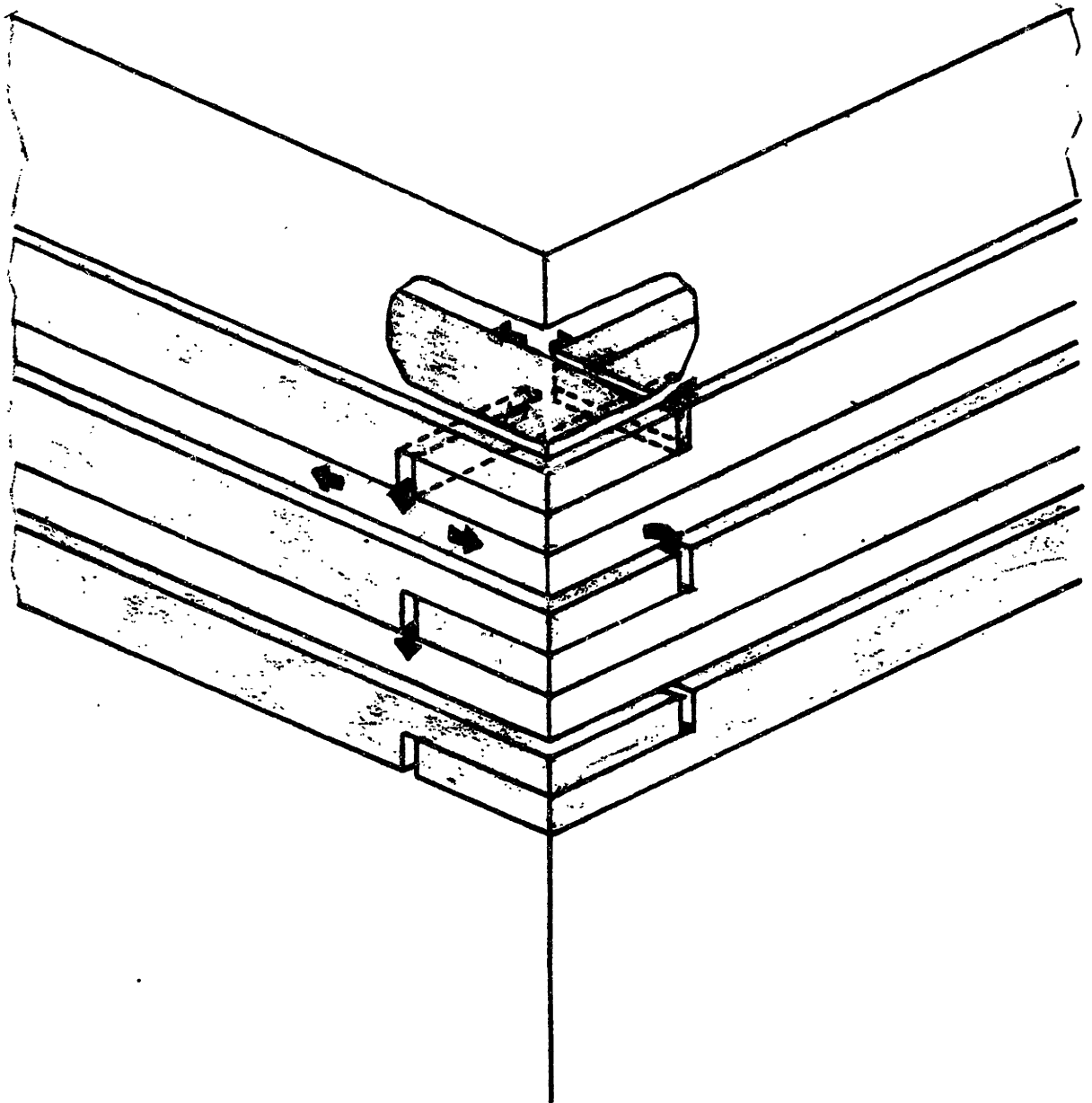
Fig 3.9 – Piston ring assembly showing the passages through which the gas flows in and out of the regions behind and between the rings.
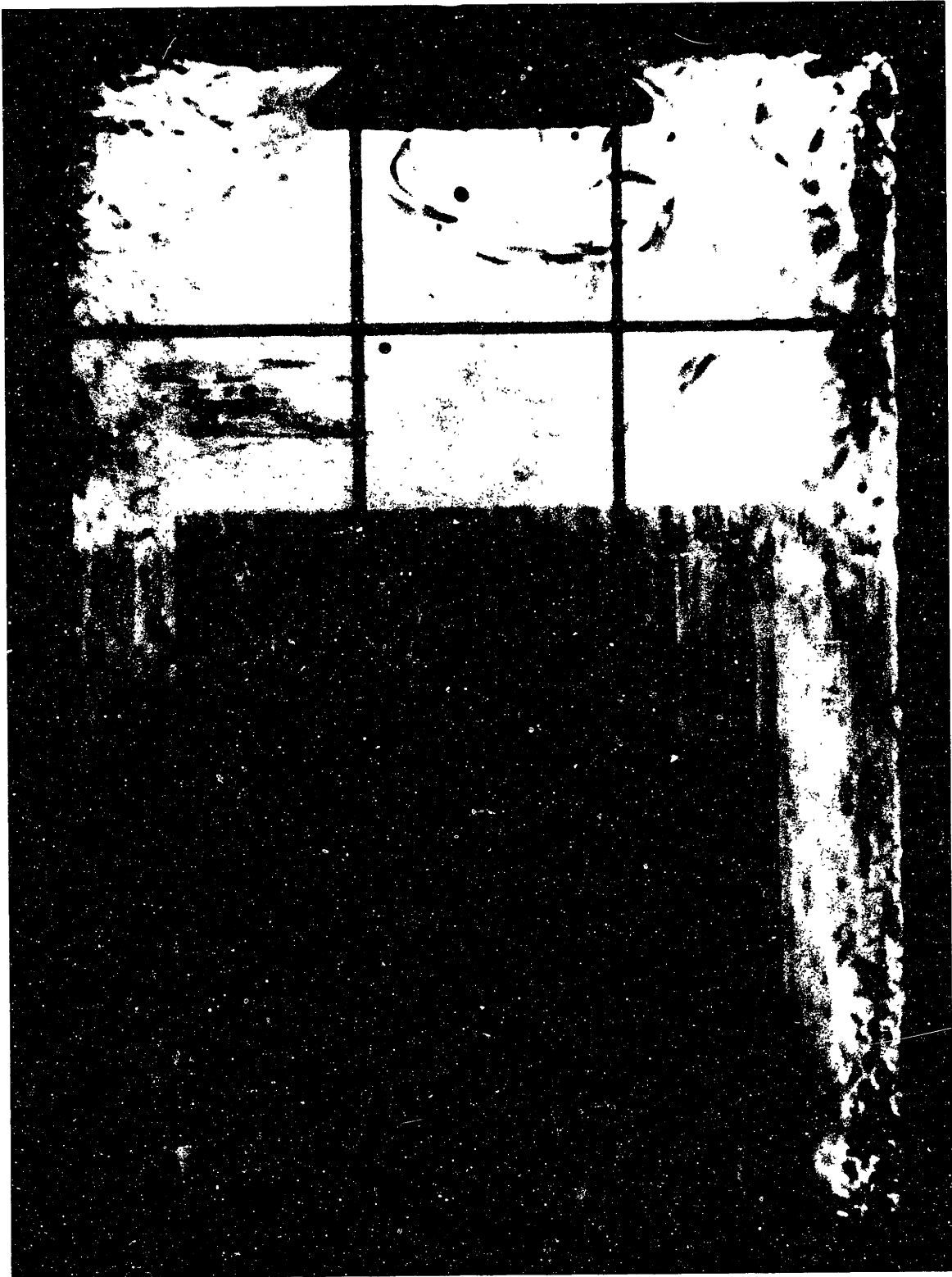
Fig 3.10 – Picture taken 120° BTC during the exhaust stroke showing a portion of the crevice jet flow, circulating under the exhaust valve. Also the left hand side piston crown cylinder wall vortex is present while the right hand side vortex has not yet formed.

THIS PAGE WAS INTENTIONALLY
LEFT BLANK
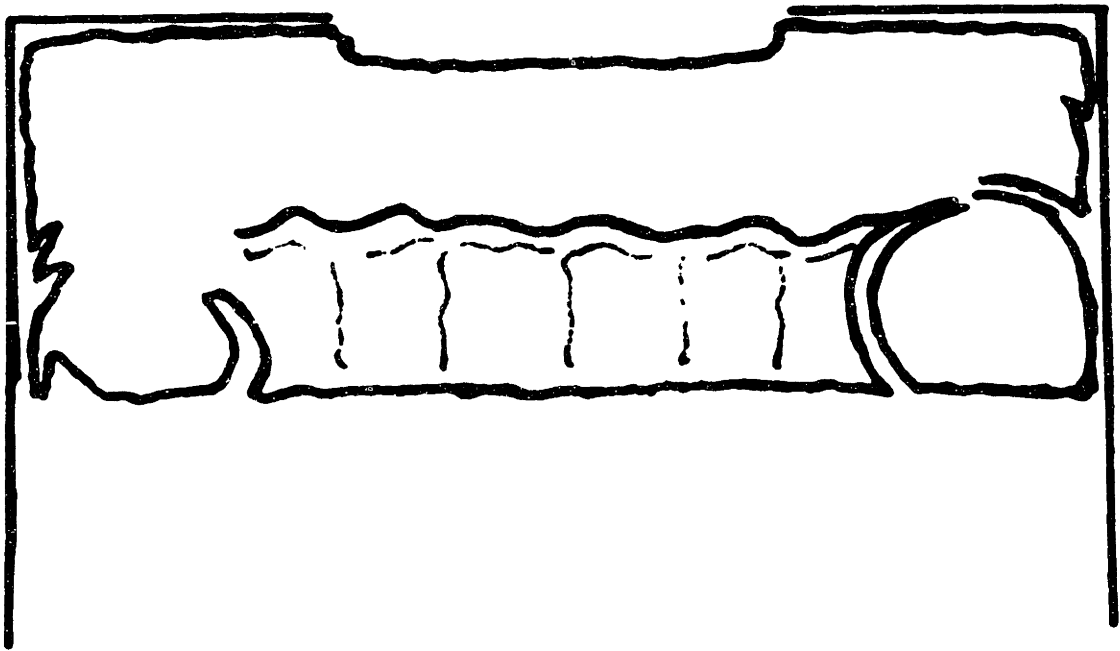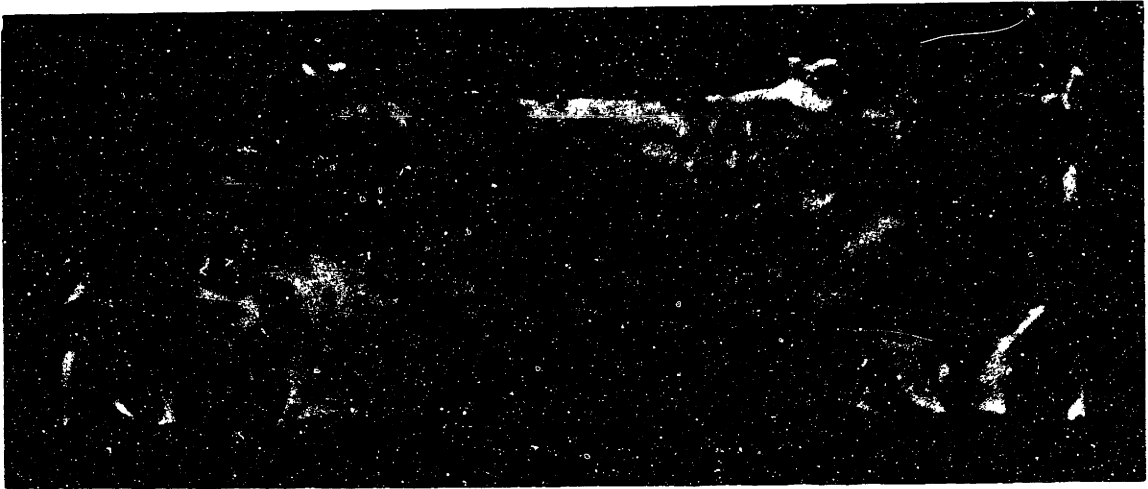
Fig 3.11 – Picture taken 20° BTC and interpretation showing the piston-crown cylinder corner vortices on all sides, left, right, and on the windows. Entrainment of boundary layer on the walls is observable as dark streaks.
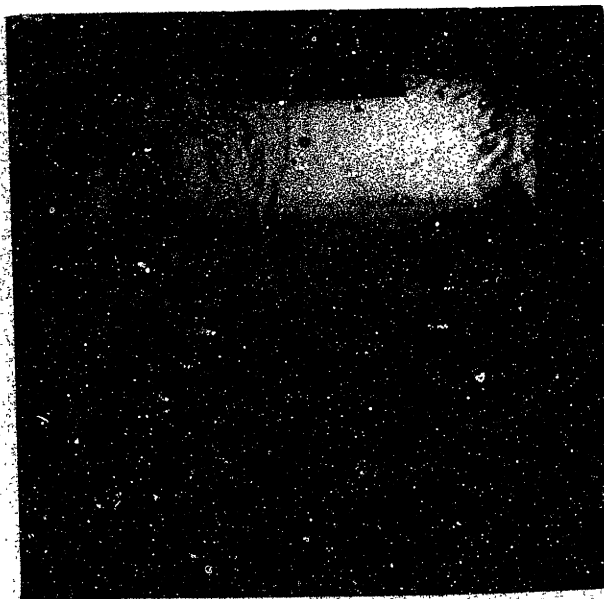
Fig. 3.12 - Picture taken 60° BTC on exhaust
stroke showing vortex instability, the left-
hand-side vortex is broken up while the
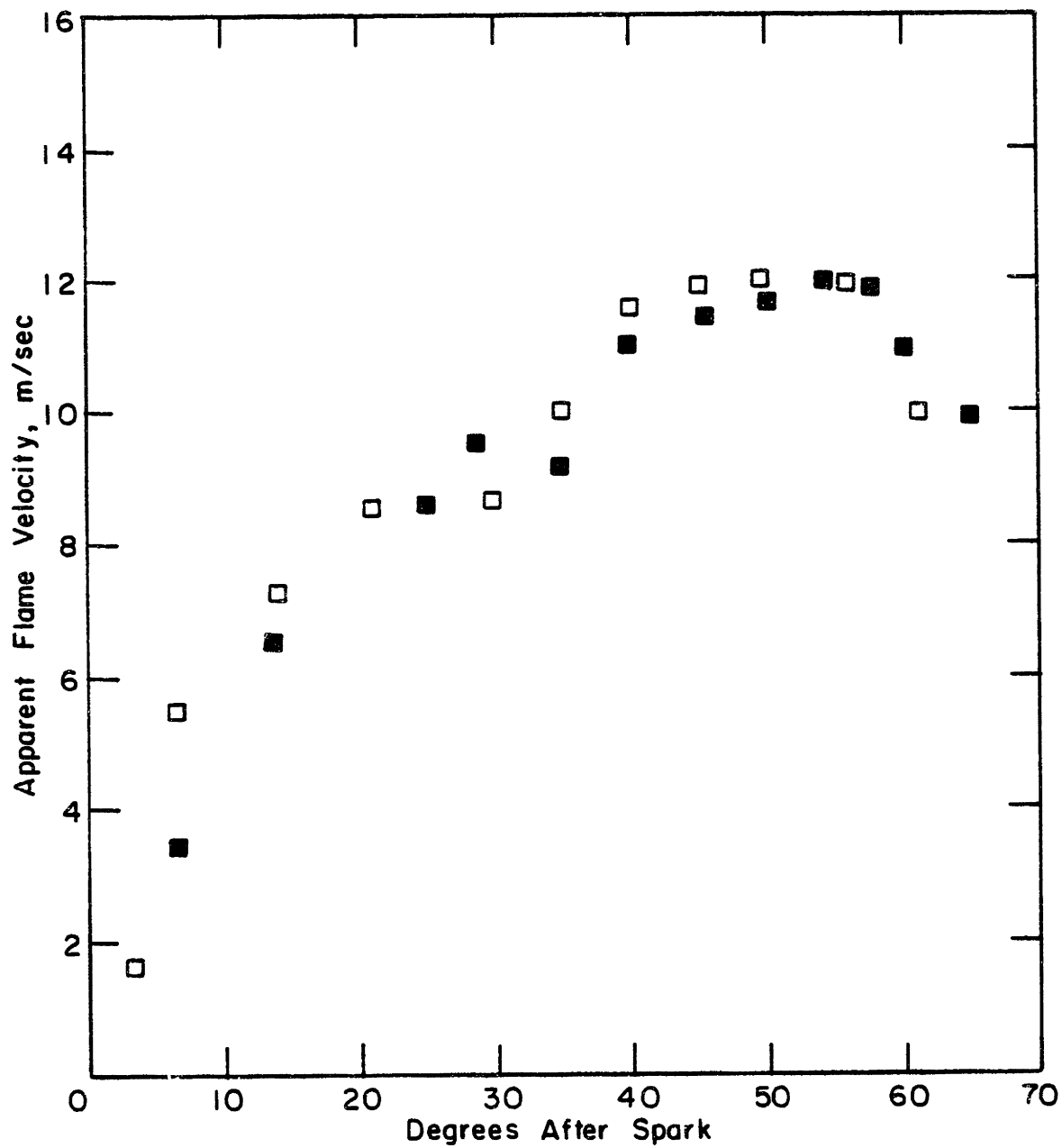right-hand-side vortex is still growing

Fig 4.1 – Apparent flame velocity, average rate of flame travel normal to the flame front in the lab coordinates for two consecutive cycles.
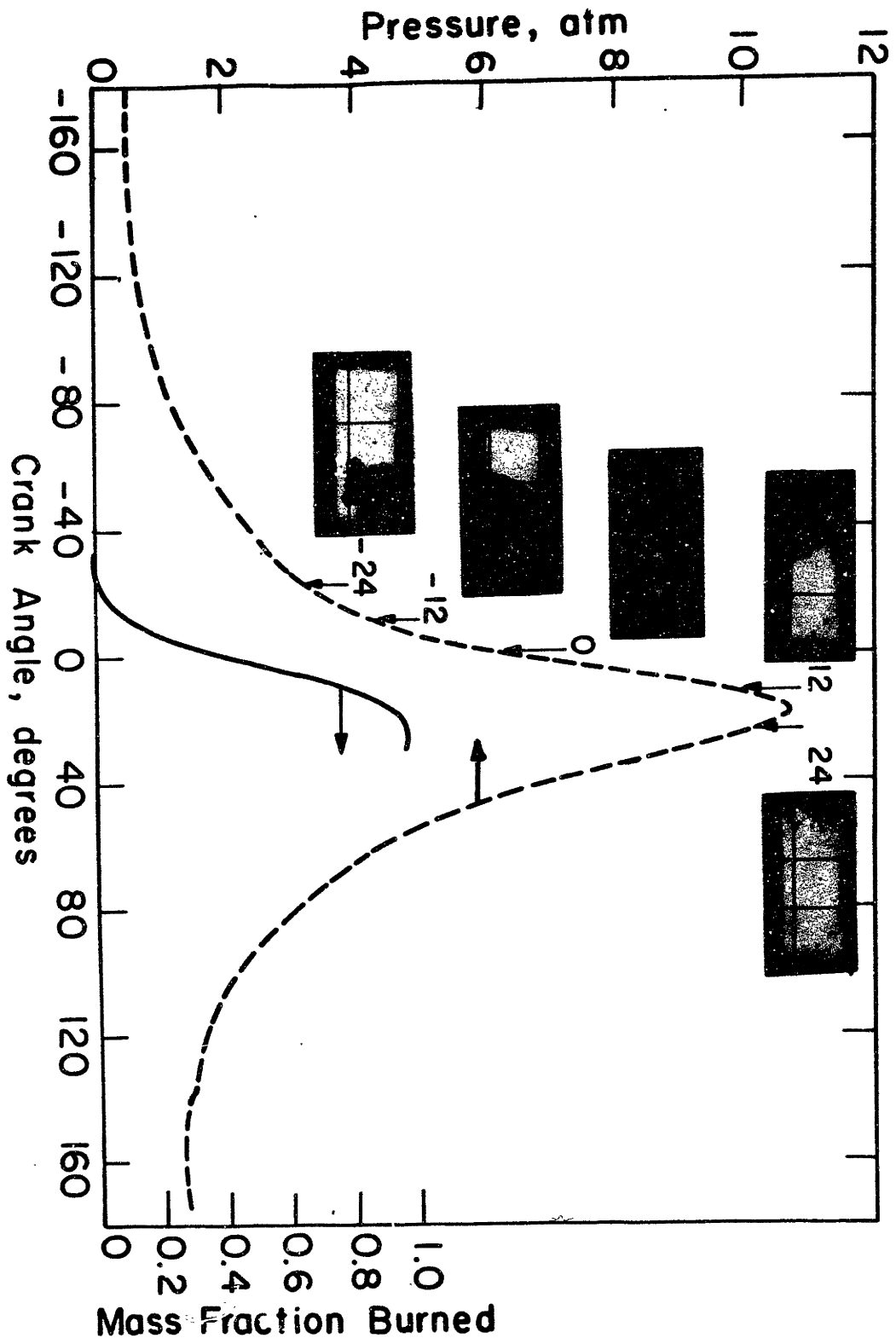
This page is intentionally left blank.

Fig 4.2 - Pressure and mass fraction burned curves corresponding to Fig. 3.5. Five stages of the flame development of Fig. 3.5 are represented.
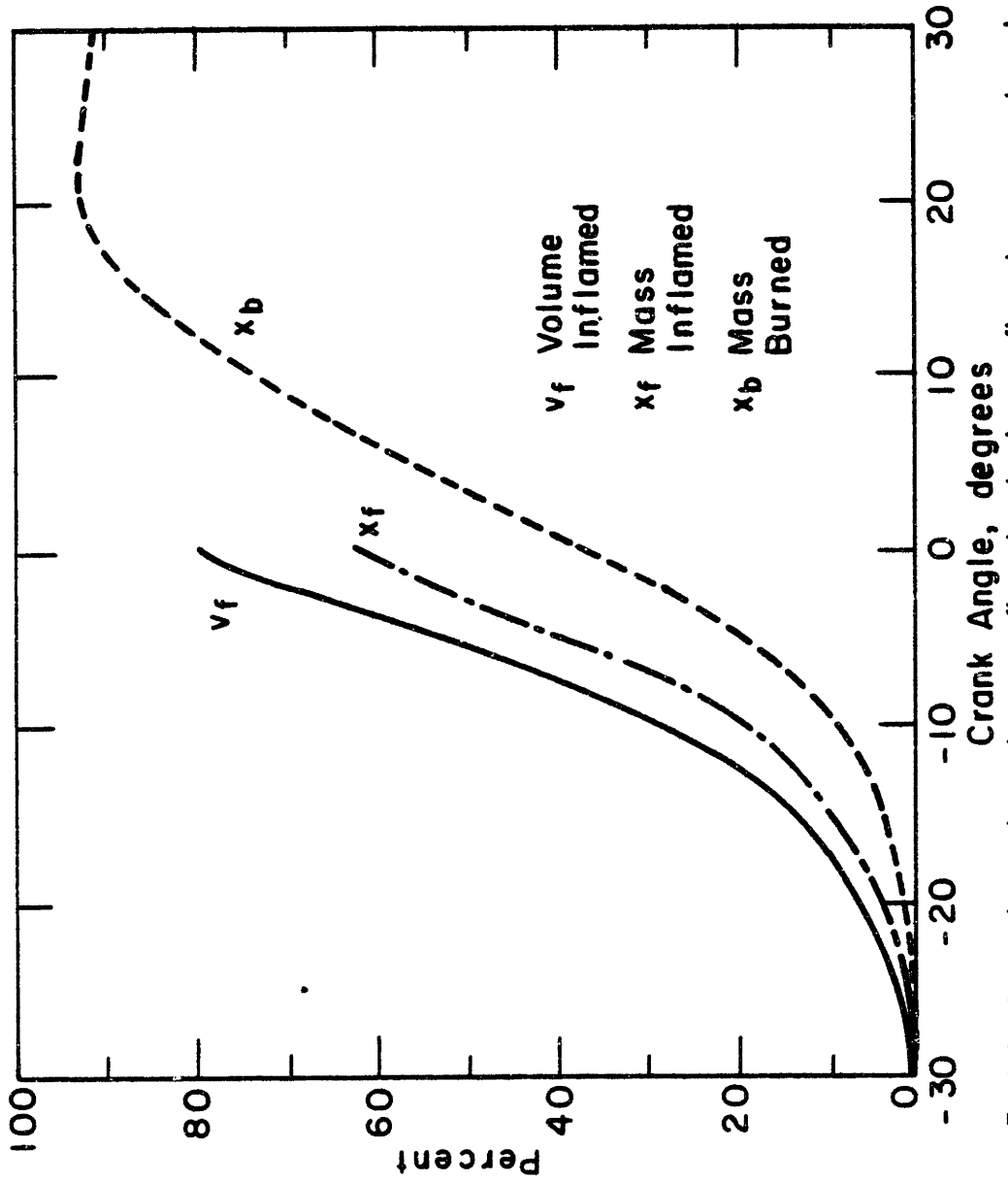
Fig 4.3 – Percent mass burned, mass enflamed and volume enflamed versus crank angle corresponding to Fig 3.5.

This page is intentionally left blank.

Fig 4.4 – A low sensitivity Schlieren still picture of the combustion process showing the structure of the flame, especially the start of the actual burning zone.

Fig 4.5 – A still picture of the flame after the front has reached the left side of the combustion chamber, showing the structure of the back side of the flame. The scale is the same as Fig 4.4.

a reference   b .0°   c .0°   d 0.5°

e 0.8°   f 1.0°   g 1.2°   h 1.5°

i 2°   j 2.5°   k 3.5°   l 5.0°

m 6.0°   n 7.0°   o 8.0°   p 10.0°

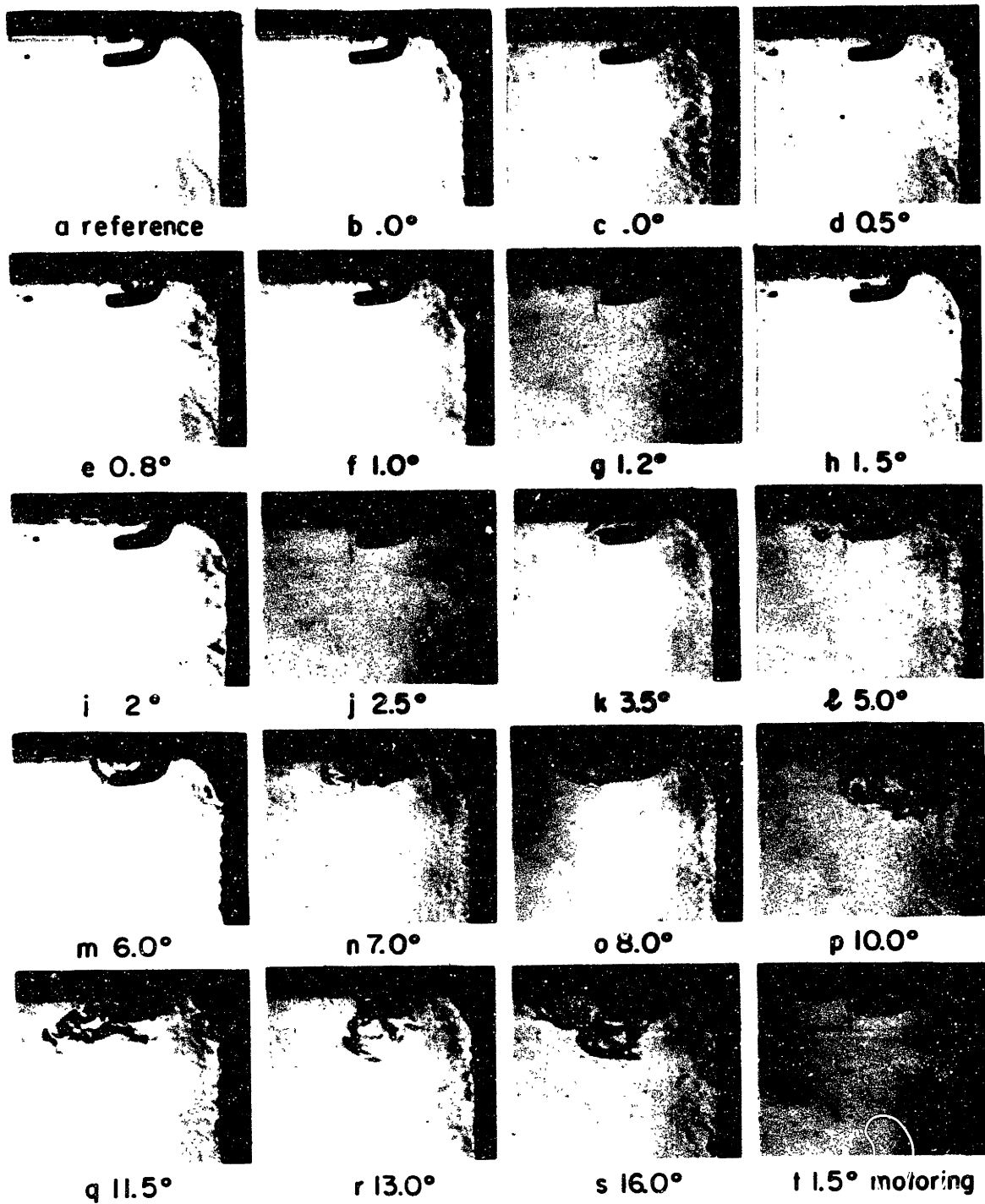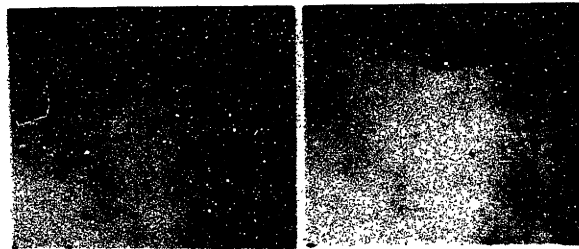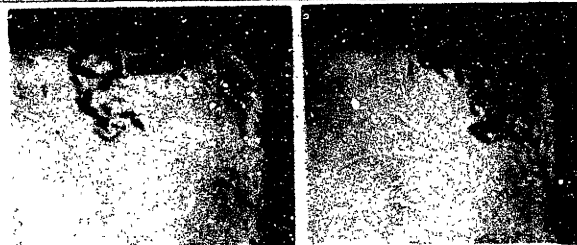q 11.5°   r 13.0°   s 16.0°   t 1.5° motoring

Fig 4.6 – Still pictures of different cycles showing the spark discharge (b and c), spark with flame kernel, (d to h) and growth of the flame (j to s) around the spark plug. The numbers indicate the timing of the pictures in degrees after the spark, which occurs at 55° BTC.
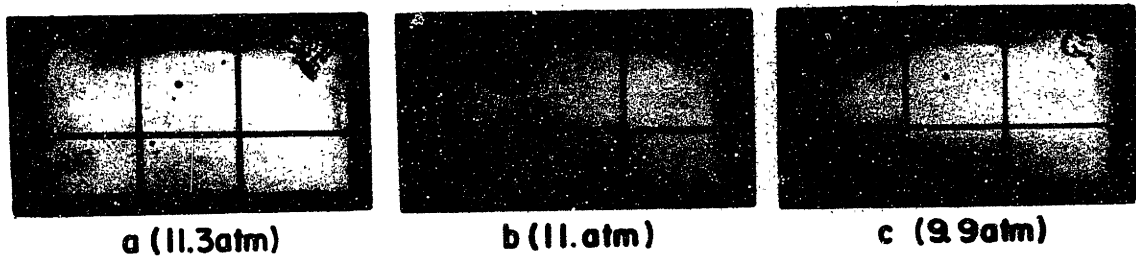
a (9.2atm)   b (9.9atm)

Fig 4.7 – Kernel development in two cycles at 9.5° after the spark.

a (9.5atm)   b (9.2 atm)

Fig 4.8 – Still pictures taken 12° after spark in two cycles, showing flame moving to right or left. The numbers are peak pressure of the corresponding cycles in atm.
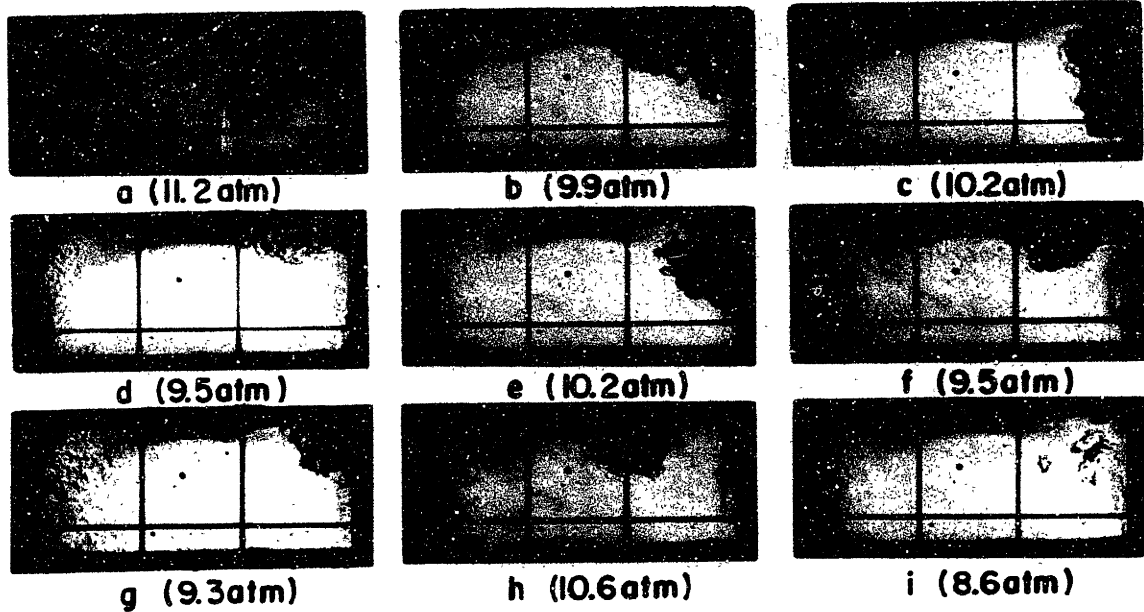
a (11.3atm) b (11.atm) c (9.9atm)

Fig 4.9 – Photographs taken at 14° after the spark of three cycles.

a (11.2atm) b (9.9atm) c (10.2atm)

d (9.5atm) e (10.2atm) f (9.5atm)

g (9.3atm) h (10.6atm) i (8.6atm)

Fig 4.10 – Still pictures taken 31° after spark (i.e. 24° BTC) from nine different cycles showing the variation in size, shape and the location of the flame from cycle to cycle. The detachment of the flame from the spark plug in h and i is due to the rotational motion shown in Fig 3.4.
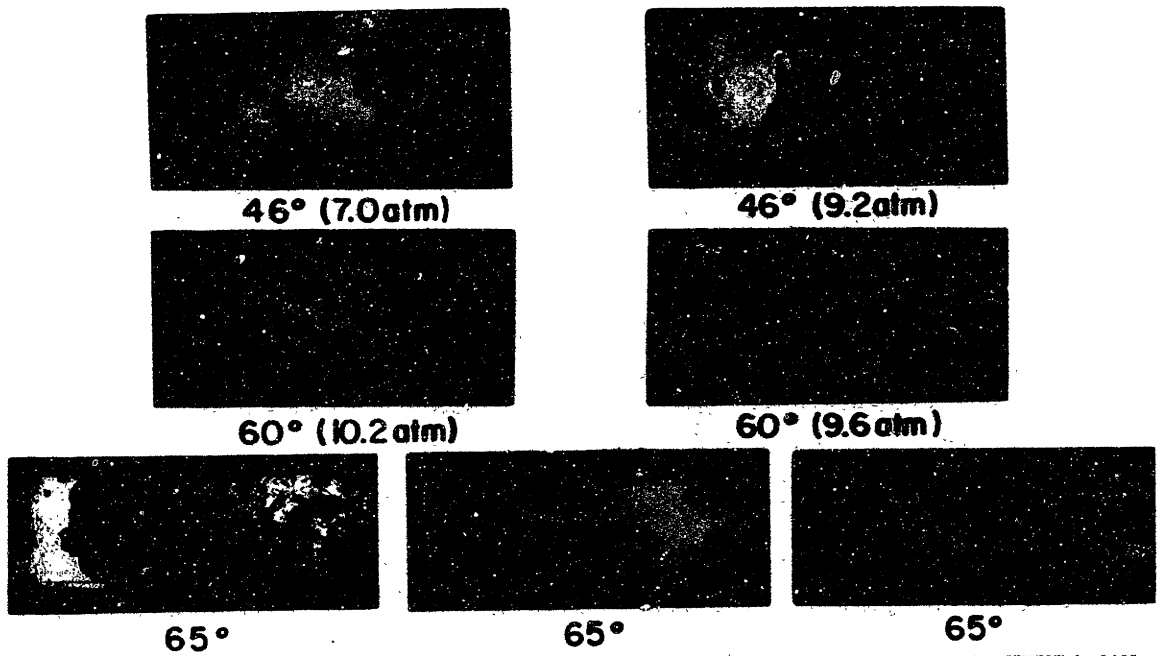
46° (7.0atm)   46° (9.2atm)

60° (10.2atm)   60° (9.6atm)

65°   65°   65°

Fig 4.11 – Three sets of photographs showing the cyclic dispersion when the flame is fully developed. The crank angle degrees shown are timing of the pictures after the spark. The peak pressure of each cycle is given in atm.
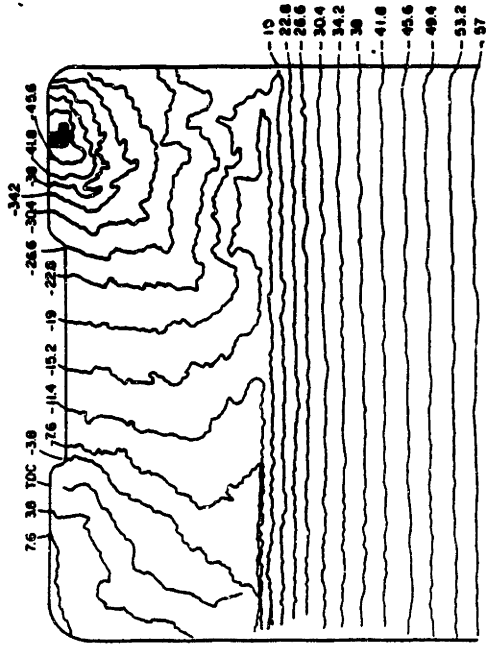
Fig 4.13 — A motoring cycle and the three firing
pressure traces corresponding to Fig 4.12

Fig 4.12 — Tracing from movies of the loading
edge of the flame front at 3.8° (0.456 ms)
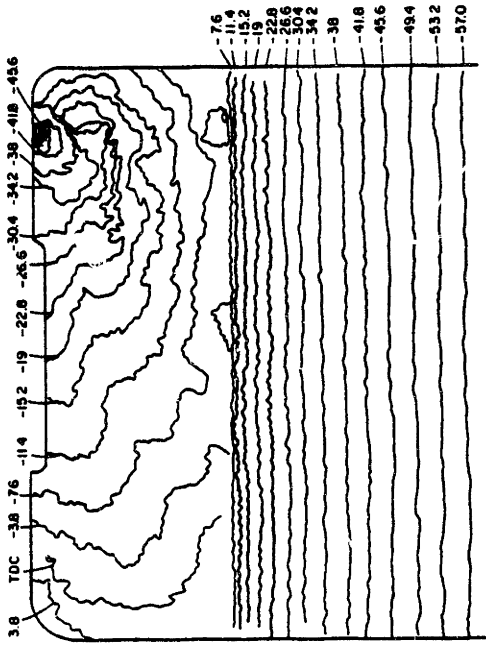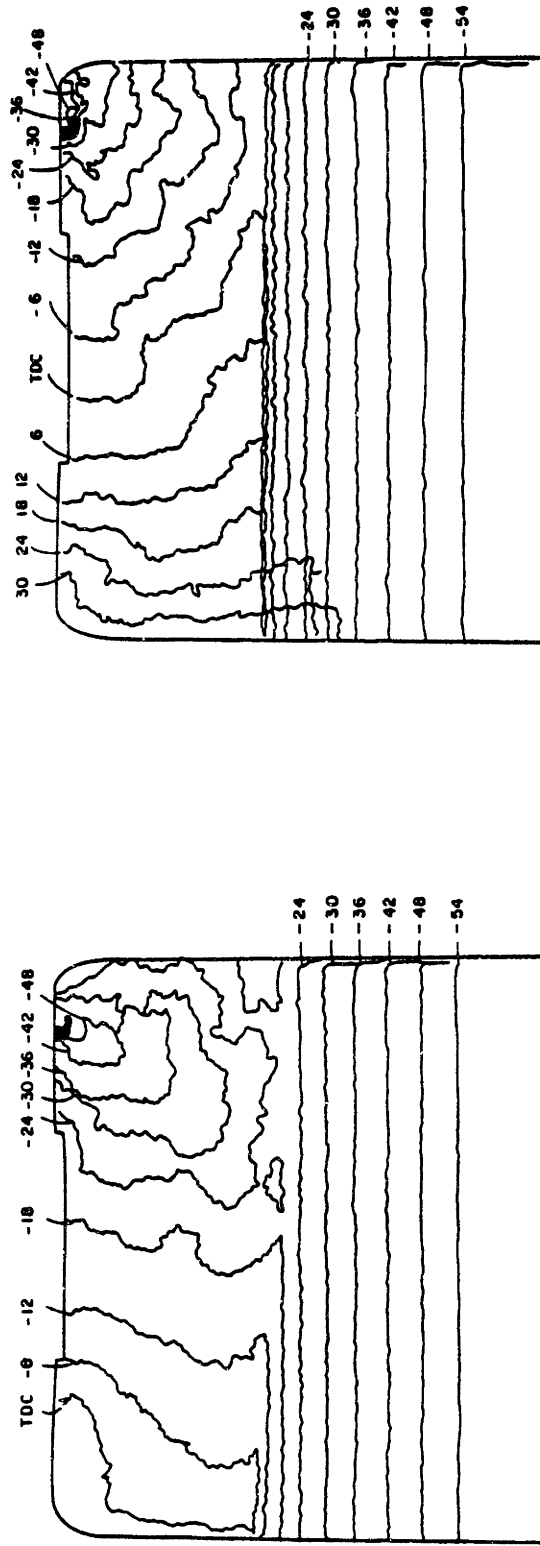intervals for three consecutive cycles

Fig 4.14 – Flame front tracing of a normal cycle (a) and a slow-burning cycle (b). The cycles are consecutive and the tracings are every 6° (0.72 ms) interval.
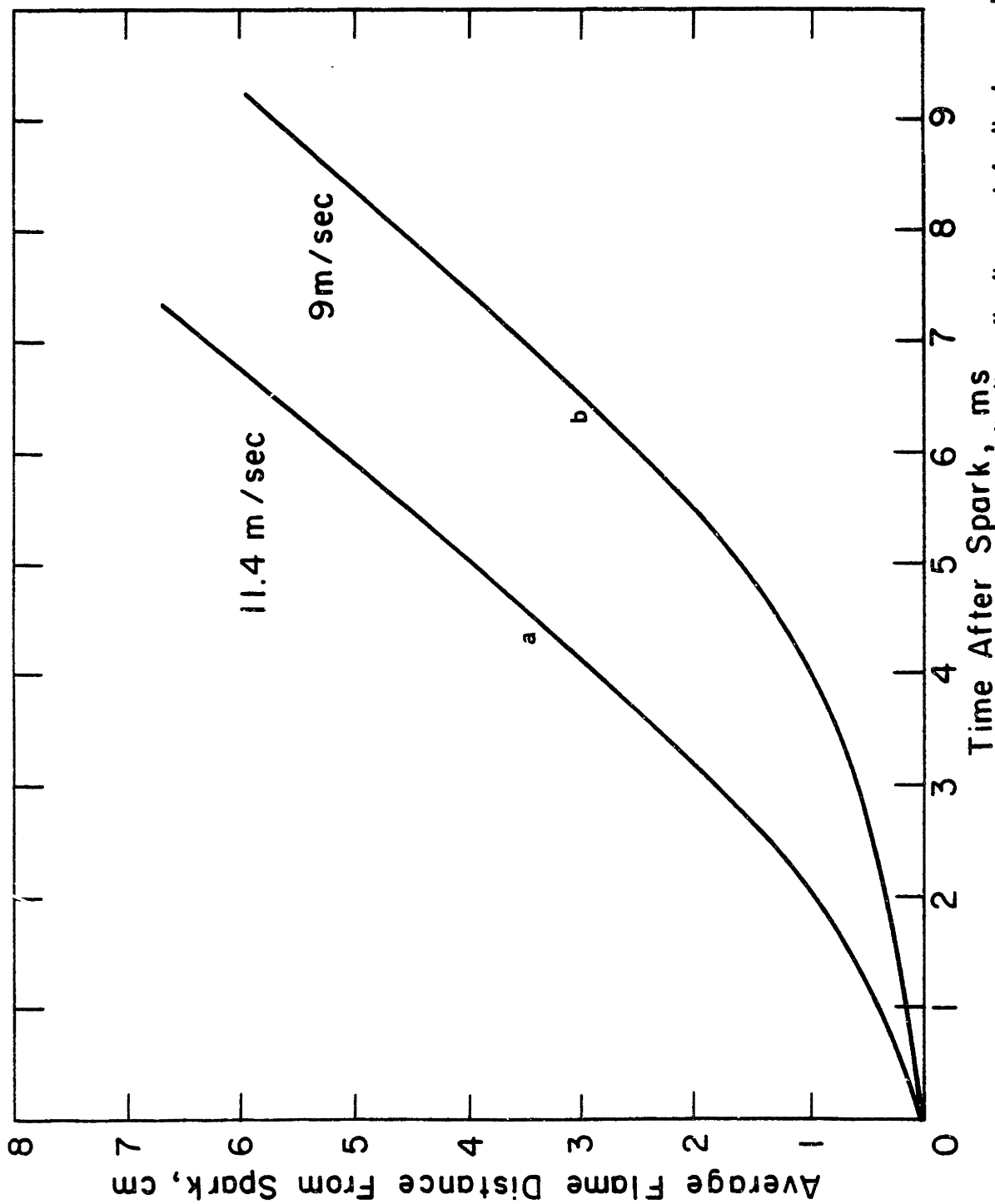
Fig 4.15 – The average flame travel distance normal to the flame front, versus the time after the spark for the two cycles of Fig 4.14

COMBUSTION CHAMBER

REGIONS

1
2
3
4
5
6

plane (a)

TOP LAND CREVICE

plane (b)

(a)

(b)
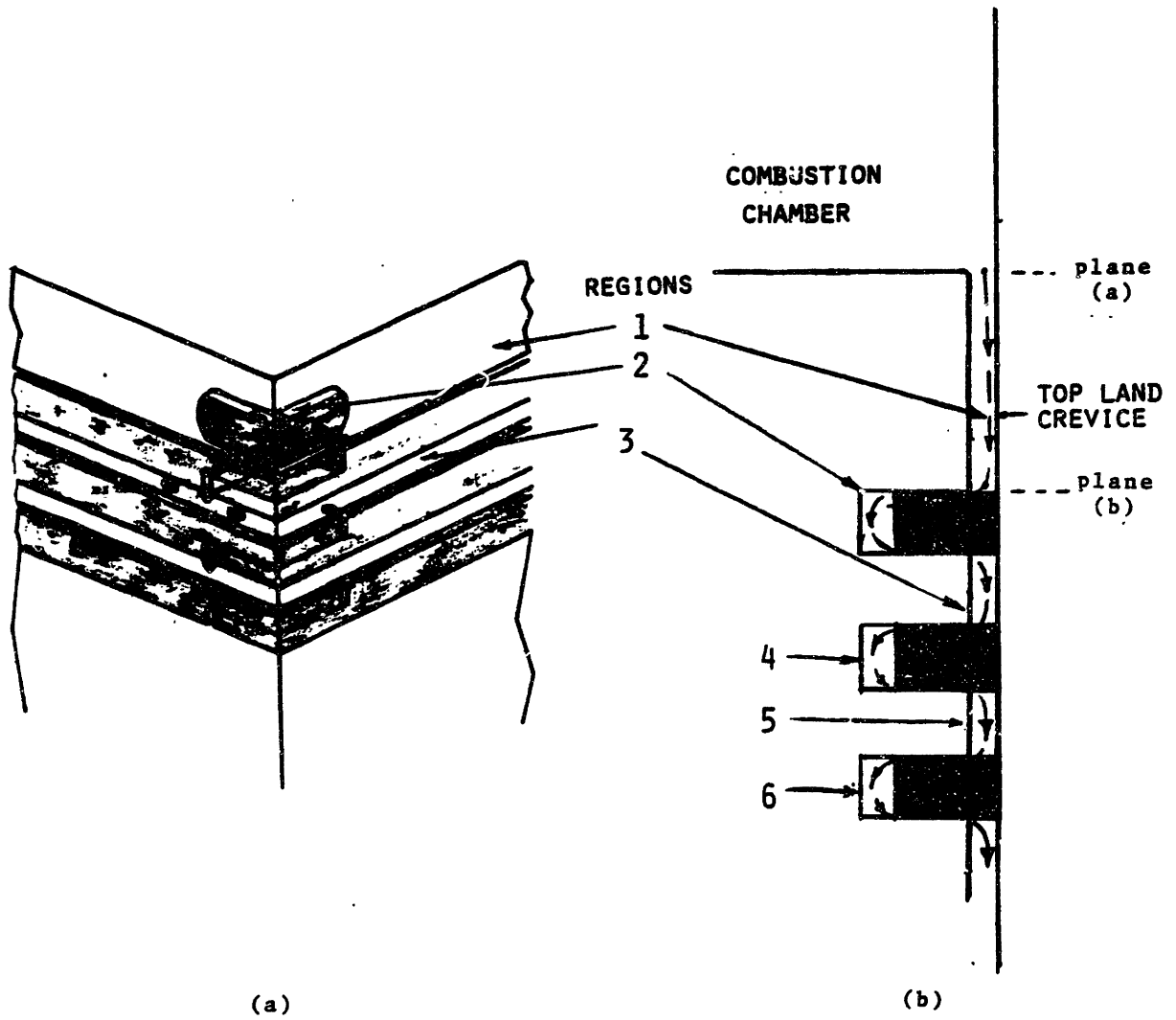
Fig 5.1 - Model geometry of the crevice regions in the square cross section piston-cylinder engine.
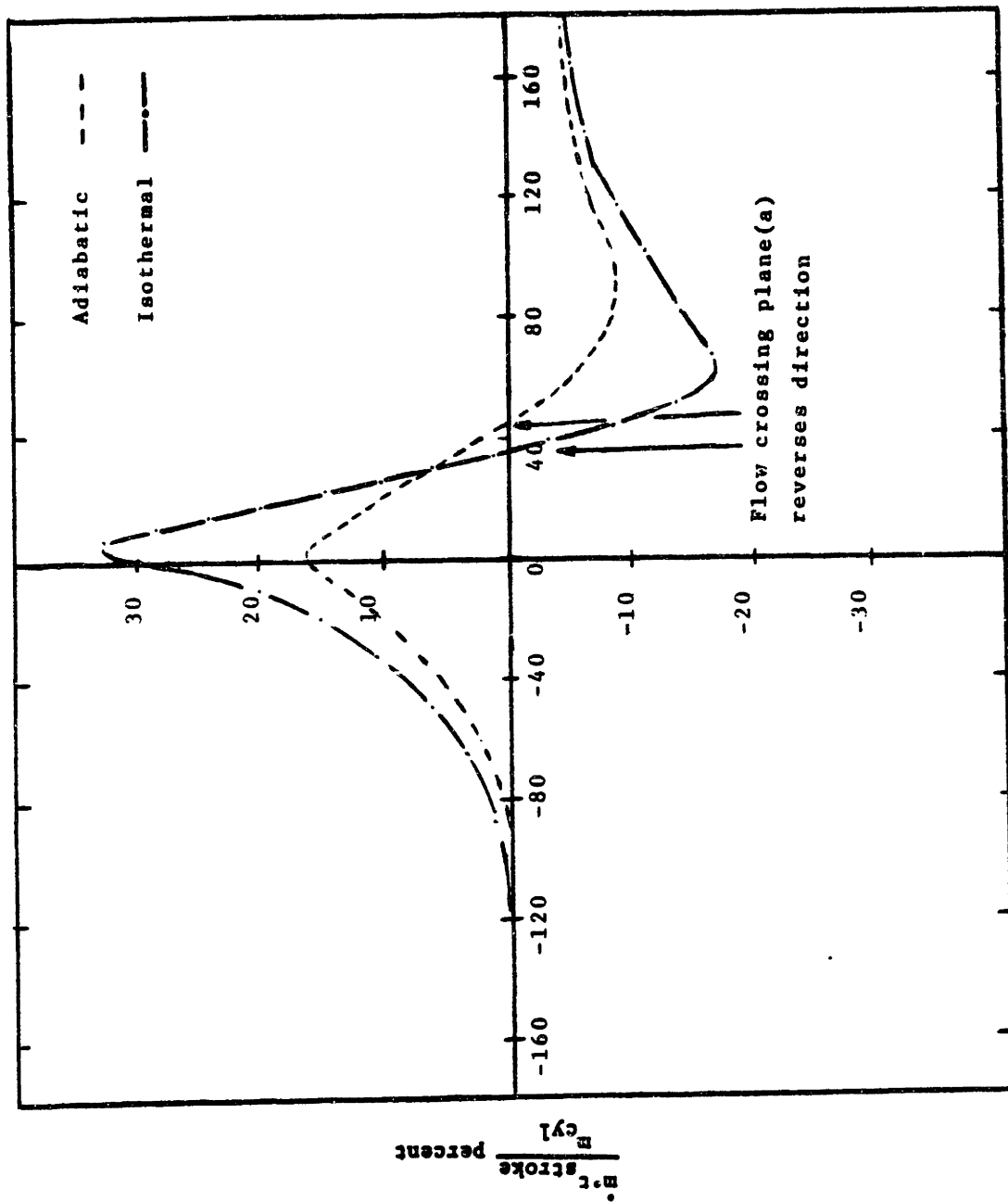
Fig 5.2 - The mass flow rate crossing the entrance of the top land crevice (plane (a) in Fig 5.1). The engine is operating at 1380 rpm and half load.
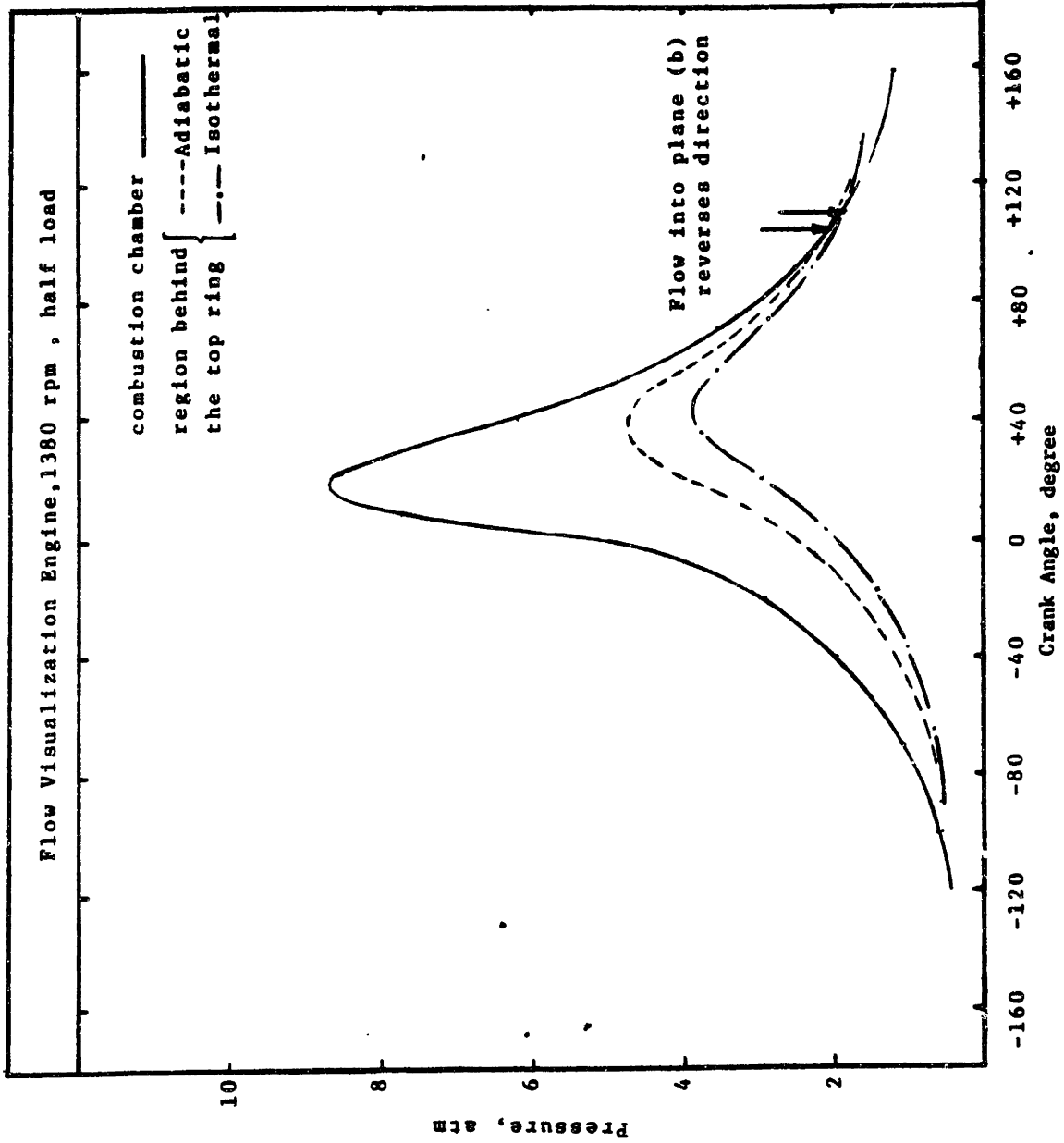
Fig 5.3 - Measured pressure of the combustion chamber and the calculated pressure of the region behind the top ring.
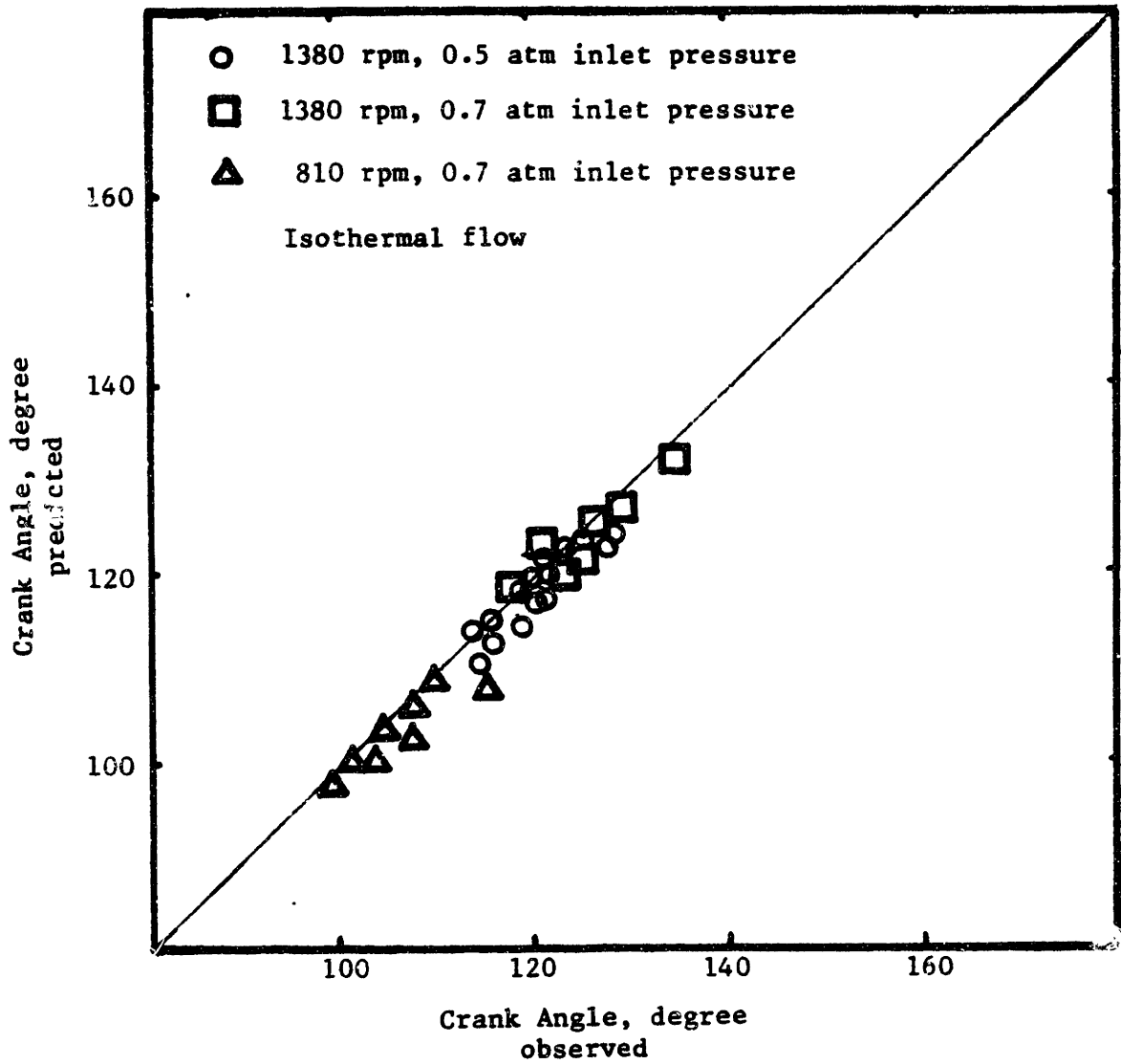
Fig 5.4 - Comparison between the observed timing (degree ATC) of the
jet-like flow out of top land crevice (plane (a) in Fig 5.1)
and predicted timing of the flow out of plane (b).

25 mm

.25 mm
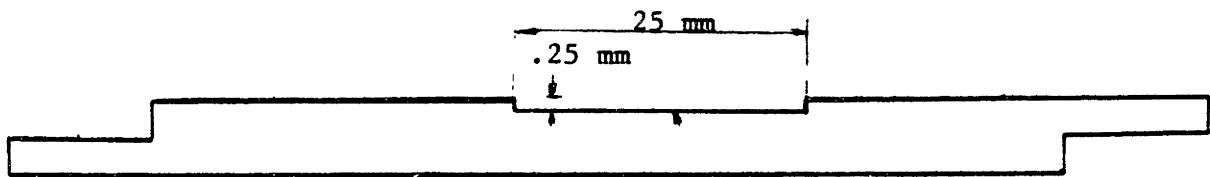
additional channel
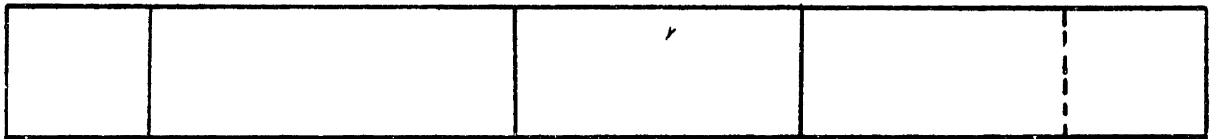
Fig 5.5 – Design of the square piston "ring" with an additional channel. The channel raises the passage area into the region behind the top ring by a factor of 4.
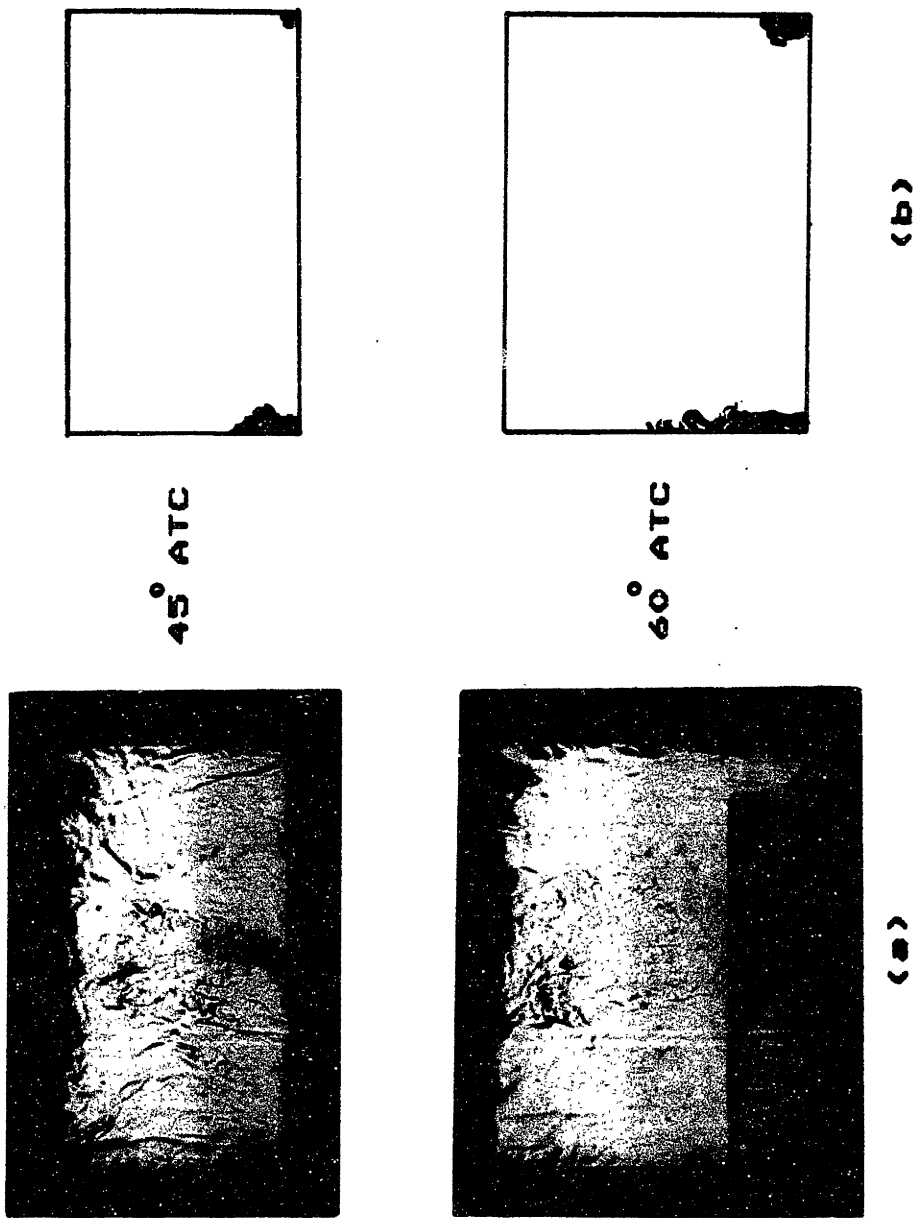
Fig 5.6 - Schlieren pictures (a) and schematic (b) for the square piston ring with an additional channel. The jet appears about 70 degrees earlier than that observed with the nominal ring.
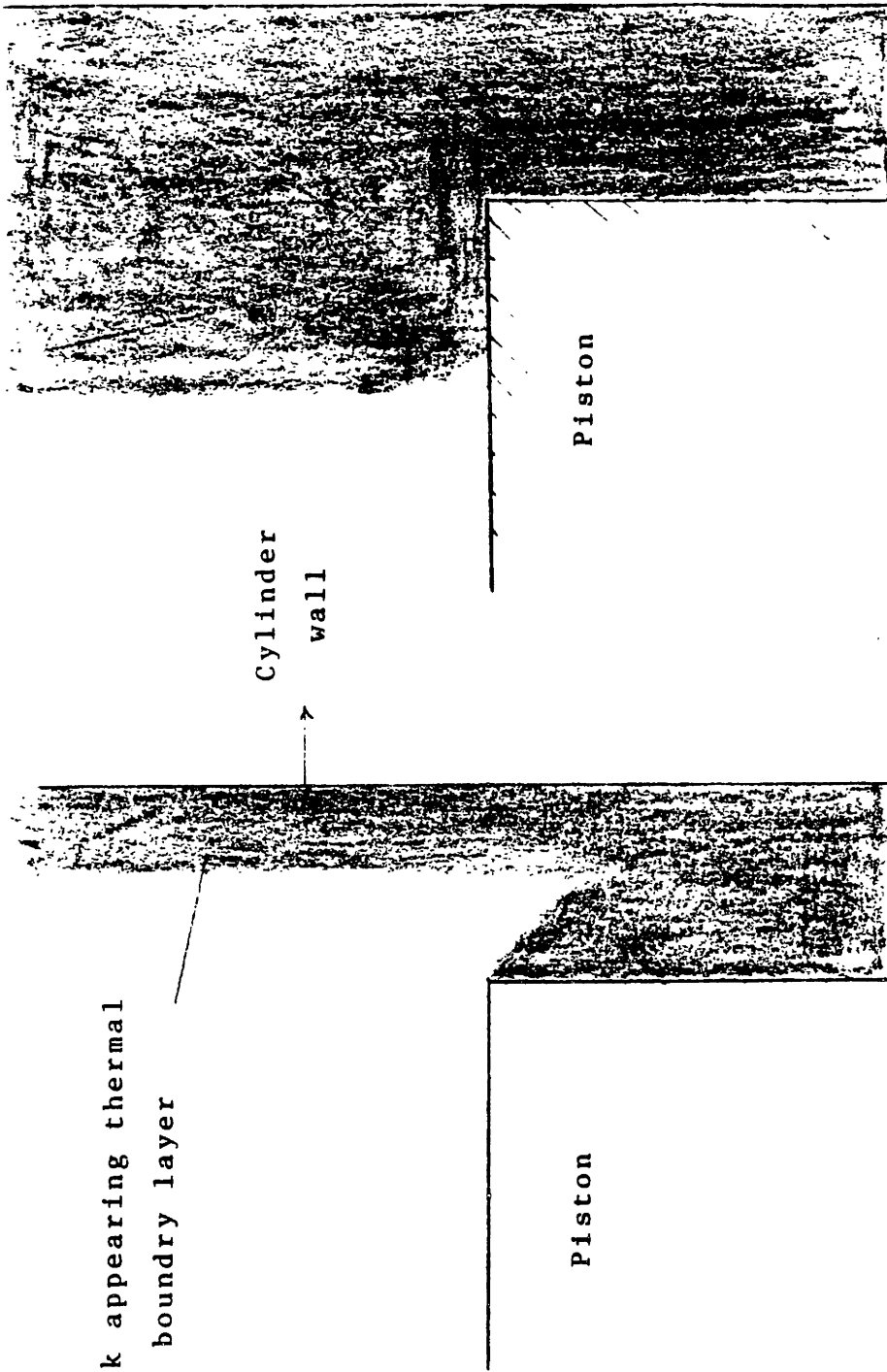
Fig 5.7 – Schematic of the dark layer on the combustion chamber wall obscuring the top land crevice entrance.
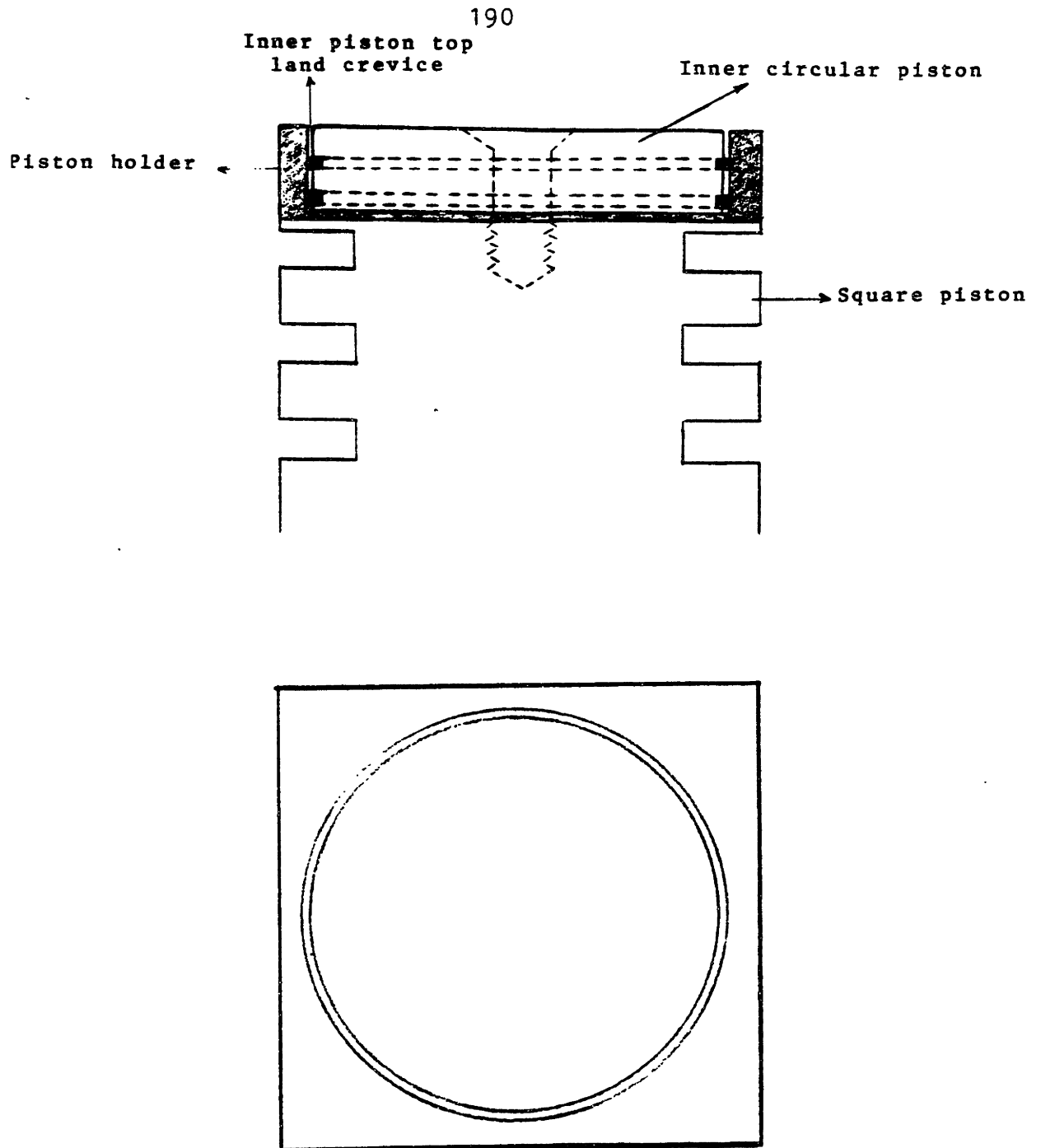
Fig 5.8 – Assembly to simulate a real engine's crevice regions. The ring belt of a conventional piston is press-fit into a piston holder. The assembly is secured to the top of the square piston.
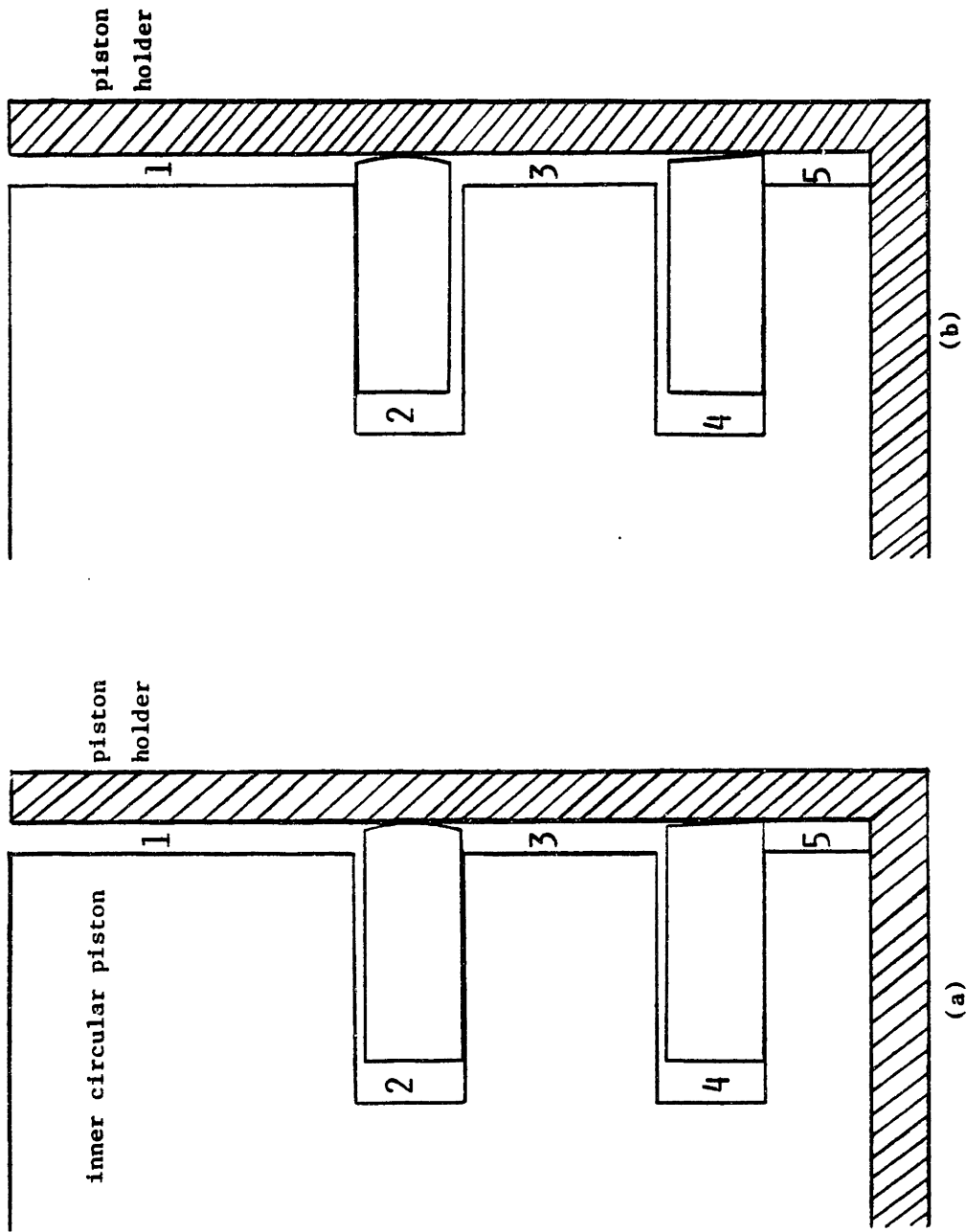
Fig 5.9 – Schematic showing the model geometry and position of the inner circular piston rings of Fig 5.8.

This page is intentionally left blank.

JET THROUGH INNER
PISTON RING GAP

40° ATC

EXPANDING FLOW OUT OF
INNER PISTON TOP LAND CREVICE

55° ATC
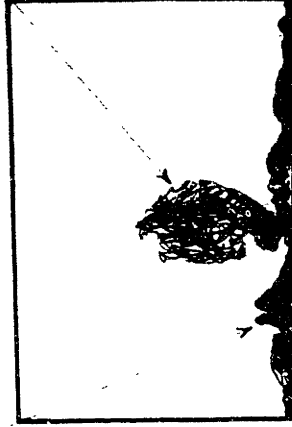
(b)

(a)

Fig. 5.10 - Schlieren pictures (a) and schematic (b) showing the flow
from the crevice regions for the inner circuler piston assembly of Fig. 5.8.
The top ring of the inner piston is fixed against the lower surface of
the groove.

Fig 5.11 – Comparison between the observed and predicted timing of the jet-like flow through the circular piston ring gap. The top ring of the circular piston is fixed on the lower surface of the groove (see Fig 5.9a).

This page is intentionally left blank.

40° ATC

55° ATC

(a)

(b)

JET THROUGH INNER
PISTON RING GAP

EXPANDING FLOW OUT OF
INNER PISTON TOP LAND CREVICE

Fig. 5.12 - Schlieren pictures (a) and schematic (b) showing the flow from the crevice regions for the inner circular piston assembly of Fig 5.8. The top ring of the inner piston is fixed against the upper surface of the groove.
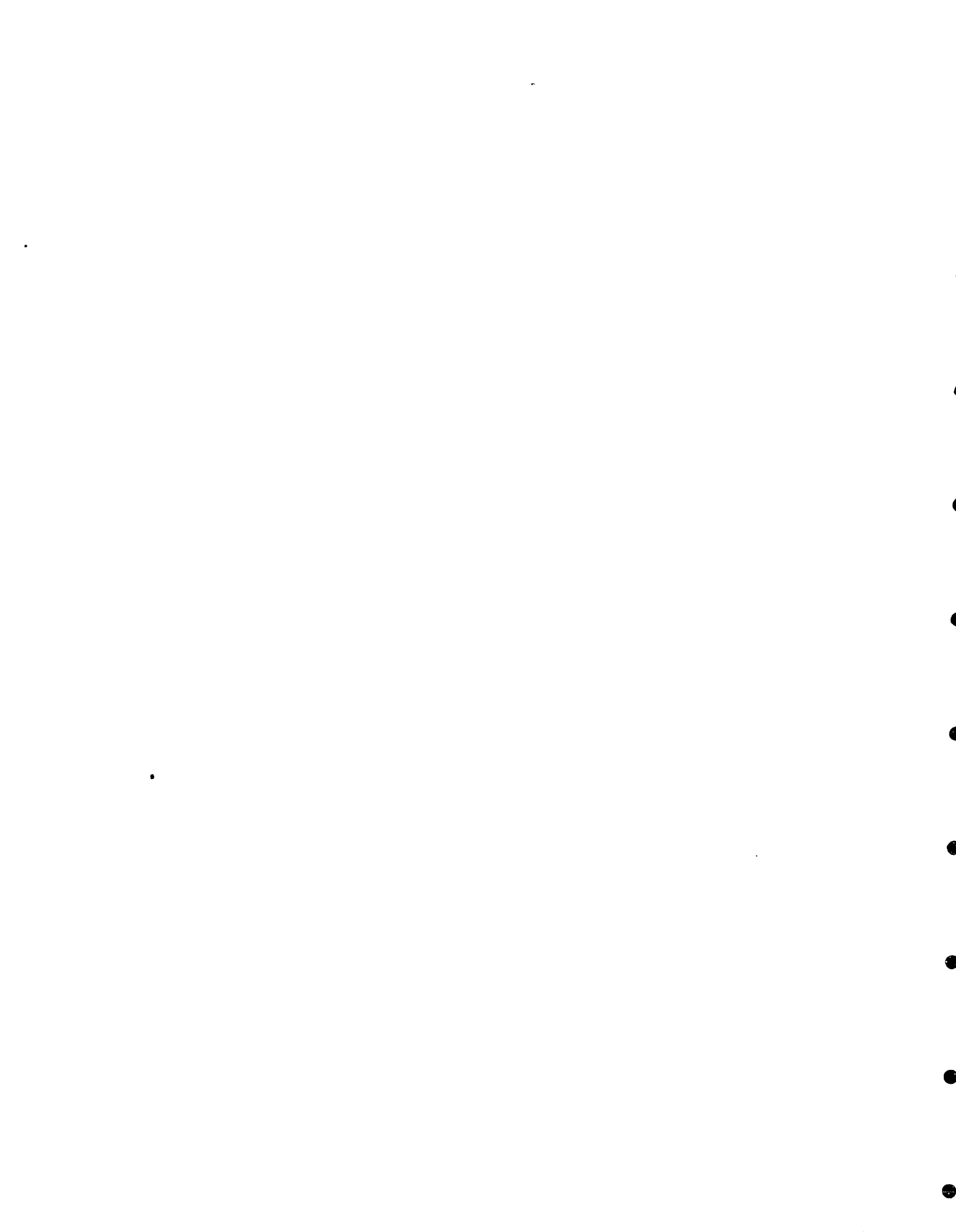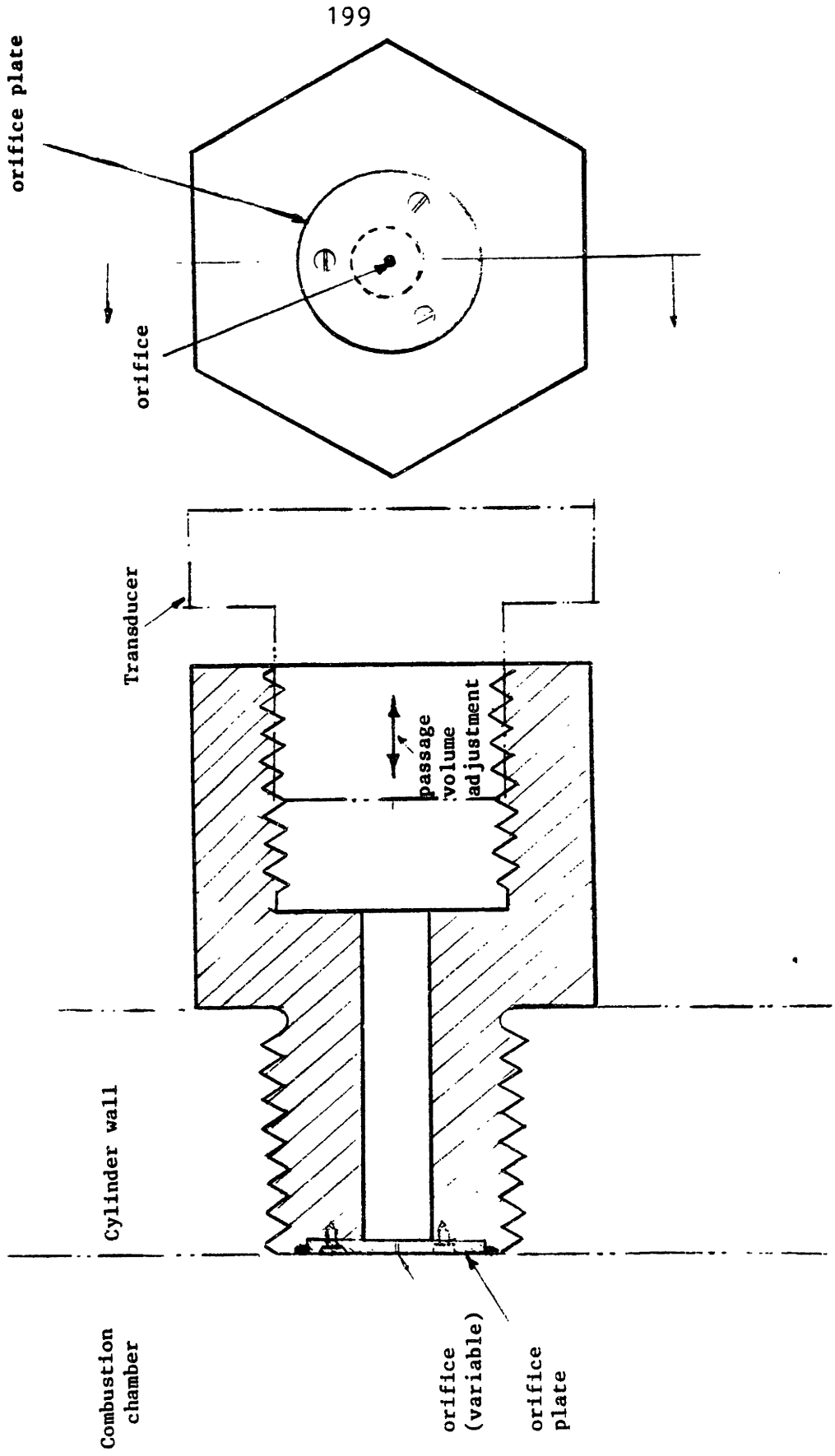
Fig 5.13 - Illustration of the plug used to study heat transfer assumptions.
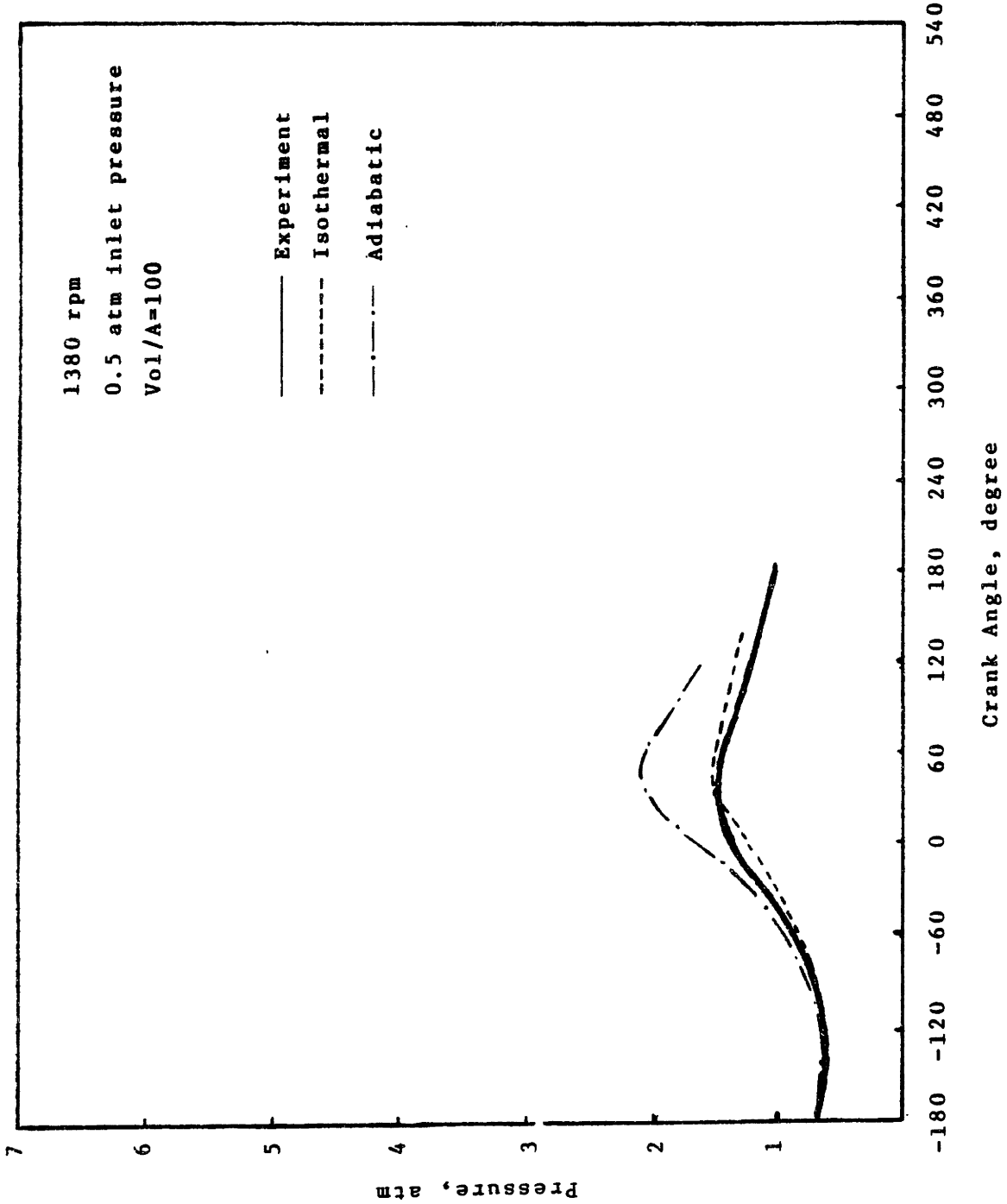
Fig 5.14 - Measured and calculated pressure traces inside the plug of Fig 5.13, comparing the
isothermal and adiabatic assumptions.
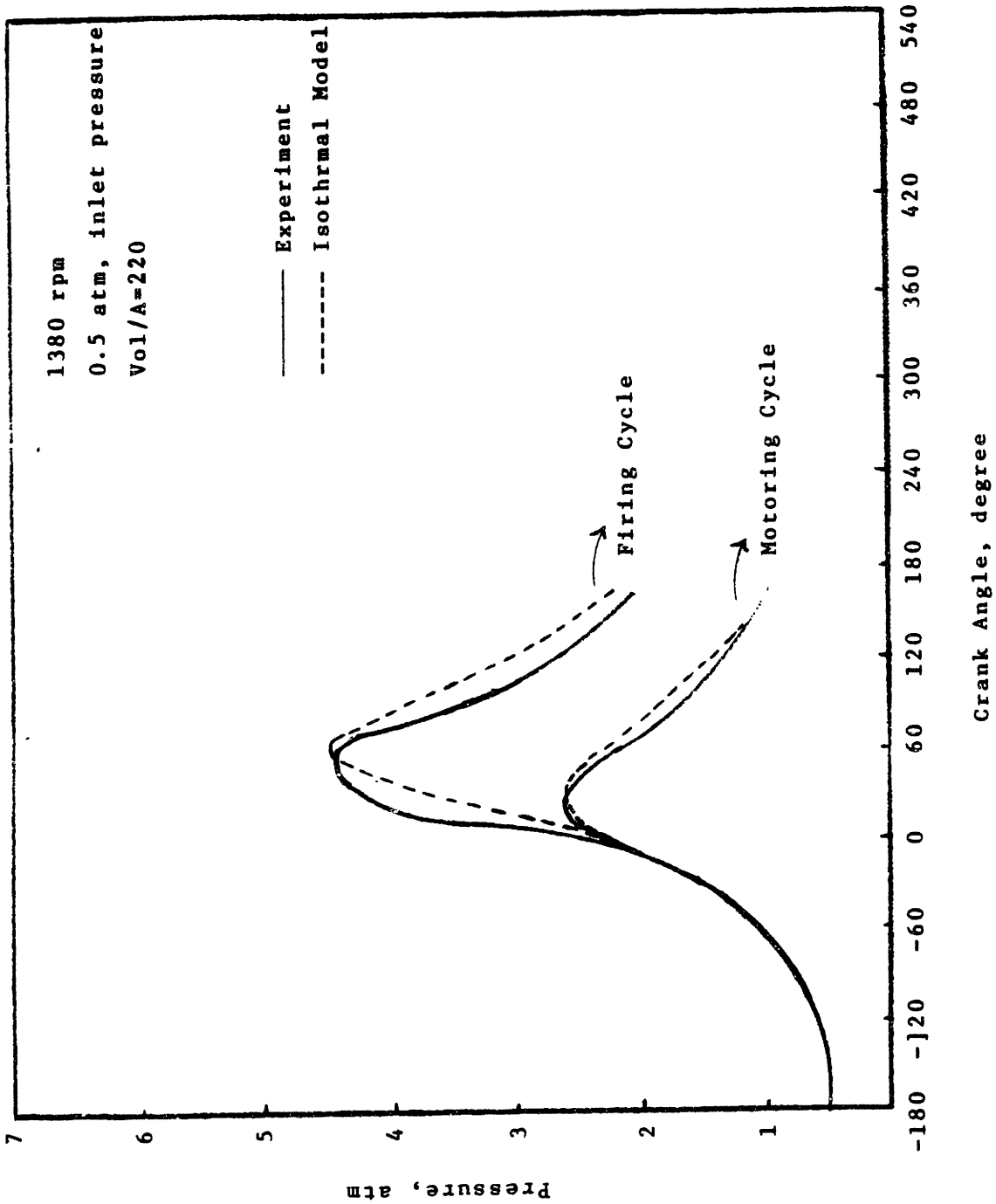
Fig 5.15 - Measured and calculated pressure traces inside the plug of Fig 5.3 for a Vol/A ratio representative of a real engine geometry.

Top land crevice

Ring gap

Combustion chamber

Ring side clearance

Region behind top ring

Oil ring

1

2

3

4

5
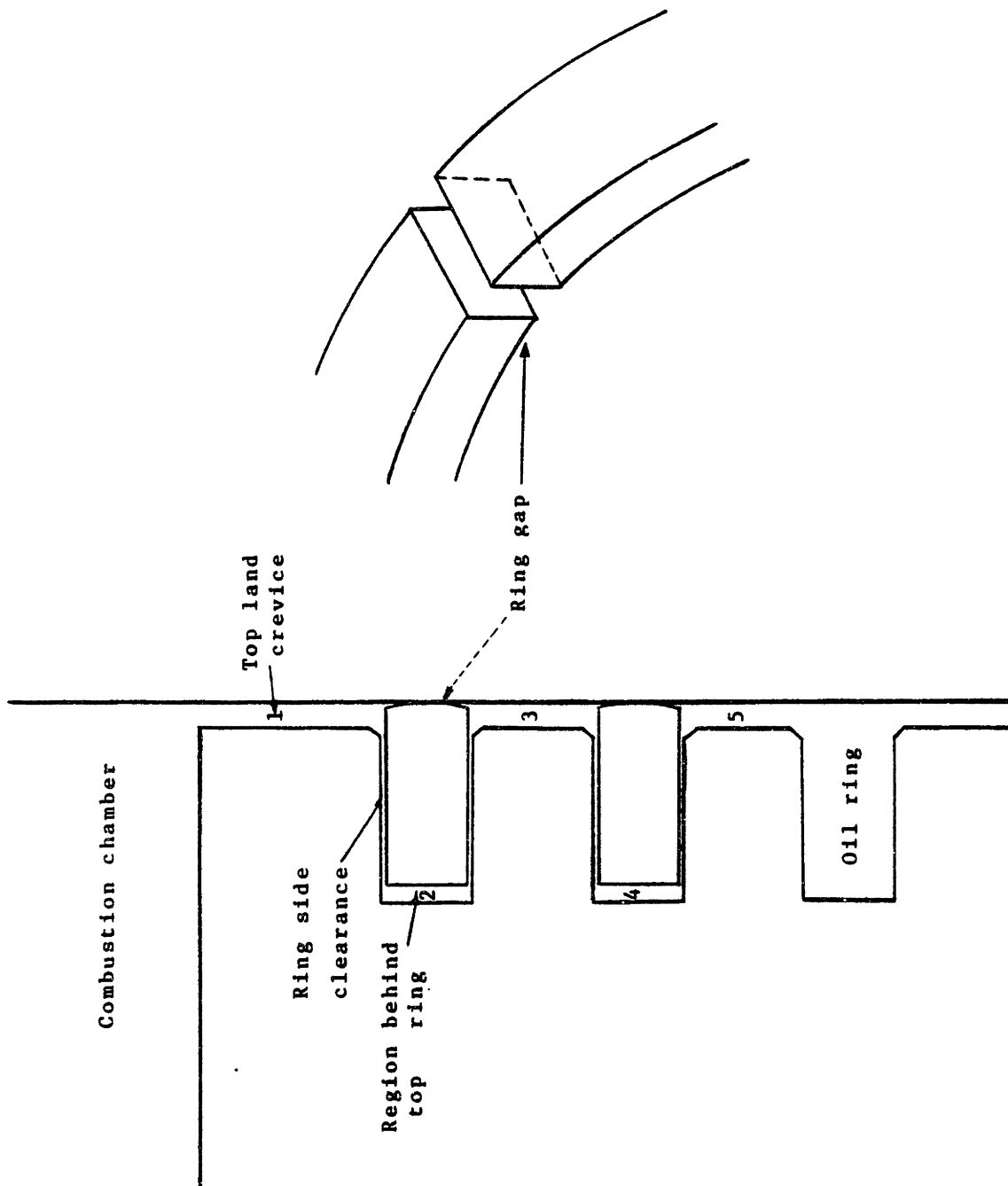
Fig 6.1 – Schematic of a conventional piston ring assembly showing the possible gas passages.
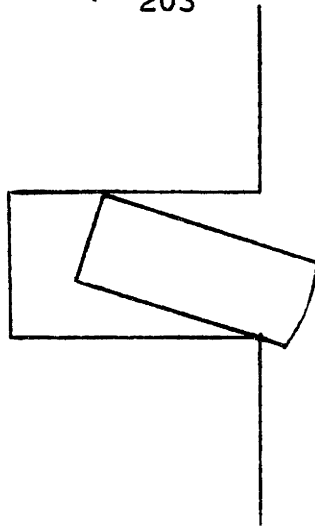
Fig 6.2 - An exaggerated schematic showing the ring fully blocking both ring side clearances.
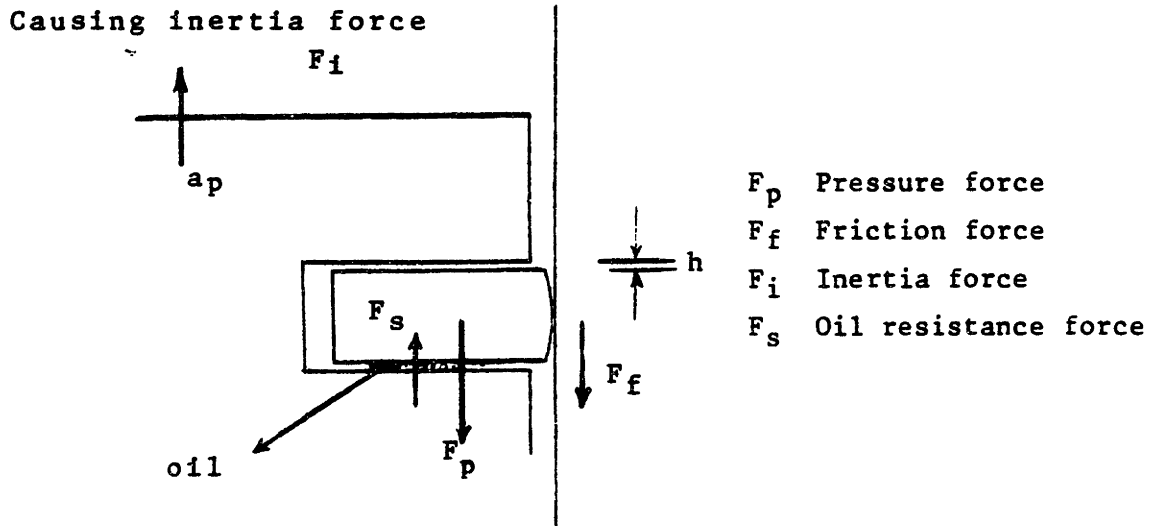
Fig 6.3 - Schematic of the forces acting on the top ring. The piston is moving upward and the ring is approaching the lower surface of the groove.

Combustion
chamber

Plane (a)

Top land crevice
region

1

Flow through the ring side
clearance channel; all over
circumfrence

Plane (b)

Region behind
the top ring

2

Flow through the
ring gap

Plane (c)

3

4

Plane (d)

5

To crankcase
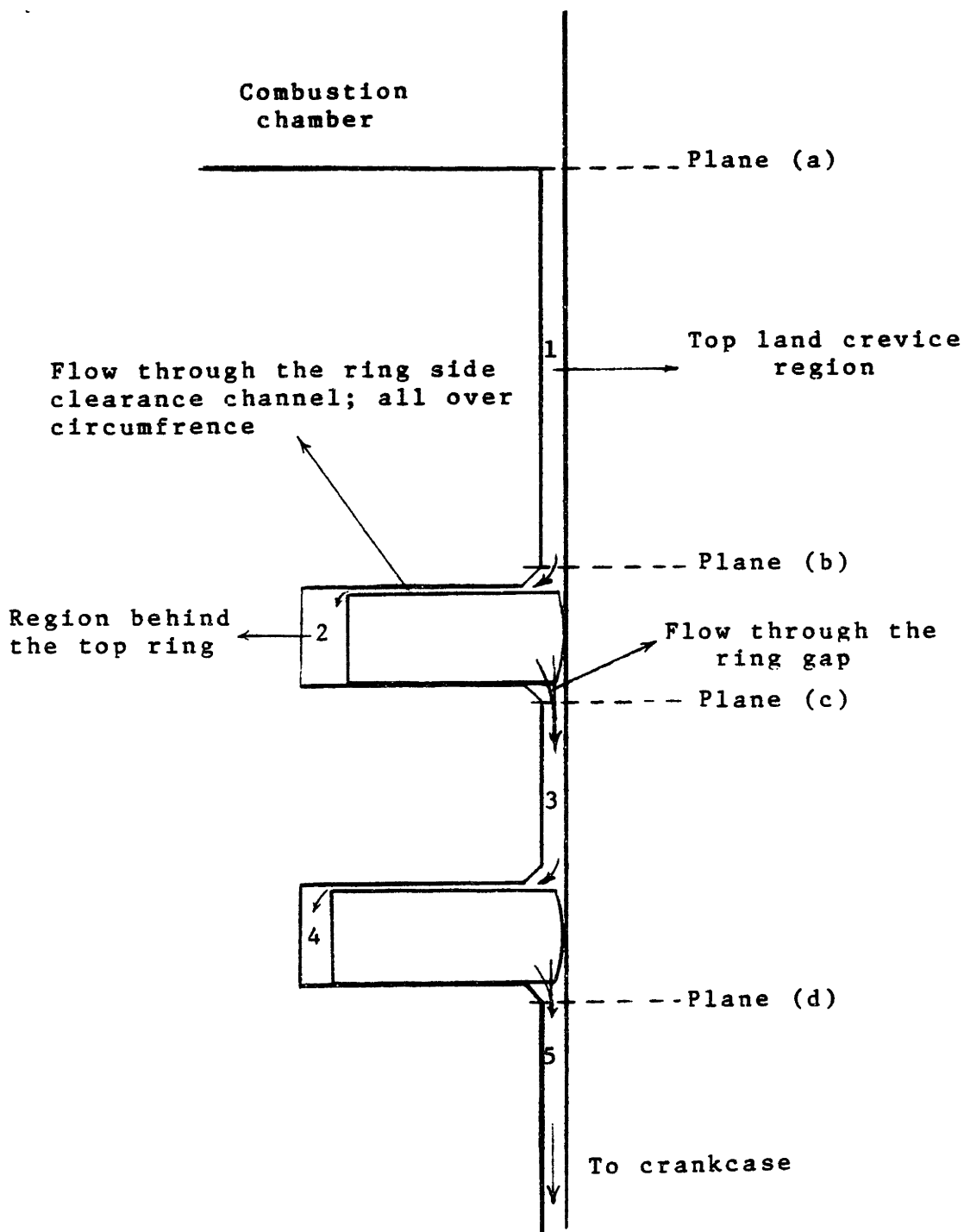
Fig 6.4 - Model geometry of the flow in the crevice regions of a
conventional engine.
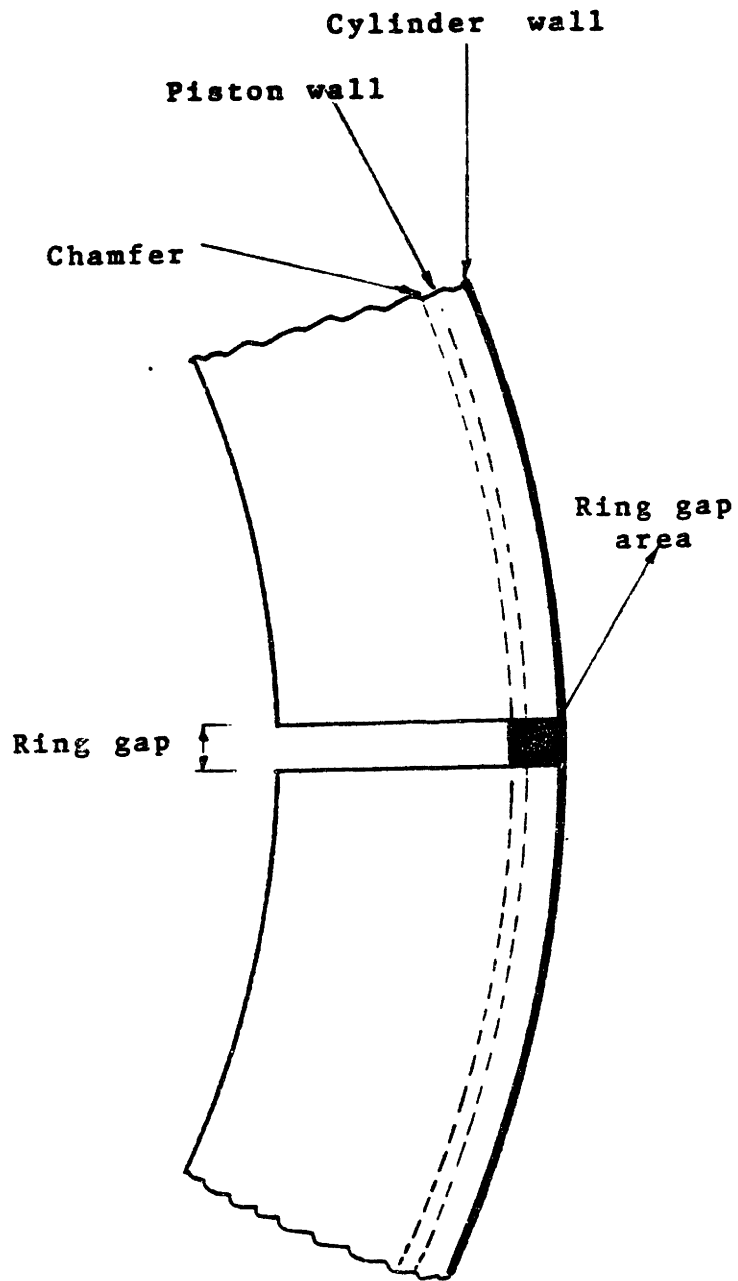
Fig 6.5 - Schematic of the passage area caused by the ring gap.
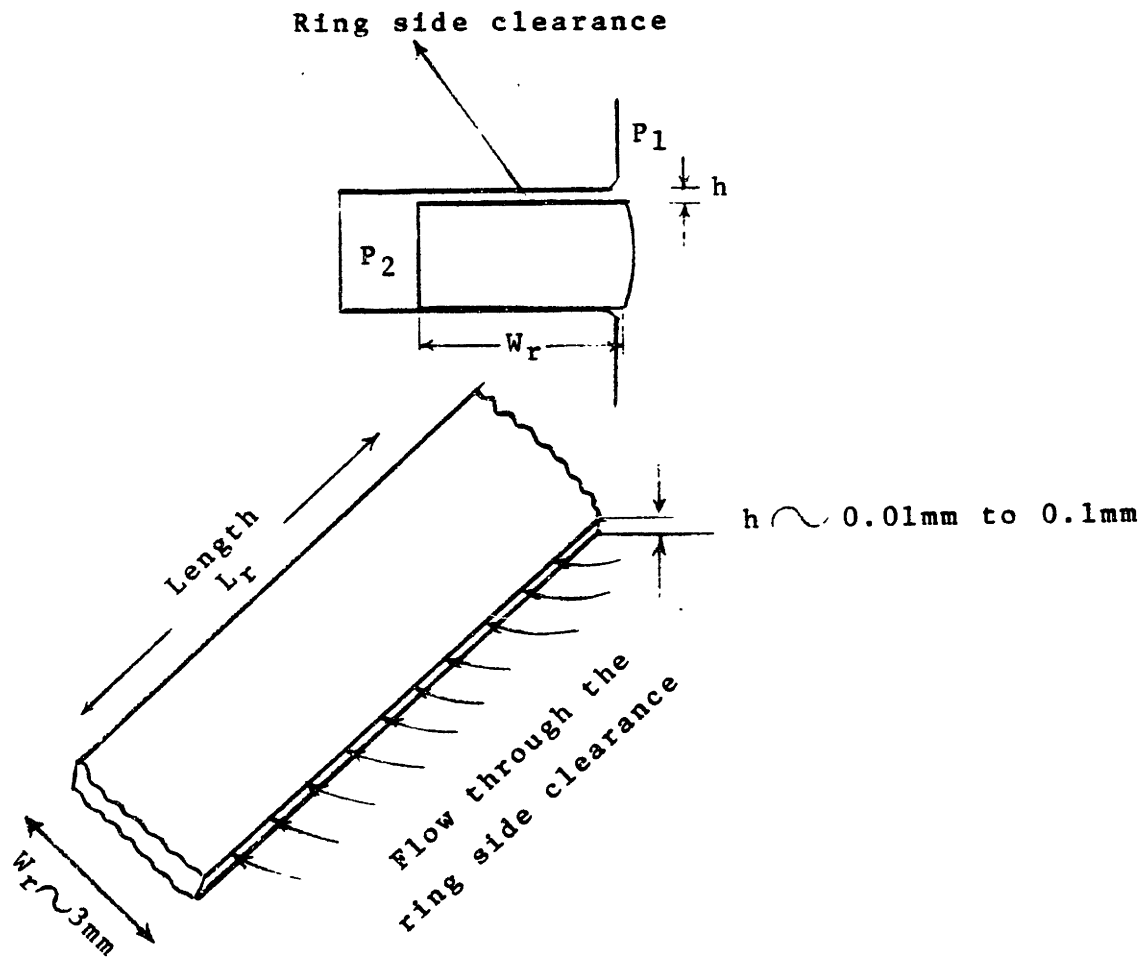
Fig 6.6 - Schematic of the ring side clearance flow.

This page is intentionally left blank.
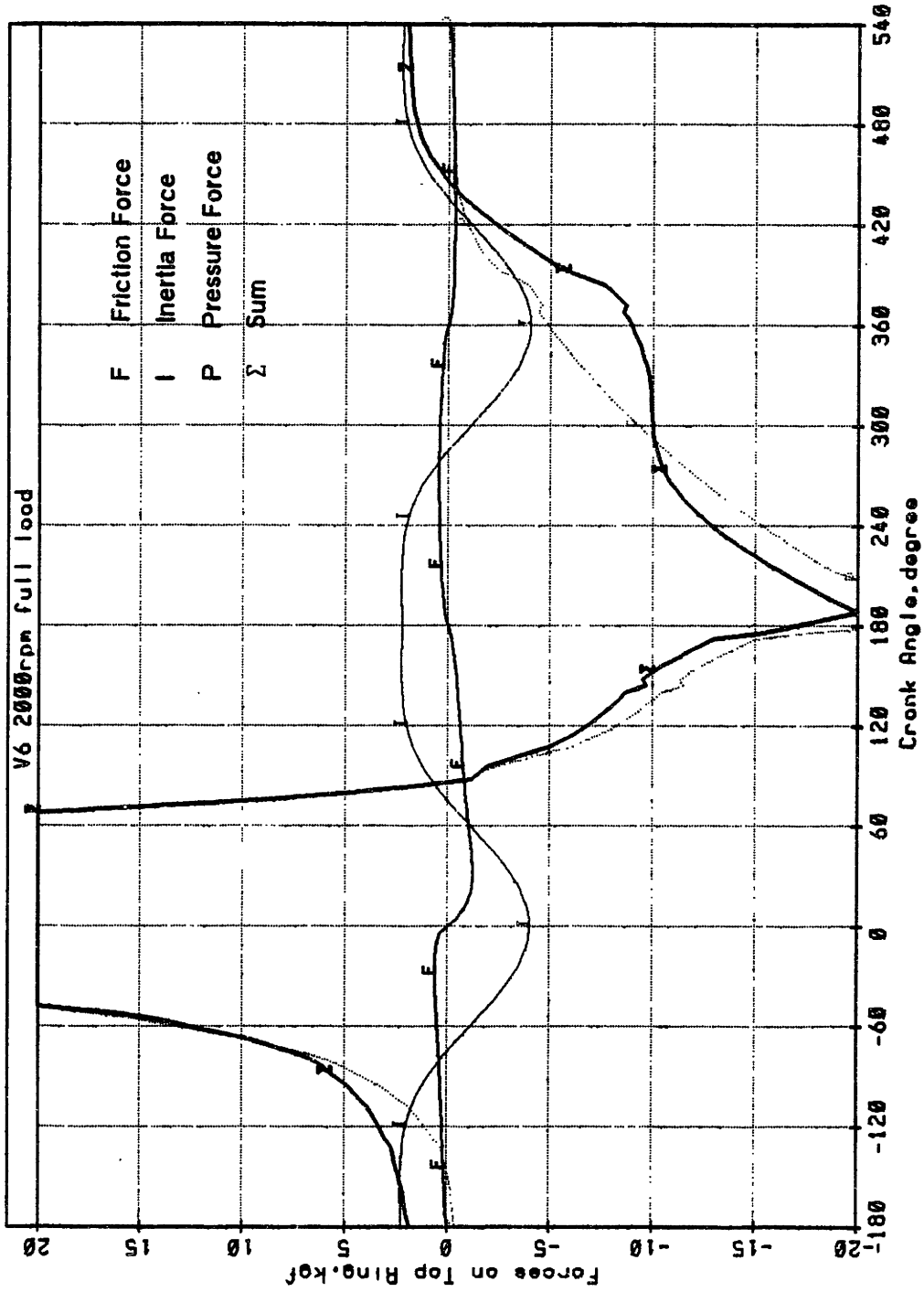
Fig 6.7I – Trace of forces acting on the top ring of V–6 engine operating at 2000 rpm and full load .
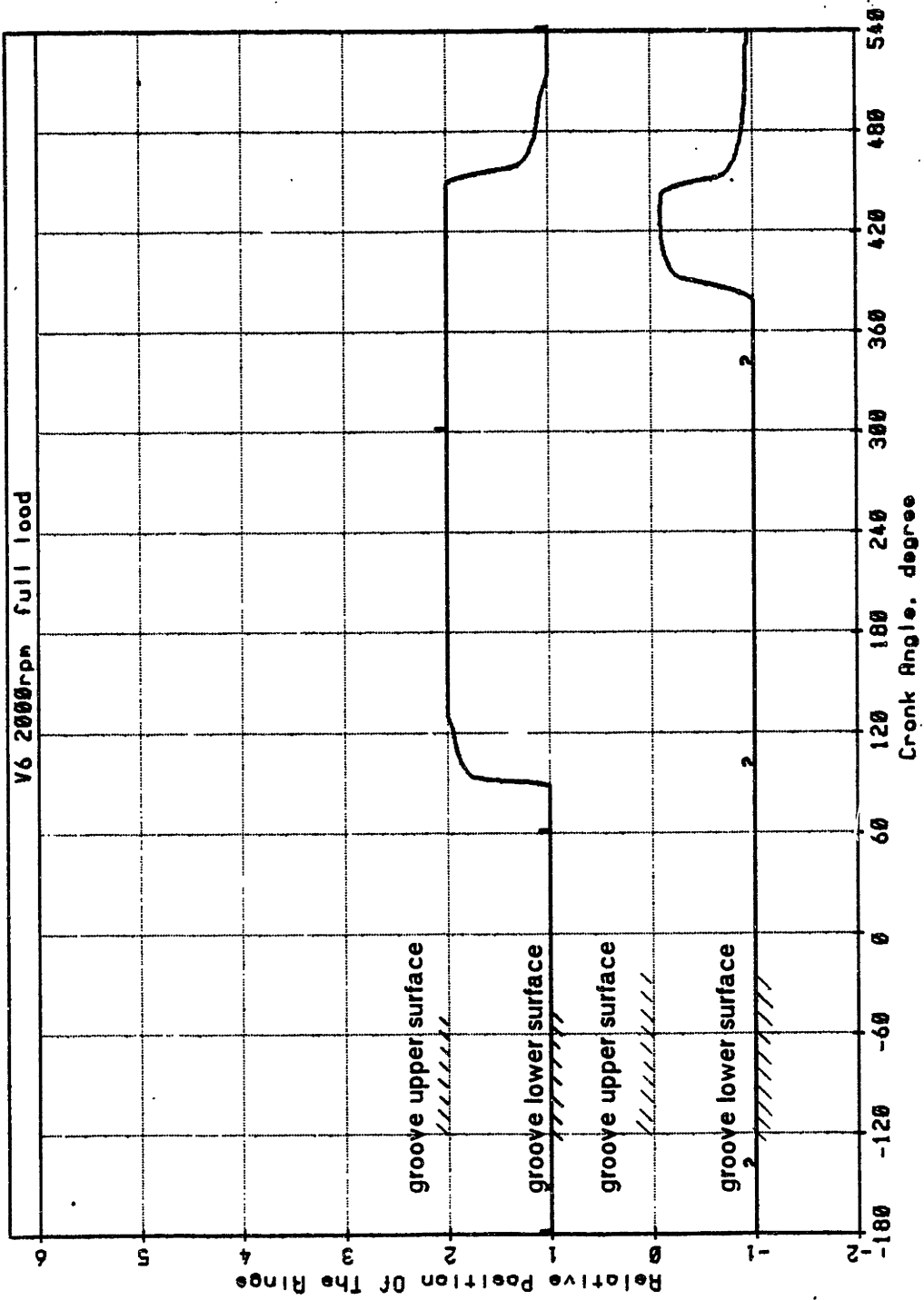
Fig 6.7II - Relative position of the top (1) and second (2) ring in the groove .
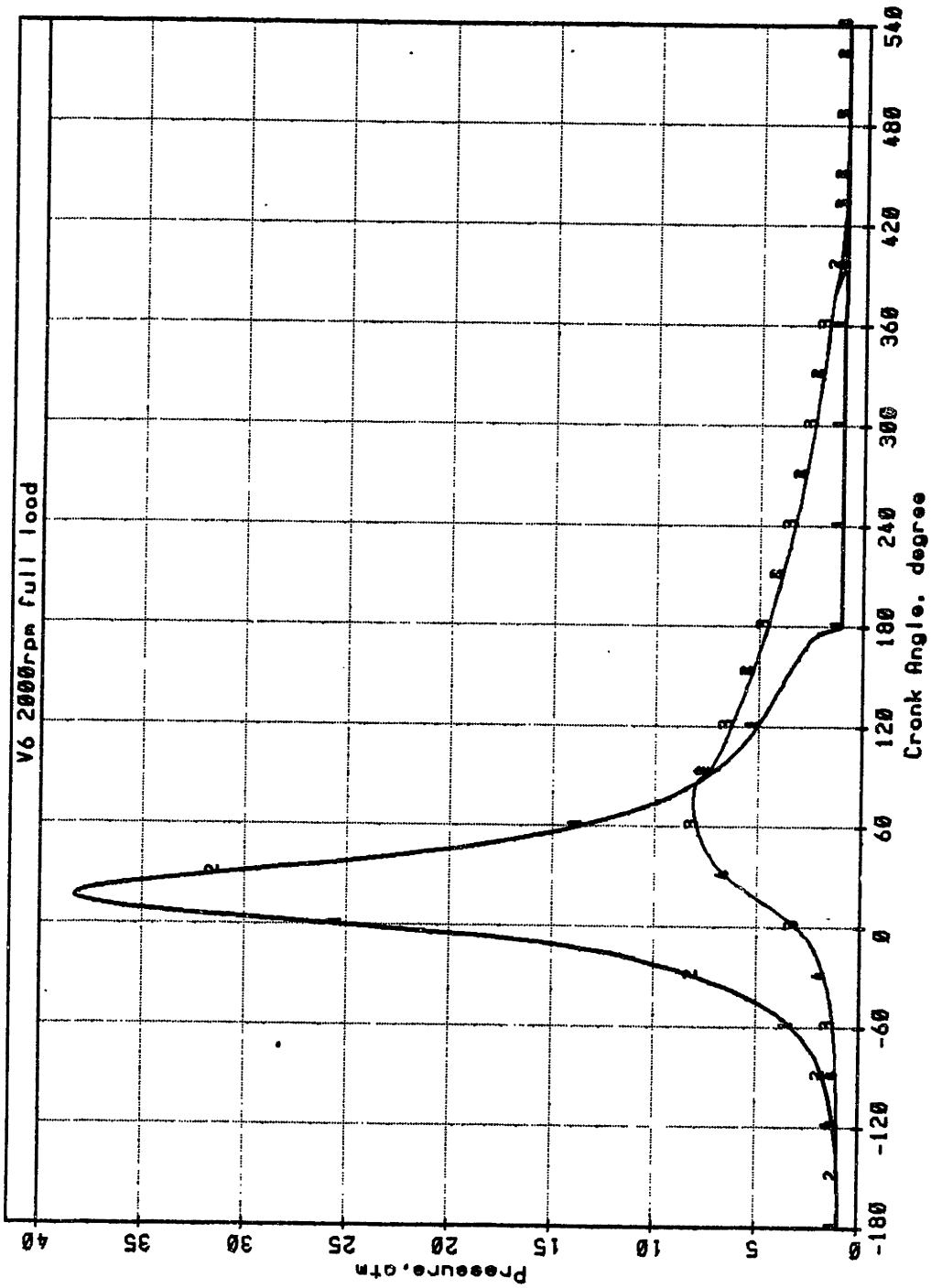
Fig 6.7III - Pressure trace of combustion chamber (1), region behind top ring (2), region between rings (3) and region behind second ring (4).
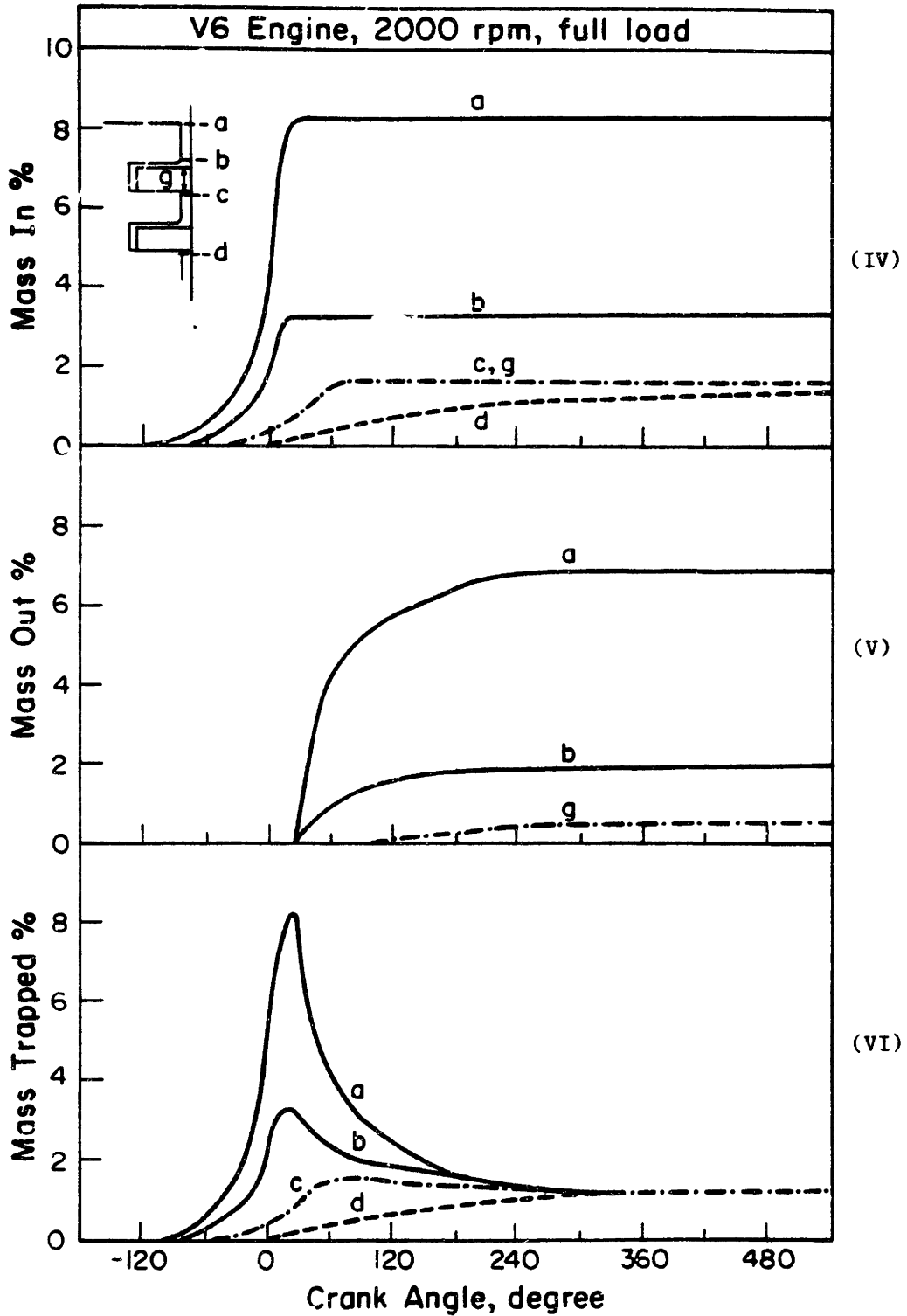
Fig 6.7 – Percentage of the charge mass that flows into (IV) and out of (V) planes (a), (b), (c) and (d) and through ring gap (g). The vertical distance between each two curves in (VI) is the mass trapped between the corresponding planes.

212
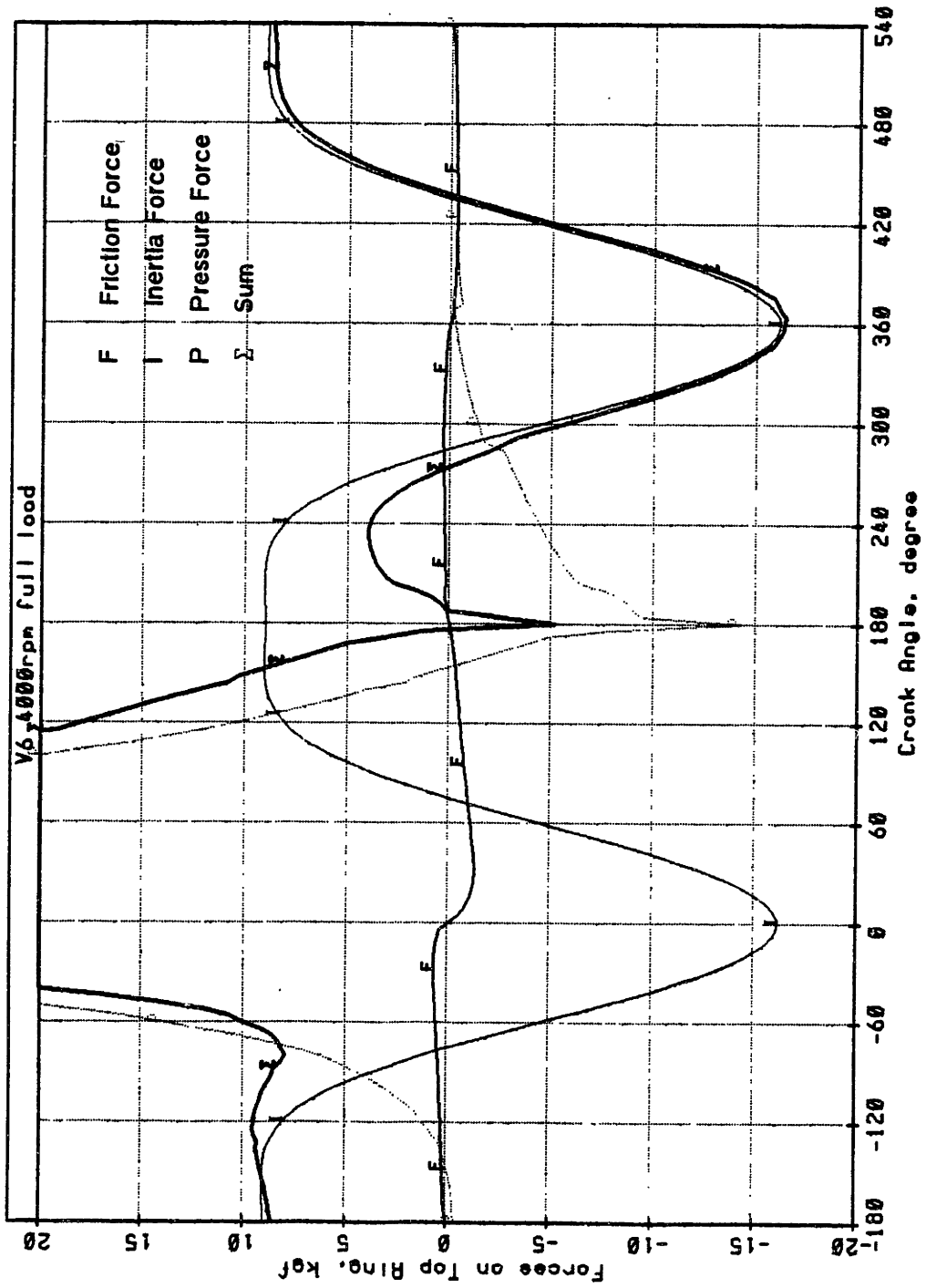
Fig 6.8I – Trace of forces acting on the top ring of V-6 engine operating at 4000 rpm and at full load .

213
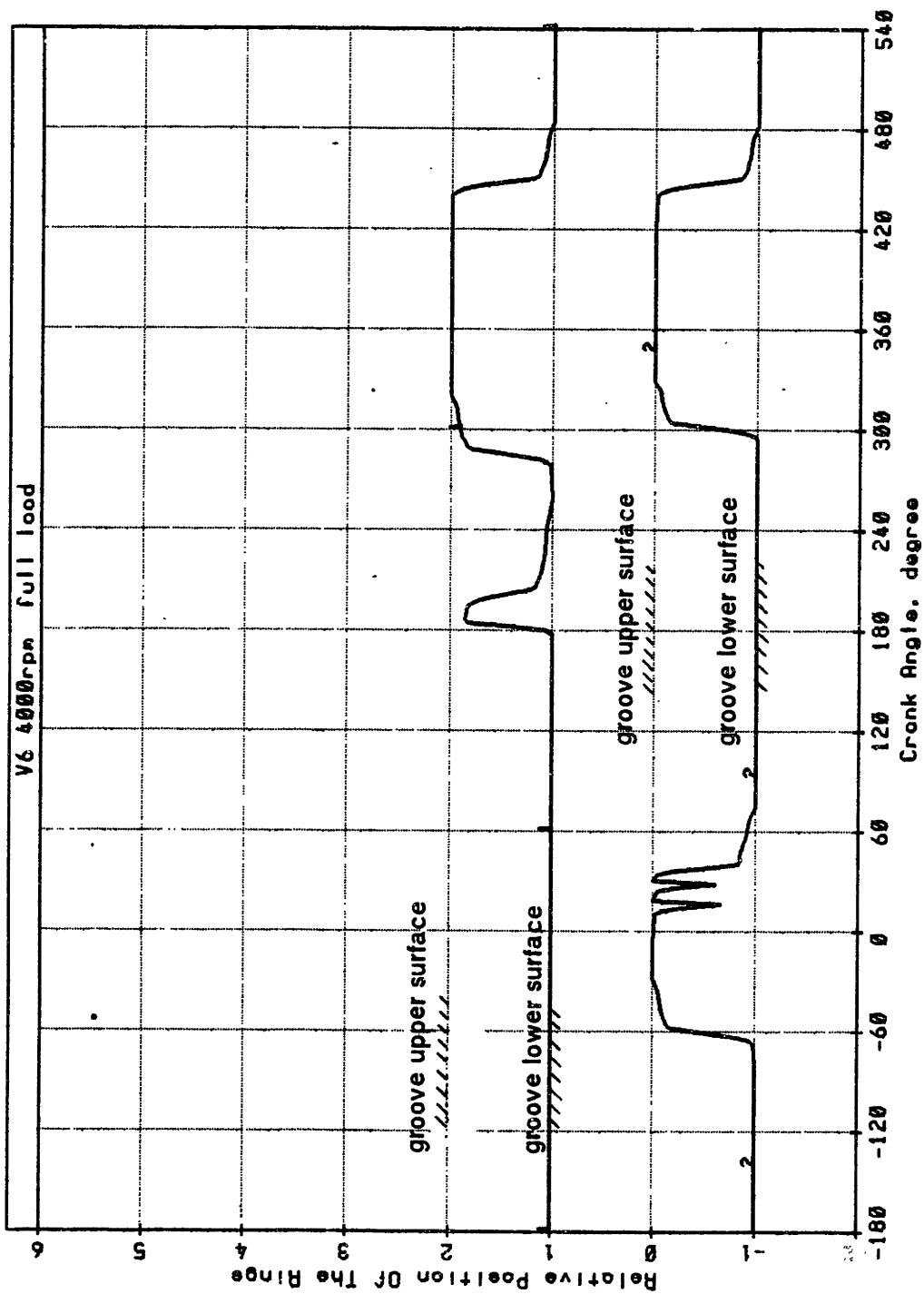
Fig 6.8II - Relative position of the top (1) and second (2) ring in the groove.
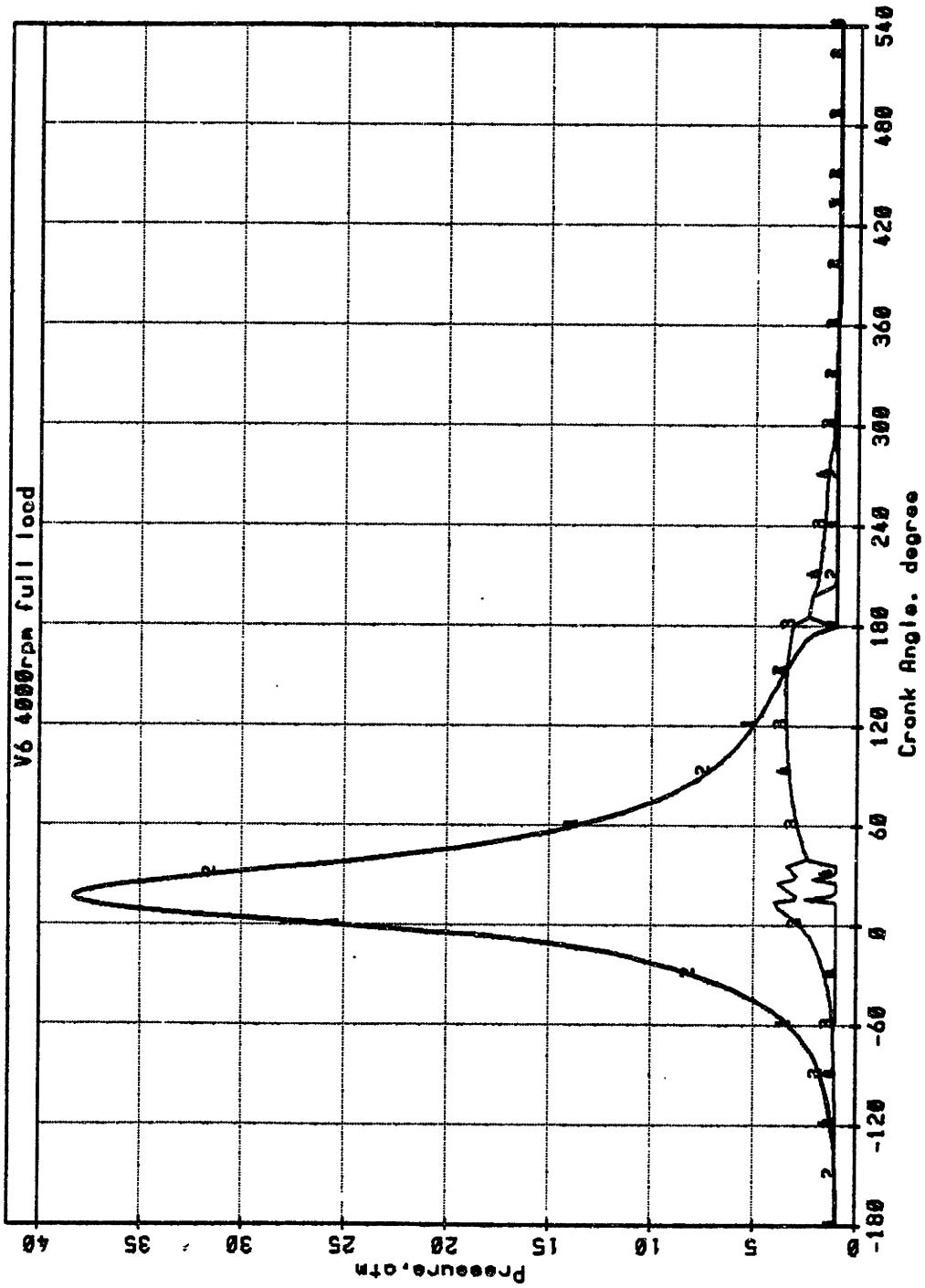
Fig 6.8III - Pressure trace of the combustion chamber (1), region behind top ring (2), region between rings (3) and region behind second ring (4) .
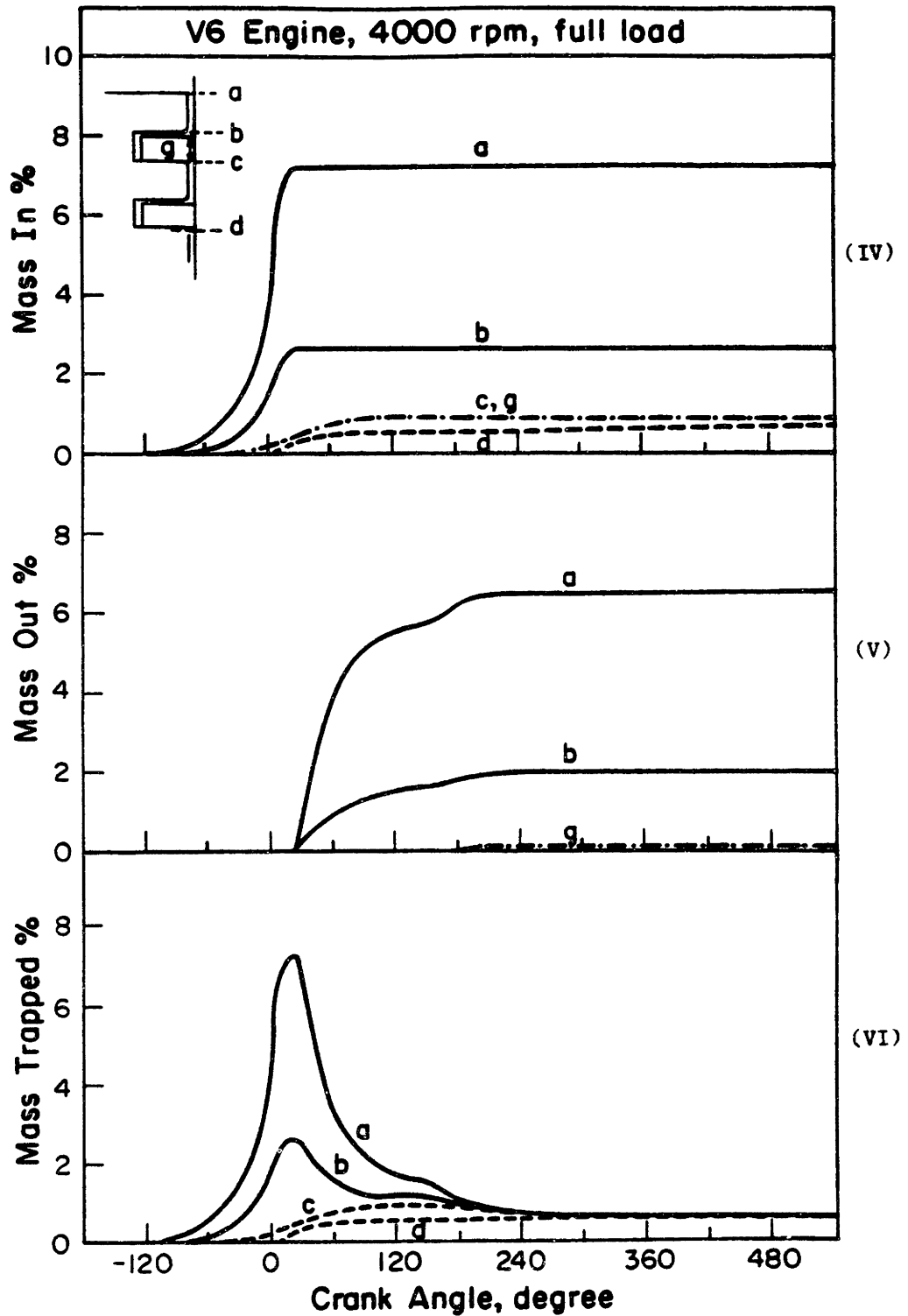
Fig 6.8 - Percentage of the charge mass that flows into (IV) and out of (V) planes (a), (b), (c) and (d) and through ring gap (g). The vertical distance between each two curves in (VI) is the mass trapped between the corresponding planes.
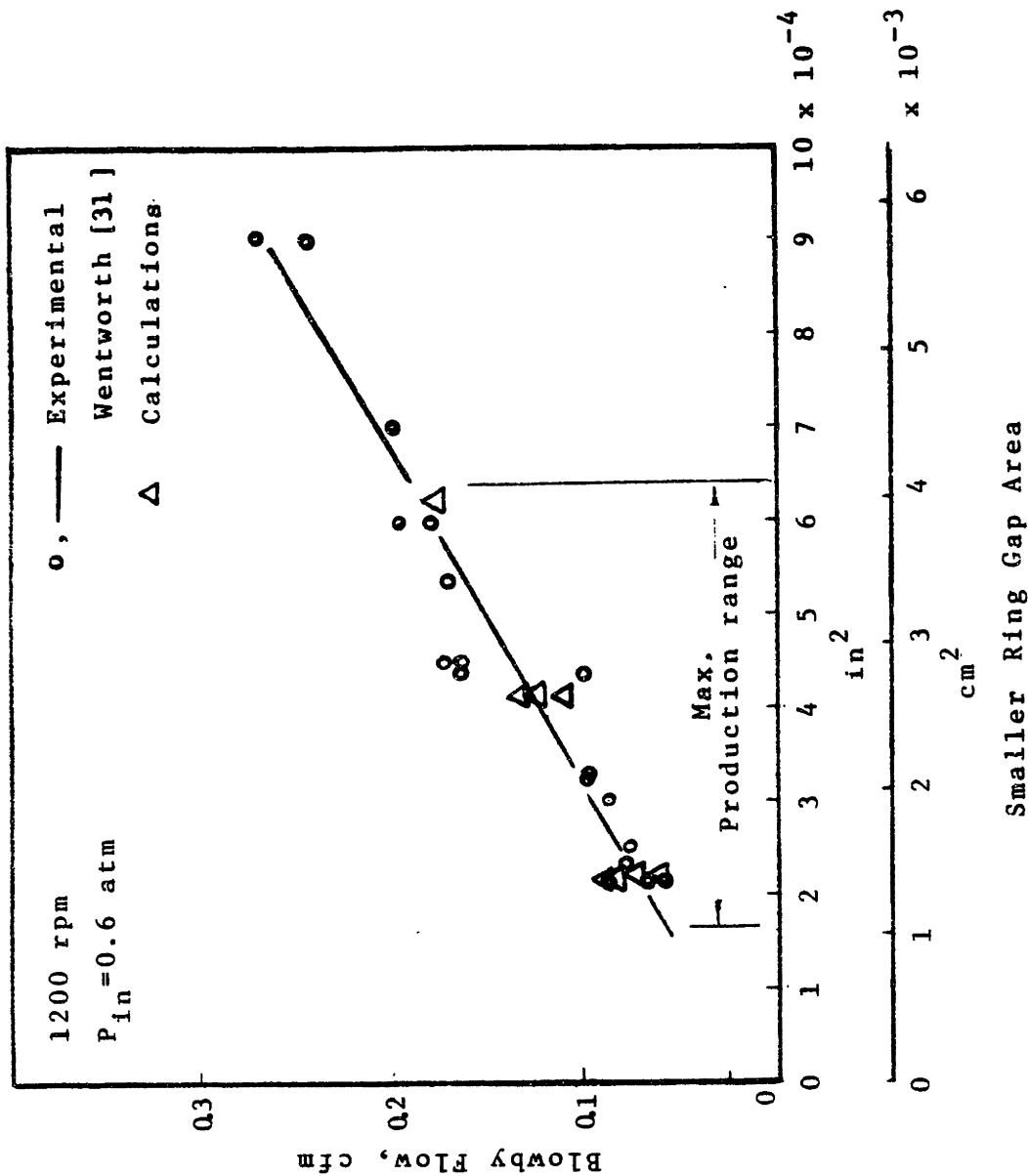
Fig 6.9 - Blowby flow rate versus the smaller ring gap area
for one V-6 cylinder with two compression rings .
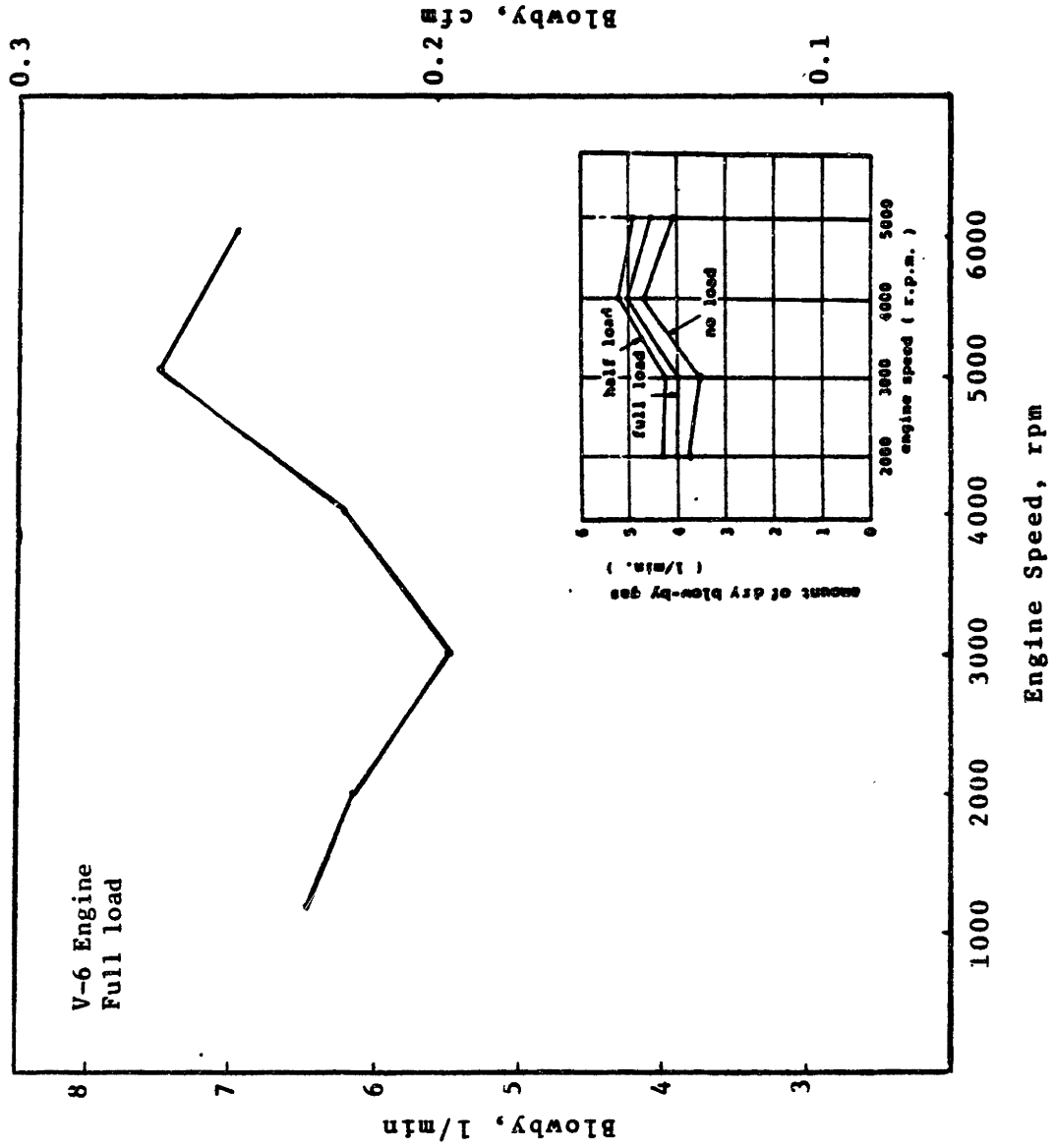
Fig 6.10 – Calculated blowby rate of one cylinder of V-6 engine operating at full load. The lower right graph shows experimental results in a smaller engine.
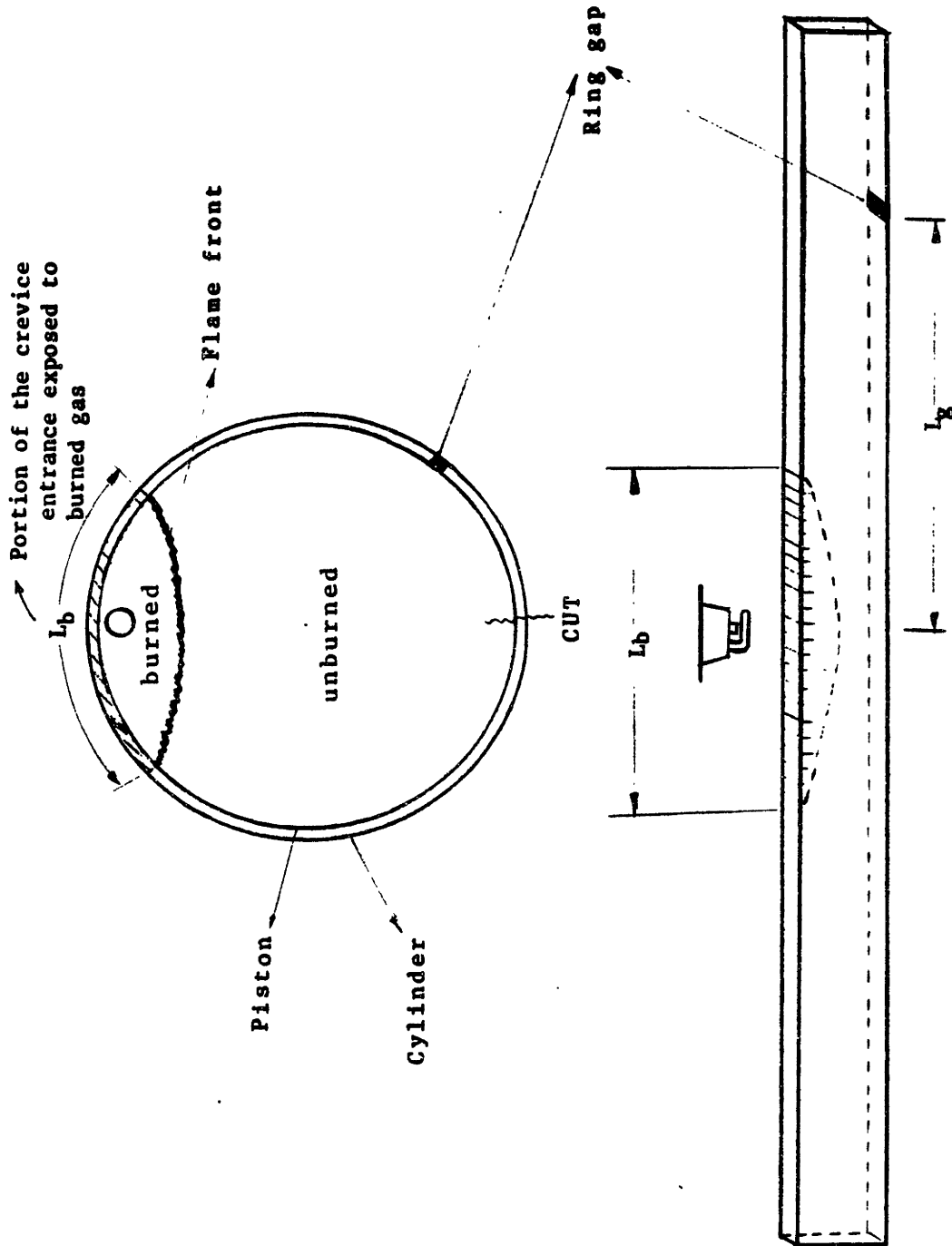
Fig 6.11 – Schematic of the top land crevice entrance model. The lower sketch shows the unwrapped top land crevice, cut at the opposite side of the spark plug.
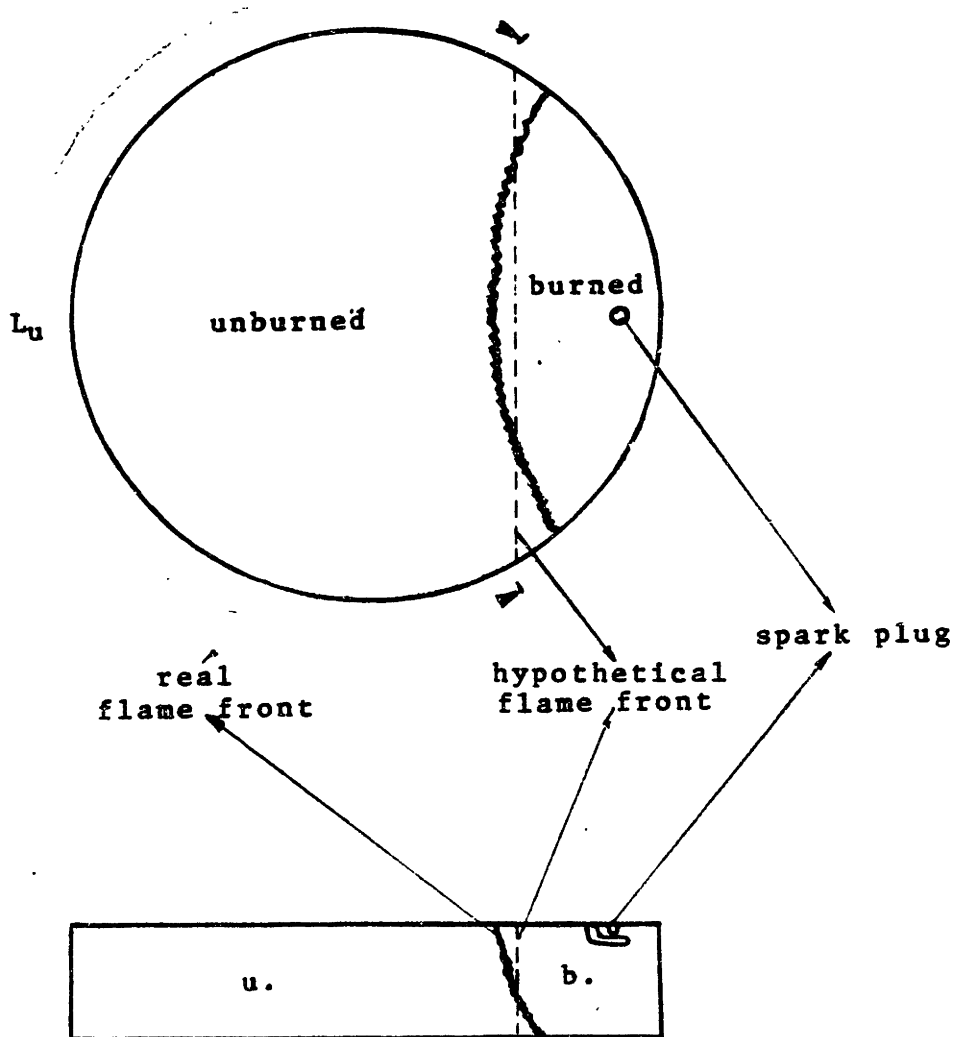
Fig 6.12 - Schematic showing the flame model used to calculate the portion of the top land crevice entrance exposed to unburned gas, i.e. L_u.
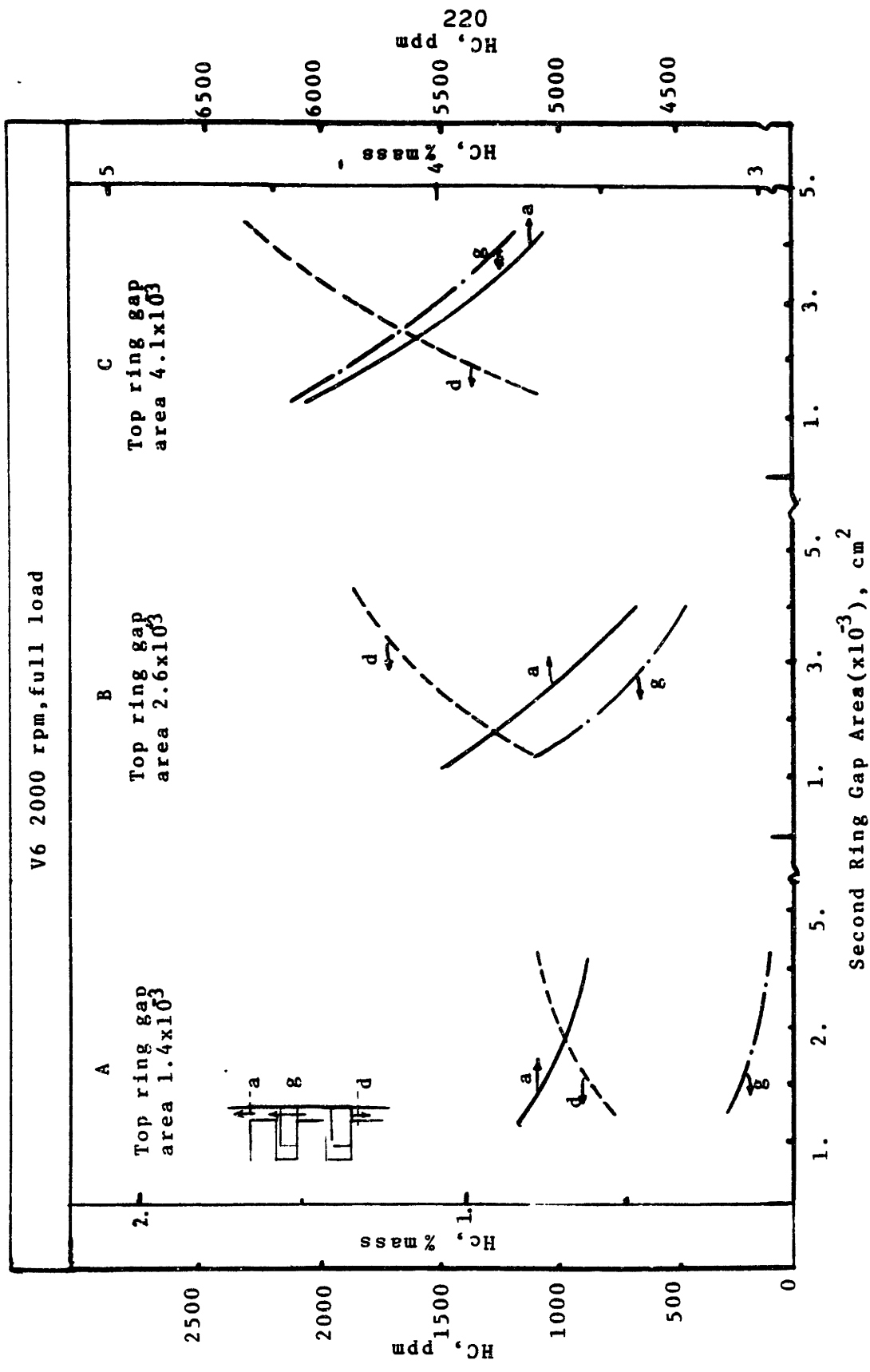
Fig 6.13 – The effect of ring gap area on the amount of hydrocarbon returning to the combustion chamber (a) and lost to blowby (d). Curve labled by (g) shows the amount of HC returning to combustion chamber through the top ring gap.
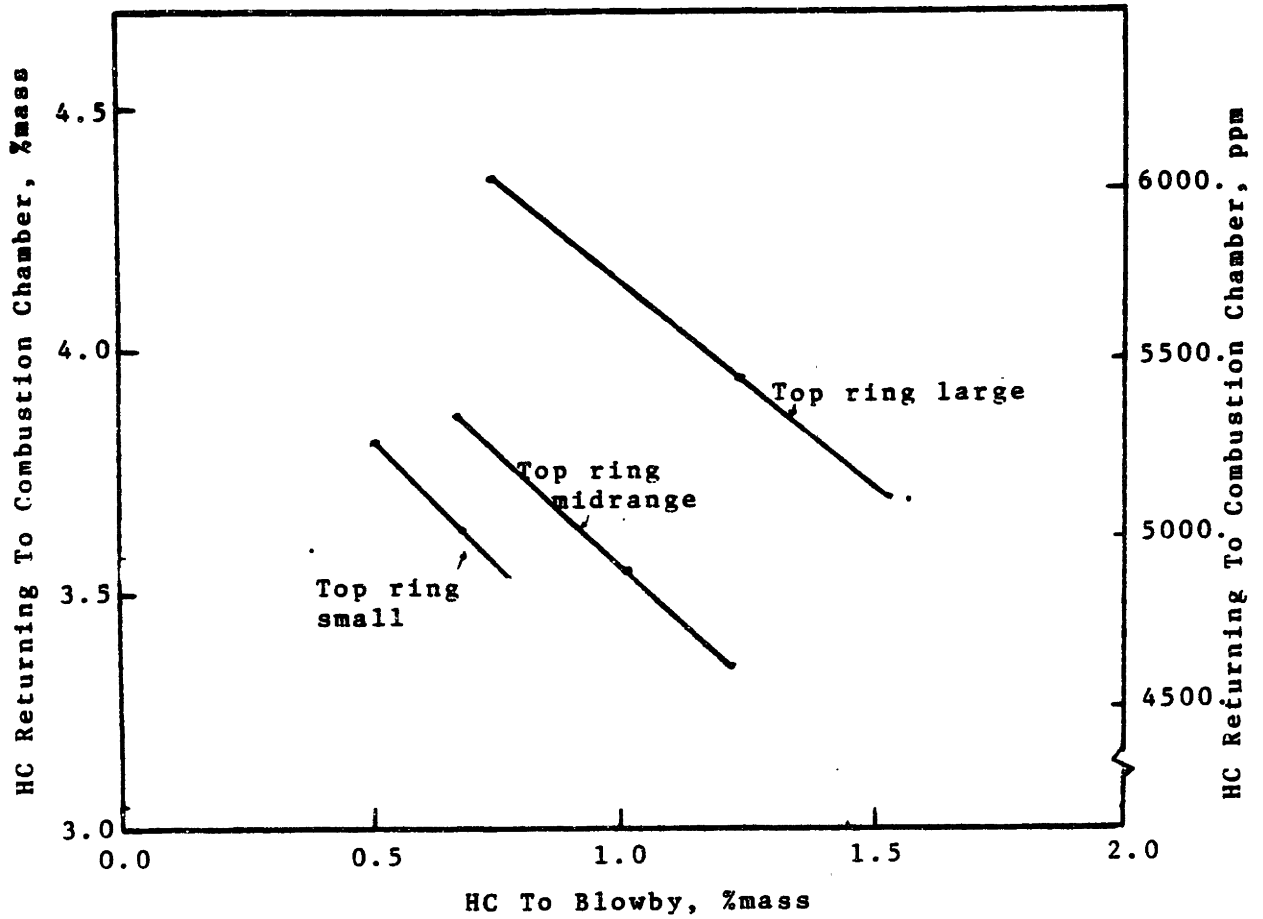
Fig 6.14 – The amount of hydrocarbon returning to the combustion chamber versus the amount that is lost to blowby.
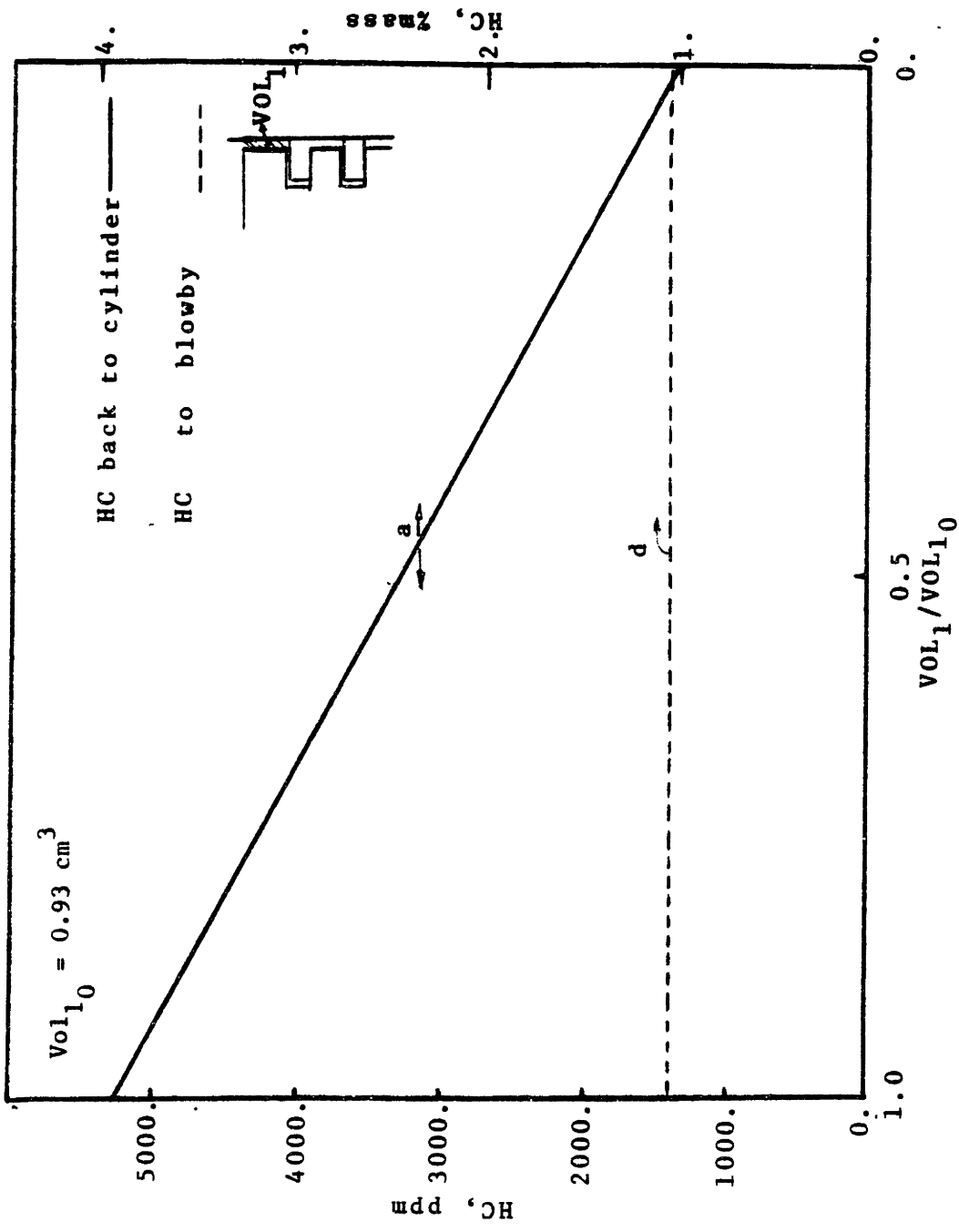
Fig 6.15 - The effect of piston top land crevice volume reduction on the amount of HC returning to the combustion chamber and the amount to blowby.

Fig 6.17 - The effect of reduction in the volumes of the regions beneath the top ring on the amount of HC returning to the combustion chamber and on the amount that is lost to blowby.
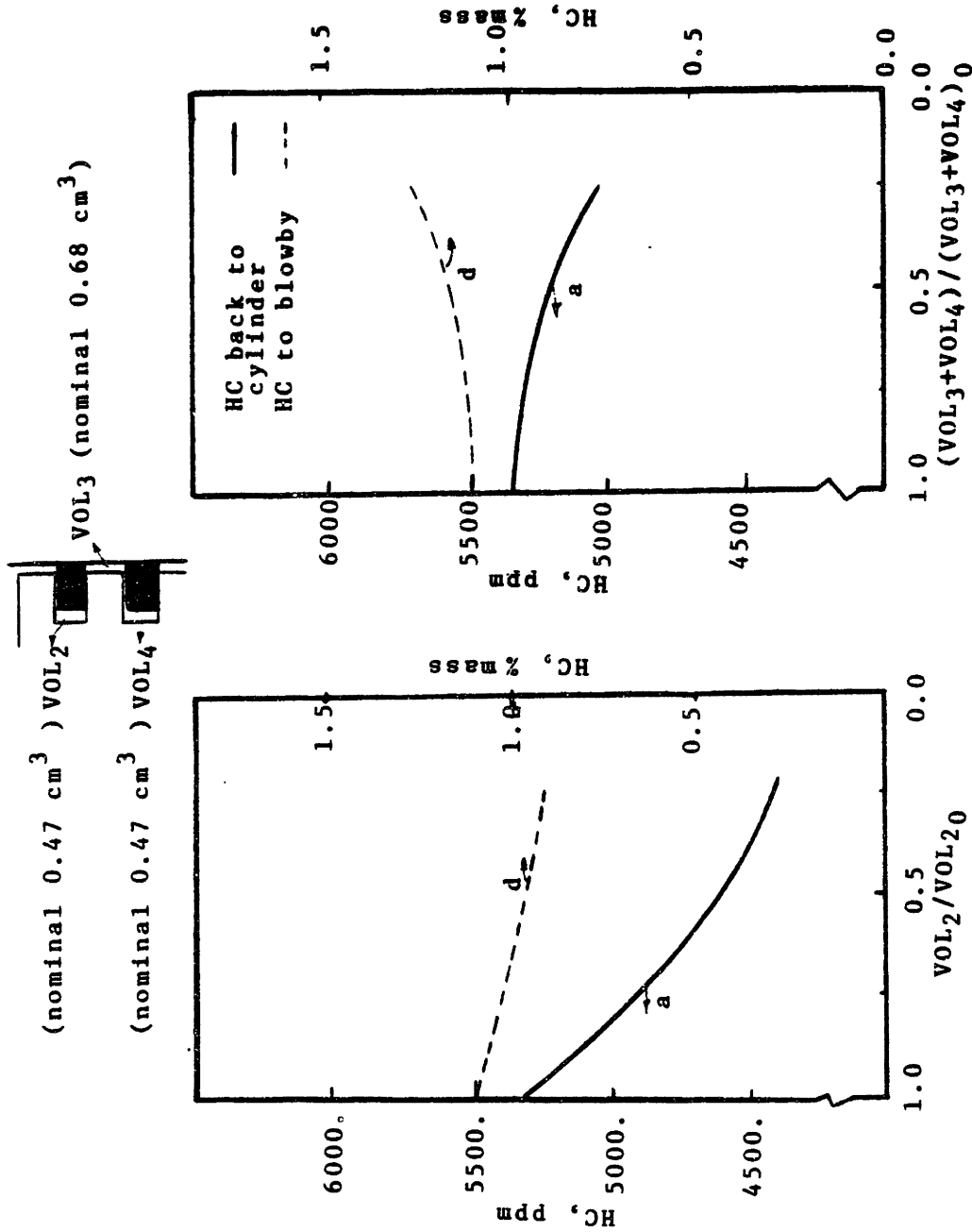
Fig 6.16 - The effect of reduction in the volume of the region behind the top ring on amount of HC returning to combustion chamber and on the amount that is lost to blowby.
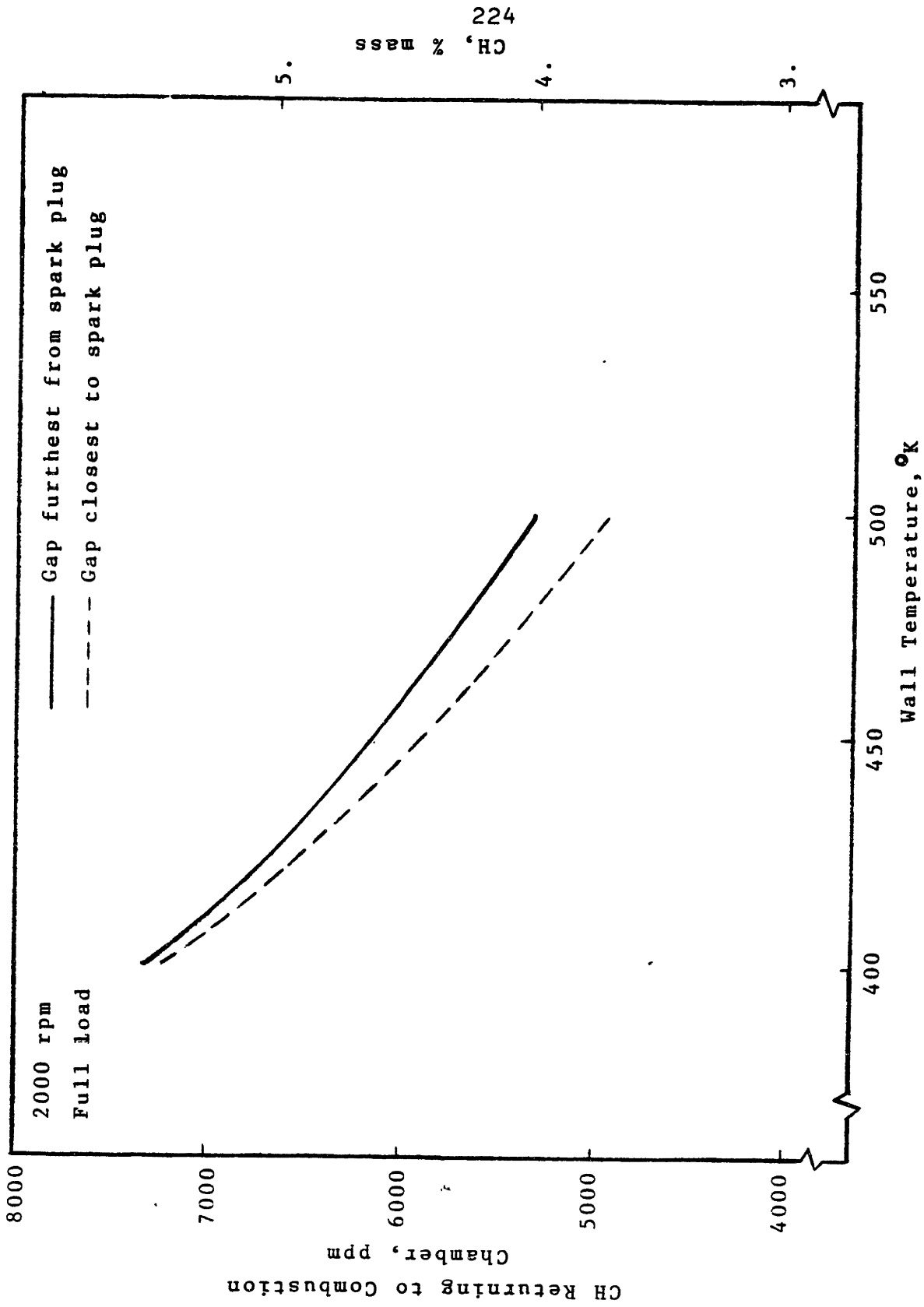
Fig 6.18a - The calculated amount of hydrocarbon returning to the combustion chamber of a V-6 engine versus wall temperature.
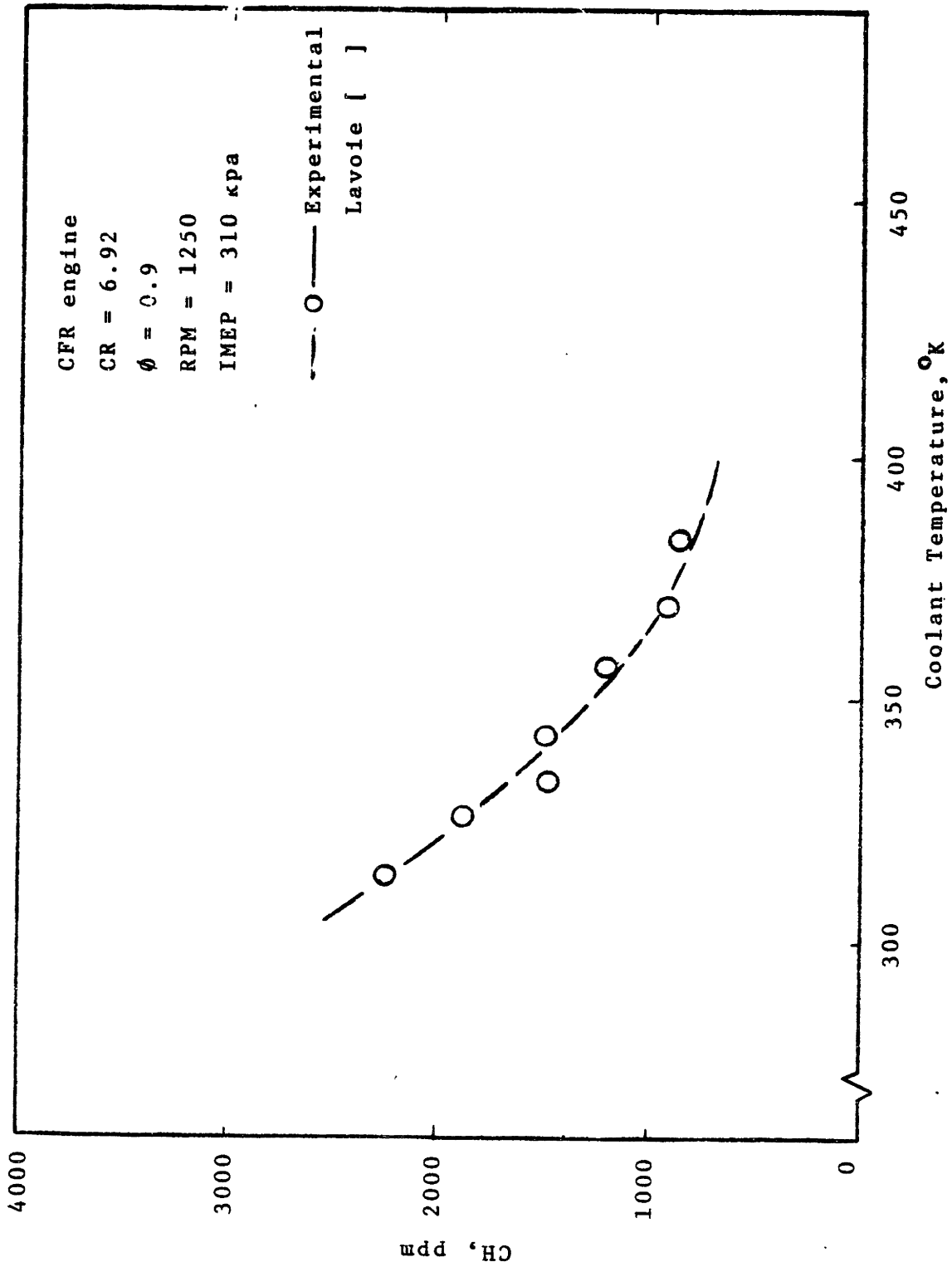
Fig 6.18b - The measured hydrocarbon of the exhaust tale of a CFR engine versus coolant temperature .
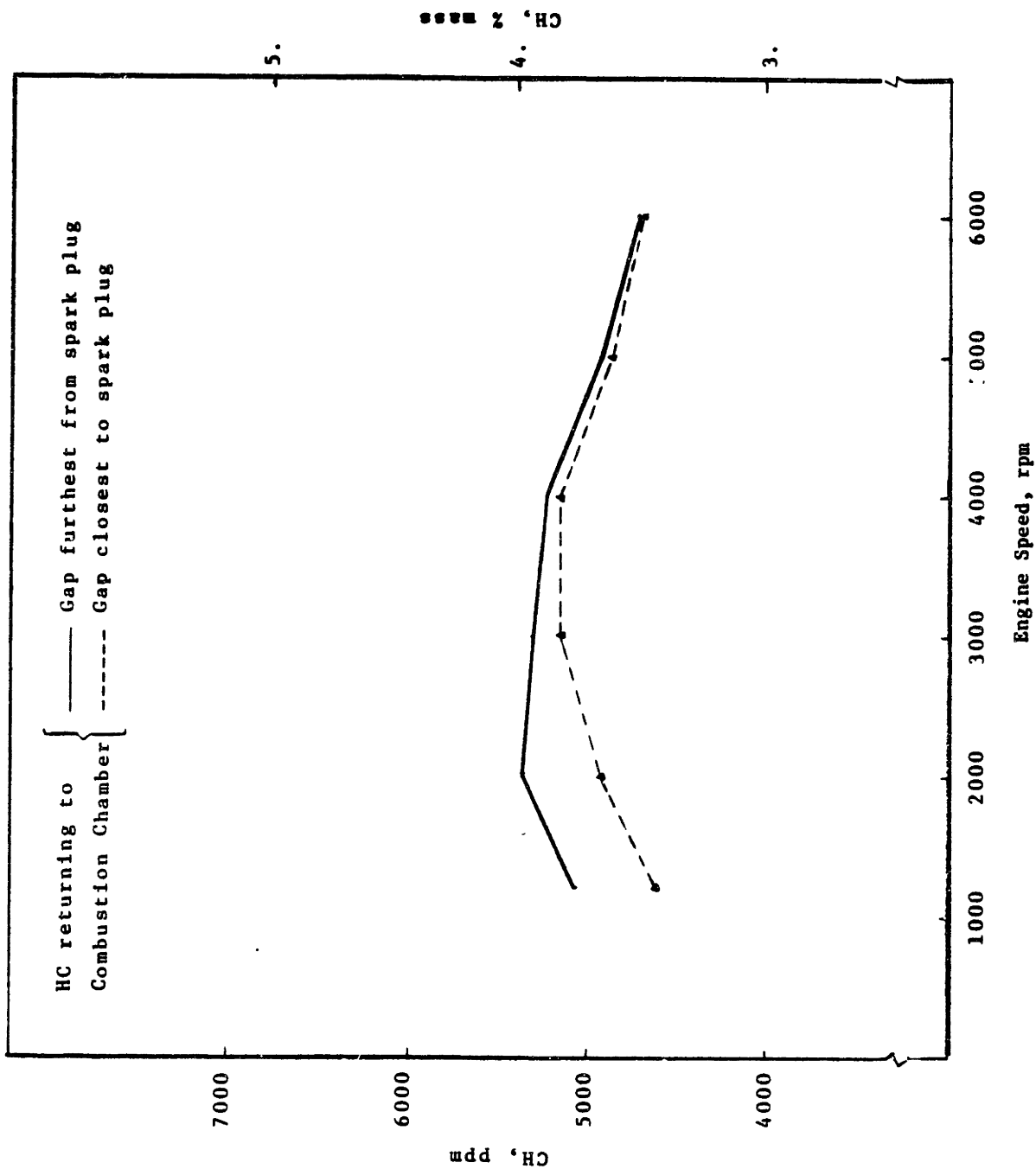
Fig 6.19 - Amount of hydrocarbon returning to combustion chamber for V-6 operating at full load.
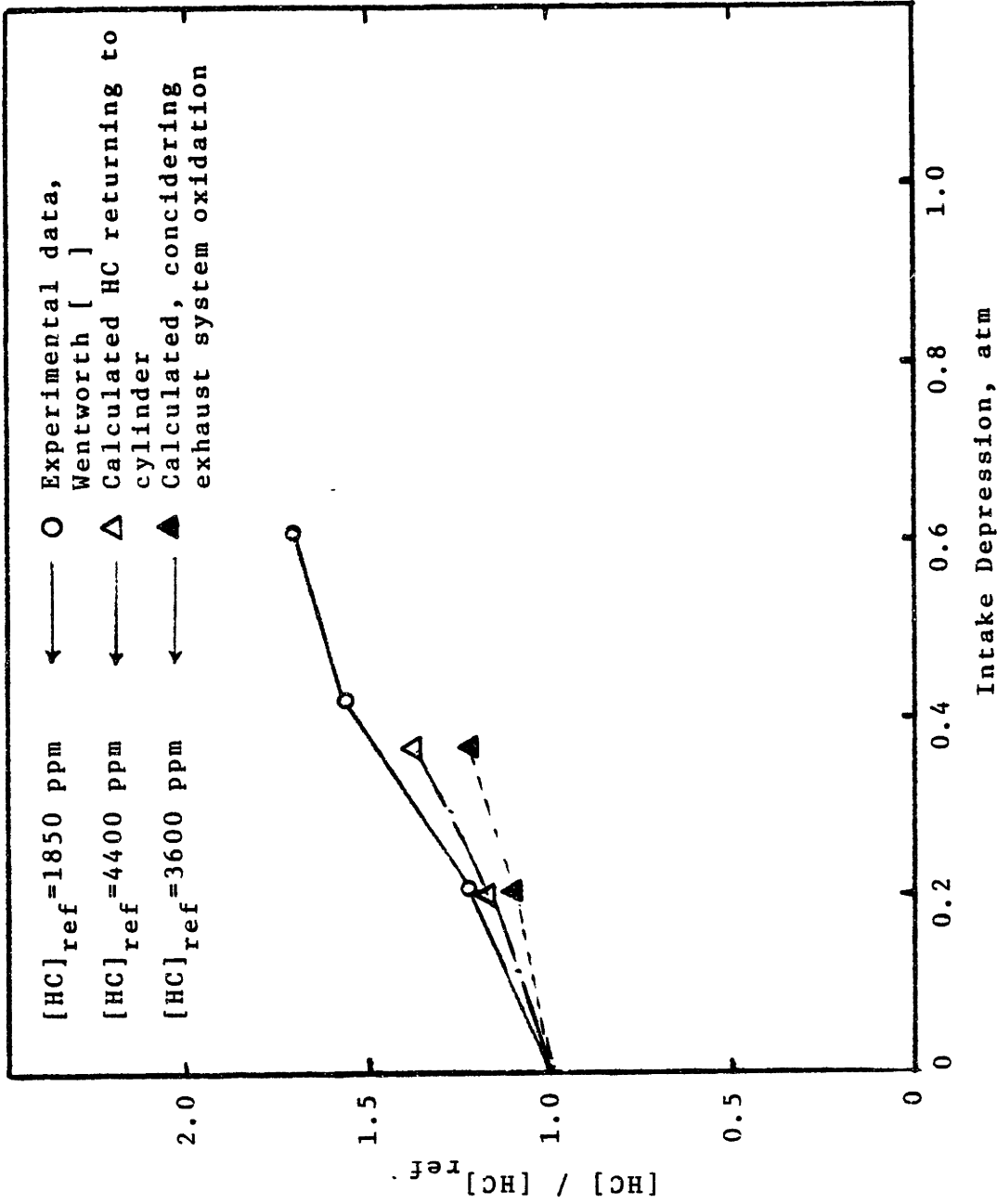
Fig 6.20 - Hydrocarbon level versus intake depression for V-6 engine . Experimental data are measured at the exhaust tale .

APPENDIX 6.1

FORCES ACTING ON A PISTON RING

To calculate the forces acting on the piston ring it is assumed that the groove surfaces are flat. The forces that act on the ring in the axial direction are:

- Pressure force F_p

- Friction force F_f

- Inertia force F_i

- Resistance of the squeezed oil F_s

Fig A6.1.1 Piston ring operating under ideal conditions (a) Piston, (b) Piston ring, (c) Cylinder liner, (d) Oil film, (e) Upper gas pressure, (f) Lower gas pressure
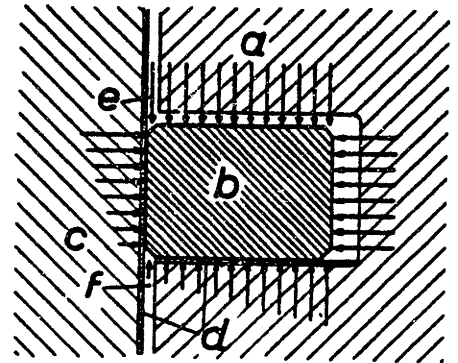
Pressure Force:

Fig A6.1.1 shows the pressure distribution around the ring [59]. The pressure force is then calculated as

$$F_p = A_r \frac{P_1 + P_2}{2} - A_r \frac{P_2 + P_3}{2} = A_r \left(\frac{P_1 - P_3}{2} \right)$$

where A_r is the ring area in radial direction.

Friction Force:

Friction force is calculated by

$$F_f = P(\pi d_r T_r) \, f$$

$$f = 4.8 \left(\frac{\mu_{oil} U_p}{P}\right)^{\frac{1}{2}} \quad [60]$$

P = pressure behind the ring

d_r = diameter of the ring in radial direction

T_r = thickness of the ring

f = friction coefficient

Inertia Force:

$$F_i = M_r a_p$$

M_r = ring mass

a_p = piston acceleration

Resistance of the Squeezed Oil:

Fig A6.1.2 shows the schematic of the squeezed oil flow. The oil volume flowrate based on Poiseuille flow is:

Fig A6.1.2 Schematic of squeezed oil flow

$$Q = - \frac{1}{12\mu_{oil}} \frac{dP}{dx} h_s^3$$

The same volume flowrate based on continuity is (for half of the ring width)

$$Q = - \frac{L_r W_r}{2} h_s^2$$

$$L_r = \text{ring length in circumference direction}$$

$$W_r = \text{ring width in radial direction}$$

Combining these two equations the pressure distribution becomes.

$$P(x) = \frac{6\mu L_r W_r \dot{h}_s}{h^3} x$$

The force due to this pressure distribution is:

$$F_s = 2\int_0^{\frac{W_r}{2}} P(x)dx$$

$$= \frac{3}{2} \mu_{oil} \; L_r \frac{dh_s}{dt} \left(\frac{W_r}{h_s}\right)^3$$

Note that only partial surface of the ring is covered by the oil [43] and hence a fraction of the above force is considered.

APPENDIX 6.2

COMPUTER PROGRAMS LISTING

This appendix contains the listing of computer programs used for the calculations described in Chapter 6.

```
C       V6.FTN
C       V6 IS FOR USE ON PDP11/60
        BYTE FILNAM(30)
        REAL MO1,NUO,NUOIL,LU,LB,LT
        COMMON /COM1/PO,ROHO,DT
        COMMON /COM2/TW,UTMOL
        COMMON /COM3/ACRV,VOL1,HSIDE,ASIDE,W
        COMMON /COM4/VOL2,VOL3,VOL4,A13,A35,6,CD,NUO
        COMMON /COM5/RCR,CONLEN,BORE,RT1,RW1,RT2,RW2,
       1 RMASS1,RMASS2,NUOIL
        COMMON /COM6/CT10,CT20,CB10,CB20,VRP1,VRP2,
       1 CT1,CT2,CB1,CB2
        COMMON /COM7/ETAV,DV
        COMMON /COM8/INTRVL,P10LD,CT10LD,CT20LD,CB10LD,CB20LD
       1 ,TOPMIN,TOPMOT,DWNMIN,DWNMOT,CMIN,CMOT,ONE3M,DOTM12
        COMMON /COM9/CRVH,DELTA,LT,B
        COMMON /COM10/FP1,FF1,FI1,FSQ1,FP2,FF2,FI2,FSQ2
        COMMON /COM11/TH,VCL
        VCL=DV/(CR-1.)
C       CALL DATA SUB PROGRAM
        CALL DATA
        WRITE(5,4)
4       FORMAT(' INLET PRESSURE PO?',$)
        READ(5,11)PO
        WRITE(5,*)' BEHIND 1ST RING;PRESSURE? PO2='
        READ(5,11)PO2
        WRITE(5,*)' BETWEEN RINGS ; PRESSURE? PO3='
        READ(5,11)PO3
        WRITE(5,*)' BEHIND 2ND RING;PRESSURE? PO4='
        READ(5,11)PO4
        WRITE(5,15)
15      FORMAT(' CRANCK CASE PRESSURE P5? ',$)
        READ(5,11)P5
        WRITE(5,8)
8       FORMAT('   RPM ?',$)
        READ(5,11)RPM
11      FORMAT(F12.5)
        WRITE(5,9)
9       FORMAT(' WHICH DATA FILE?',$)
        READ(5,10)FILNAM
10      FORMAT(30A1)
        FILNAM(30)=0
        OPEN (UNIT=3,NAME=FILNAM,TYPE='OLD',ACCESS='DIRECT'
       1 ,FORM='UNFORMATTED')
        WRITE(5,5)
5       FORMAT(' WHICH CYCLE 1 - 16?',$)
        READ(5,6)N
6       FORMAT(I3)
        READ(3'11)PO
        READ(3'1)CR
```

```
        READ(3'2)RPMBAS
        READ(3'3)BSFC
        READ(3'4)BMEP
        READ(3'5)POWER
        READ(3'6)AFRATO
        READ(3'7)AIRFLW
53      FORMAT(////////,50X,'V6 231 CUBIC INCH  BUICK ENGINE',
     1 ///2X,'CR= ',F4.2,2X,'RPM= ',F6.1,5X,'BSFC(G/KW-HR)=',F7.2
     1 ,'   BMEP(KPA)=',F7.2,'    POWER(KW)=',F6.2
     1 ,'    A/F = ',F5.2,'     AIRFLOW(GR/SEC)=',F6.4)
        WRITE(5,50)
50      FORMAT(' NAME OF MASS FRACTION BURNED FILE',/)
        READ(5,10)FILNAM
        FILNAM(30)=0
        OPEN (UNIT=4,NAME=FILNAM,TYPE='OLD',ACCESS='DIRECT'
     1 ,FORM='UNFORMATTED')
        READ(4'1)THXMIN
        READ(4'2)THXMAX
        READ(4'3)XMAX
        IXBRED=3
        WRITE(5,*) ' FILENAME.OUT?'
        READ(5,10)FILNAM
        FILNAM(30)=0
        OPEN(UNIT=2,NAME=FILNAM,TYPE='NEW')
        WRITE(5,53)CR,RPMBAS,BSFC,BMEP,POWER,AFRATO,AIRFLW
        WRITE(2,53)CR,RPMBAS,BSFC,BMEP,POWER,AFRATO,AIRFLW
        WRITE(2,54)RPM
        WRITE(5,59)VOL1,VOL2,VOL3,VOL4,A13,A35,TW,MUOIL
        WRITE(2,59)VOL1,VOL2,VOL3,VOL4,A13,A35,TW,MUOIL
59      FORMAT(1X,' VOL1(CC) VLO2  VOL3     VOL4     A13(CM2) A35    TW(K)
     1 MUOIL(N-S/M2)',/
     1 1X,4F8.3,2F10.6,F8.2,F10.8)
        OPEN(UNIT=1,NAME='RING.OUT',TYPE='NEW')
        OPEN(UNIT=7,NAME='MDOTS.OUT',TYPE='NEW')
        WRITE(1,53)CR,RPMBAS,BSFC,BMEP,POWER,AFRATO,AIRFLW
        WRITE(7,53)CR,RPMBAS,BSFC,BMEP,POWER,AFRATO,AIRFLW
        WRITE(1,57)
        WRITE(7,58)
57      FORMAT(1X,/////,3X,'TH',5X,'CT1',6X,'CT2',3X,'*',4X
     1 ,'FP1',2X,'FF1',2X,'FI1',2X,'SUMF1',2X,'FSQ1',2X,'VRP1',2X,'*'
     2 ,2X,'VRP2',2X,
     3 'FP2',2X,'FF2',2X,'FI2',2X,'FSUM2',2X,'FSQ2')
58      FORMAT(2X,'  TH DOTM12   DOTM23 DOTM34   DOTM45  DOTM
     1 13     DOTM35')
54      FORMAT(1X,//,' RPM USED=',F10.2,'COMPARE WITH ORIGINAL')
7       FORMAT('  TH    P1    P2    P3    P4  *',1X,
     1 ' CT1  CT2 *',' TOPFLW BLOWBY BURDT  UNBDOT  OUTDT'
     1 '* TPIN TPOT DNOT BNIN UBIN OUTM CHIN CMOT ONETM BIN2 ')
C   INITIALIZATION
        P2=PO2
```

```
          P3=P03
          P4=P04
          TOPMIN=0.
          P1OLD=P0
          BRNMIN=0.
          UNBMIN=0.
          TOPMOT=0.
          DWNMIN=0.
          DWNMOT=0.
          CMIN=0.
          CMOT=0.
          ONE3M=0.
          BUTO2=0.
          CRVMOT=0.
          CT1OLD=CT1
          CT2OLD=CT2
          CB1OLD=CB1
          CB2OLD=CB2
          ROHO=WTMOL*P0/82./TW
          MO1=VOL1*ROHO
          DT=60./RFM/360.*2.
C         ESTIMATE THE TIME STEP ,H, FOR RUGE-KUTTA
C         NOTE H=DT/INTRVL
          C=ROHO*VOL2/P0
          R=24*NUO*1.*RW1*2/(3.14*BORE*CT1*101325.*1000.*CT1**2)
          TUO=R*C
          NTRVL=4.*DT/TUO+1
          INTRVL=NTRVL
          IF(NTRVL.LT.4)NTRVL=4
          IF(NTVVL.GT.3)NTRVL=8
          INTRVL=NTRVL
C         NOTE ; R THE RESISTANCE IS =(P1-P2)/MDOT . . . . ASSUMED P1+P2=2.
C         SO IT IS MADE SURE THAT H IS AT LEAST 1/4 OF TIME CONSTANT
C         CALCULATE THE CHRGE MASS IN THE CYLINDER
          CHMASS=ETAV*DV*ROHO
C         CORRECT CHMASS COULD BE CALCULATED FROM THE GIVEN AIRFLOW
          CHMASS=AIRFLW*(1+1./AFRATO)/(RPMBAS/60./2.)
          WRITE(5,25)CHMASS,INTRVL
          WRITE(2,25)CHMASS,INTRVL
25        FORMAT(1X,////,10X,'TOPFLW & BLOWBY ARE IN GR/SEC',/,
         1 ///,10X,'MASSES IN & OUT OF TOP AND BOTTOM ARE IN % OF THE
         1 MASS IN THE CYLNDER WHICH IS ',F5.3,' GR',///
         1 ,10X,' NUMBER OF INTERVALS USED IN THE RUNGE KUTTA IS ',I2)
          WRITE(5,7)
          WRITE(2,7)
          J=11+(N-1)*180
          READ(3'J)P1
          DP=P0-P1
```

```
          DO 2 I=1,361
          TH=(I-1)*2-180
          IF(TH.GT.180.)GOTO38
          IS=I+10+(N-1)*180
          READ(3'IS)P1
          P1=P1+DP
38        CONTINUE
          IF(TH.GE.180..AND.TH.LT.370.)P1=1.
          IF(TH.GE.370..AND.TH.LT.540.)P1=PO
C         * * * * * * * * * * * * * * * * * * * * * * * * * * * * * * * * *
C         CALL PRESS ROUTINE TO CALCULAE THE PRESSURES OF THE REGIONS
          INTRVL=NTRVL
          IF(TH.GT.-40..AND.TH.LT.70.)INTRVL=2*NTRVL
          IF(TH.GT.-18..AND.TH.LT.30.)INTRVL=4*NTRVL
          IF(TH.GE.10..AND.TH.LT.30.)INTRVL=8*NTRVL
          CALL PRESS(P1,P2,P3,P4,P5,TOPFLW,BLOWBY)
C         CALL FORCES TO CALCULATETHE FORCES ON THE RINGS
          CALL FORCES(TH,P1,P2,P3,P4,P5,RPM,SUMF1,SUMF2)
C         NONDIMENTIONALIZE THE MASSES IN AND OUT OF REGIONS
C         THESE ARE CALCULATED IN PRESS SUBROUTINE
          TINCNT=TOPMIN/CHMASS*100.
          TOTCNT=TOPMOT/CHMASS*100.
          DOTCNT=DWNMOT/CHMASS*100.
          DINCNT=DWNMIN/CHMASS*100.
C         * * * * * * * * * * * * * *  * * * * * * * * * * * * *  * * *
C         FIND CRVICE FLOW ; PISTON CYLINDER CREVICE
          IF(TH.EQ.THXMIN)PREF=P1
          LU=LT
          IF(TH.LE.THXMIN.OR.P1.LE.P1OLD.OR.TH.GT.THXMAX)GOTO 60
          IXBRED=IXBRED+1
          READ(4'IXBRED)XB
          XB=XB/XMAX
          CALL UNBL(XB,LU,PREF,P1)
60        LB=LT-LU
          BRNDOT=LB*CRVH*DELTA*ROHO/PO*(P1-P1OLD)/DT
          UNBDOT=LU*CRVH*DELTA*ROHO/PO*(P1-P1OLD)/DT
          IF(UNBDOT.LT.0.)CRVOUT=UNBDOT
      .   IF(UNBDOT.LT.0.)UNBDOT=0.
          BTO2DT=LB/LT*DOTM12
          BUTO2=BUTO2+BTO2DT*DT
          BTO2CT=BUTO2/CHMASS*100.
          ONE3MC=ONE3M/CHMASS*100.
          BRNMIN=BRNMIN+BRNDOT*DT
          UNBMIN=UNBMIN+UNBDOT*DT
          CRVMOT=CRVMOT-CRVOUT*DT
          BINCNT=BRNMIN/CHMASS*100.
          UINCNT=UNBMIN/CHMASS*100.
          COTCNT=CRVMOT/CHMASS*100.
```

```
        CHINCT=CHIN/CHMASS*100.
        CHOTCT=CHOT/CHMASS*100.
        P1OLD=P1
        CT1MM=1000.*CT1
        CT2MM=1000.*CT2
        ITH=TH
        IF(ITH/10.EQ.TH/10.)WRITE(5,19)
        IF(ITH/10.EQ.TH/10.)WRITE(2,19)
19      FORMAT(1X,/)
        IF(TH.EQ.0.)WRITE(2,7)
        IF(TH.EQ.180.)WRITE(2,7)
        IF(TH.EQ.360.)WRITE(2,7)
        IF(TH.EQ.540.)WRITE(2,7)
        WRITE(5,20)TH,P1,P2,P3,P4,CT1MM,CT2MM,TOPFLW,BLOWBY,BRNDOT,
        1 UNBDOT,CRVOUT,TINCNT,TOTCNT,DOTCNT,BINCNT,UINCHT,COTCNT
        1 ,CHINCT,CHOTCT,ONE3HC,BTO2CT
        WRITE(2,20)TH,P1,P2,P3,P4,CT1MM,CT2MM,TOPFLW,BLOWBY,BRNDOT,
        1 UNBDOT,CRVOUT,TINCNT,TOTCNT,DOTCNT,BINCNT,UINCNT,COTCNT
        2 ,CHINCT,CHOTCT,ONE3HC,BTO2CT
20      FORMAT(1X,F6.1,3F6.2,F5.2,'*',F5.3,1X,F5.3,'*'
        1 ,2F7.3,3F7.3,'*',8F5.2,2F6.2)
        CRVOUT=0.
C       CALL RING SUBROUTINE TO FIND THE POSITION OF THE RINGS
        CALL RING(SUMF1,1)
        CALL RING(SUMF2,2)
        WRITE(1,100)TH,CT1,CT2,FP1,FF1,FI1,SUMF1,FSQ1,VRP1,VRP2
        1                   ,FP2,FF2,FI2,SUMF2,FSQ2
100     FORMAT(F7.1,2F10.6,'*',5F7.2,F7.4,'*',F7.4,5F7.2)
C       THIS STATEMENT COME INTO EFFECT WHEN /D IS USED WHEN COPILING
D       IF(CT1.GT.0..AND.CB1.GT.0.)RMODE=2.
D       IF(CT1.NE.CT10)RMODE=2.
D       IF(RMODE.EQ.2.)CT1=CT10/2.
D       CB1=CT10-CT1
2       CONTINUE
        CLOSE(UNIT=3)
        CLOSE(UNIT=4)
        CLOSE(UNIT=2)
        STOP
        END
```

```fortran
C       V6DATA.FTN
C     · DATA FOR V6 ENGINE
C       NUO M2/SEC    AREAS CM2    VOLUMS IN CC
C       ETAV IS VOLUMETRIC EFFICIENCY & DV IS DISPLACEMENT VOLUME IN CC
C       VOL1 IS PISTON CYLINDER CLEARANCE VOLUME
C       COM5 DATA ARE ALL MKS EXCEPT MUOIL ;CHECK LATER
        SUBROUTINE DATA
        REAL NUO,MUOIL,LT
        COMMON /COM2/TW,WTMOL
        COMMON /COM3/ACRV,VOL1,HSIDE,ASIDE,W
        COMMON /COM4/VOL2,VOL3,VOL4,A13,A35,G,CD,NUO
        COMMON /COM5/RCR,CONLEN,BORE,RT1,RW1,RT2 RW2,
       1 RMASS1,RMASS2,MUOIL
        COMMON /COM6/CT10,CT20,CB10,CB20,VRP1,VRP2,
       1 CT1,CT2,CB1,CB2
        COMMON /COM7/ETAV,DV
        COMMON /COM9/CRVH,DELTA,LT,B
C       DOUBLE PRECISION CT10,CB10,CT20,CB20,CT1,CT2
C       ,CB1,CB2
        DATA ACRV/.92/,VOL2/.467/,HSIDE/.005/,ASIDE/.122/,W/.32/,
       1 NUO/.000015/,WTMOL/31.5/,TW/450./
        DATA VOL3/.681/,VOL4/.467/,A13/.002613/,A35/.002614/,G/1.4/
        DATA RCR/.04318/,CONLEN/.1515/,BORE/.09652/,RT1/.00196/
       1 ,RW1/.00439/,RT2/.00196/,RW2/.00439/,RMASS1/.0163/,RMASS2/.0163/
       1 ,MUOIL/.003/
        DATA CT10/7.6E-5/,CB10/0.E00/,CT20/7.6E-5/,CB20/0.E00/
        DATA ETAV/.90/,DV/631.88/
        DATA CRVH/.638/,DELTA/.0483/
        B=100.*BORE
        LT=3.14159*B
        VOL1=CRVH*DELTA*LT
        CD=.86
        OPEN(UNIT=8,NAME='DATA.DAT',TYPE='OLD')
        READ(8,10)CRVH,DELTA,VOL2,VOL3,VOL4,A13,A35,TW
10      FORMAT(10X,F20.8)
        MUOIL=EXP(1036./(TW-173.)-9.84)
C       INITIALIZATION
        CT1=CT10
        CT2=CT20
        CB1=CB10
        CB2=CB20
        VRP1=0.
        VRP2=0.
        CLOSE(UNIT=8)
        RETURN
        END
```

```
C       RING.FTN
C   ·   TO CALCULATE POSITION OF THE RING
        SUBROUTINE RING(SUMF,IR)
        REAL MUOIL,LT
        DIMENSION YY(3),FF(3)
        COMMON /COM1/PO,ROHO,DT
        COMMON /COM5/RCR,CONLEN,BORE,RT1,RW1,RT2,RW2,
       1 RMASS1,RMASS2,MUOIL
        COMMON /COM6/CT10,CT20,CB10,CB20,VRP1,VRP2,
       1 CT1,CT2,CB1,CB2
        COMMON /COM9/CRVH,DELTA,LT,B
        COMMON /COM10/FP1,FF1,FI1,FSQ1,FP2,FF2,FI2,FSQ2
        DOUBLE PRECISION H,X
C       INITIALIZATION
        IF(IR.EQ.1)GOTO 1
        IF(IR.EQ.2)GOTO 2
1       RMASS=RMASS1
        RW=RW1
        CTO=CT10
        CT=CT1
        VRP=VRP1
        GOTO 4
2       RMASS=RMASS2
        RW=RW2
        CTO=CT20
        CT=CT2
        VRP=VRP2
4       CONTINUE
        YY1OLD=VRP
        YY2OLD=CT
        RL=3.14159*BORE
        W=RW-DELTA/100.
        INTRVL=10
        GO TO 3
8       INTRVL=2*INTRVL
3       CONTINUE
        H=DBLE(DT/FLOAT(INTRVL))
        YY(1)=YY1OLD
        YY(2)=YY2OLD
        K=0
        X=0.
        DO 20 J=1,INTRVL
        OLDY2=YY(2)
        OLDY1=YY(1)
9       CALL RUNGE(2,YY,FF,X,H,K)
        IF(OLDY2.EQ.0.)GOTO 12
        IF(INTRVL.LT.300.AND.ABS(YY(2)-OLDY2)/OLDY2*100..GT.40.)GOTO 8
12      CONTINUE
        IF(OLDY1.EQ.0.)GOTO 14
C       IF(ABS(YY(1)-OLDY1)/OLDY1*100..GT.25.)GOTO 8
```

```
      IF(ABS(SUMF).GT..9.AND.SUMF*YY(1).LT.0..AND.
   -1 INTRVL.LT.200)GOTO 9
14    CONTINUE
      IF(SUMF.GT..0.AND.YY(2).GT..95*CT0)YY(1)=.0
      IF(SUMF.GT..0.AND.YY(2).GT..95*CT0)YY(2)=CT0
      IF(SUMF.LT..0.AND.YY(2).LT..04*CT0)YY(1)=.0
      IF(SUMF.LT..0.AND.YY(2).LT..04*CT0)YY(2)=.0
      GOTO (10,15),K
10    CONTINUE
D     WRITE(5,11)YY(1),YY(2)
D11   FORMAT(2F12.6)
      IF(SUMF.LE.0.)CTB=YY(2)
      IF(SUMF.GT.0.)CTB=CT0-YY(2)
      IF(CTB.EQ.0.)GOTO 15
      FF(1)=SUMF*9.8-.1*RL*MUOIL*(W/CTB)**3.*YY(1)
      FF(1)=FF(1)/RMASS
      FF(2)=YY(1)
      GOTO 9
15    CONTINUE
20    CONTINUE
      IF(CTB.NE..0)FSQ=-.1*RL*MUOIL*(W/CTB)**3.*YY(1)
      IF(CTB.EQ..0)FSQ=.0
      IF(IR.EQ.1)CT1=YY(2)
      IF(IR.EQ.1)VRP1=YY(1)
      IF(IR.EQ.1)FSQ1=FSQ/9.8
      IF(IR.EQ.2)CT2=YY(2)
      IF(IR.EQ.2)VRP2=YY(1)
      IF(IR.EQ.2)FSQ2=FSQ/9.8
      CB1=CT10-CT1
      CB2=CT20-CT2
D     WRITE(5,7)DT,BORE,RW,RMASS,RL,VRP,MUOIL,CT0,CTB
D7    FORMAT(F15.8,6F10.5,2F10.7)
      RETURN
      END
```

```
C       FORCER.FTN
C   -   SUBROUTINE TO CALCULATE THE FORCES ACTING ON THE RING
        SUBROUTINE FORCES(TH,P1,P2,P3,P4,P5,RPM,SUMF1,SUMF2)
        REAL MUOIL
        COMMON /COM5/RCR,CONLEN,BORE,RT1,RW1,RT2,RW2,
       1 RMASS1,RMASS2,MUOIL
        COMMON /COM10/FP1,FF1,FI1,FSQ1,FP2,FF2,FI2,FSQ2
        ROOT(T)=SQRT(1.-(RCR*SIN(T)/CONLEN)**2.)
        ROOTDT(T)=-(RCR/CONLEN)**2.*SIN(T)*COS(T)/ROOT(T)
        UPP(T)=RCR*SIN(T)-CONLEN*ROOTDT(T)
        APP(T)=RCR*COS(T)*(1.+RCR/CONLEN*COS(T)/ROOT(T))
       1 +RCR**2./CONLEN*SIN(T)*
       1 (-SIN(T)*ROOT(T)-COS(T)*ROOTDT(T))/(ROOT(T))**2.
C       PISTON VELOCITY & ACCELERATION
CD      CHEK=UPP(90.*.01745)*2.*3.14*RPM/60.
CD      WRITE(5,13)RPM,CHEK
CD13     FORMAT(2F12.5)
        UP=UPP(TH*.01745)*2.*3.14*RPM/60.
        AP=APP(TH*.01745)*(2.*3.14*RPM/60.)**2.
C       FRICTION COEFFICIENTS
        FCOEF1=4.8*SQRT(MUOIL*ABS(UP)/(P2*101323.0*RT1))
        FCOEF2=4.8*SQRT(MUOIL*ABS(UP)/(P4*101323.0*RT2))
C       FRICTION FORCES
        FF1=FCOEF1*3.14*(BORE-2.*RW1)*RT1*P2*1.033*10000.
        FF2=FCOEF2*3.14*(BORE-2.*RW2)*RT2*P4*1.033*10000.
        IF(TH.GT.0..AND.TH.LT.180.)FF1=-FF1
        IF(TH.GT.360..AND.TH.LT.540.)FF1=-FF1
        IF(FF1.LT.0.)FF2=-FF2
C       PRESSURE FORCES
        FP1=3.14*(BORE-RW1)*RW1*(P1-P3)/2.*1.033*10000.
        FP2=3.14*(BORE-RW2)*RW2*(P3-P5)/2.*1.033*10000.
C       INERTIAL FORCES
        FI1=-RMASS1*AP/9.8
        FI2=-RMASS2*AP/9.8
C       SUM UP THE FORCES
        SUMF1=FP1+FF1+FI1
        SUMF2=FP2+FF2+FI2
D       WRITE(5,10)TH,UP,AP,P1,P3,FP1,FF1,FI1,SUMF1
D      1 ,FP2,FF2,FI2,SUMF2
D10     FORMAT(1X,2F6.1,F9.1,'   *',2F5.2,'   *',4F8.2,'   *',4F8.2,$)
        RETURN
        END
```

```
C       PRESSURE.FTN
C     ·  TO CALCULATE THE PRESSURE OF THE REGIONS
C       THIS SUBPROGRAM SOLVES THE THREE DIFFERENTIAL EQUATIPN
C       FOR PRESSURES IN THE RIGIONS BEHIND AND BETWEEN RINGS
C       METHOD USED IS RUNGE-KUTTA
        SUBROUTINE PRESS(P1,P2,P3,P4,P5,TOPFLW,BLOWBY)
        DIMENSION Y(3),F(3)
        DOUBLE PRECISION X1,X2,X3,X4,X5,X6,X7,X,XOLD,H
        REAL NUO,MUOIL,HO2,HO3,HO4
        COMMON/COM1/PO,ROHO,DT
        COMMON /COM4/VOL2,VOL3,VOL4,A13,A35,G,CD,NUO
        COMMON /COM5/RCR,CONLEN,BORE,RT1,RW1,RT2,RW2,
       1 RMASS1,RMASS2,MUOIL
        COMMON /COM6/CT10,CT20,CB10,CB20,VRP1,VRP2,
       1 CT1,CT2,CB1,CB2
        COMMON /COM8/INTRVL,P1OLD,CT10LD,CT20LD,CB10LD,CB20LD
       1 ,TOPMIN,TOPMOT,DWNMIN,DWNMOT,CMIN,CMOT,ONE3M,DOTM12
        COMMON /COM11/TH,VCL
        FLOW(SIDE,PUP,PDOWN,W)=3.14*BORE*(SIDE*(PUP**2.-PDOWN**2.))/
       1 (24.*NUO*1.*W)*(101325.*SIDE*1000.*SIDE)
C       INITIALIZATION
C       H; AN INDEX USED IN RUNGE
C       X; INDEPENDENT VARIABLE I.E. TIME ...
C       H; TIME INTERVAL USED IN RUNGE; NOTE H IS A FRACTION OF DT
C       Y(I); VECTOR OF DEPENFENT VARIABLES
C       F(I); VECTOR OF DERIVATIVES
        GOTO 4
5       INTRVL=2*INTRVL
D       WRITE(5,3)INTRVL
03      FORMAT('   NEW INTRVL=  ',I3)
4       H=0
        X=0.
        XOLD=0,
        Y1OLD=P2
        Y2OLD=P3
        Y3OLD=P4
        Y(1)=P2
        Y(2)=P3
        Y(3)=P4
        E1CMAX=0.
        E2CMAX=0.
        E3CMAX=0.
        F1SUM=0
        F2SUM=0.
        F3SUM=0.
        P3OLD=P3
        P4OLD=P4
        P2OLD=P2
        X1=0.
```

```
          X2=0,
        . X3=0,
          X4=0,
          X5=0,
          X6=0,
          X7=0,
          H=DT/INTRVL
C         INITIAL MASSES IN THE REGIONS
          MO2=VOL2*ROHO
          MO3=VOL3*ROHO
          MO4=VOL4*ROHO
          DO 7 I=1,INTRVL
6         CALL RUNGE(3,Y,F,X,H,M,K)
          GOTO (10,20),K
C         TO CALCULATE THE DERIVATIVES FIND MASS FLOWS
C         FIRST INTERPOLATE, LINEARLY, THE NECESSARY VALUES
10        CONTINUE
          PINTVL=P1OLD+X/DT*(P1-P1OLD)
          CT11=CT1OLD+X/DT*(CT1-CT1OLD)
          CT22=CT2OLD+X/DT*(CT2-CT2OLD)
          CB11=CB1OLD+X/DT*(CB1-CB1OLD)
          CB22=CB2OLD+X/DT*(CB2-CB2OLD)
D         WRITE(5,15)DT,X,PINTVL,Y(1),Y(2),Y(3)
D15       FORMAT(2F15.10,4F15.3)
C         CONTROL THE ERROR
C         IF(ABS(Y1OLD-Y(1))/Y1OLD.GT..05) GOTO 5
C         IF(ABS(Y2OLD-Y(2))/Y2OLD.GT..10) GOTO 5
C         IF(ABS(Y3OLD-Y(3))/Y3OLD.GT..10) GOTO 5
          Y1OLD=Y(1)
          Y2OLD=Y(2)
          Y3OLD=Y(3)
C         ANOTHER ERROR CHECK ON CONTINUTY OF P2 REGION
          F1SUM=F1SUM+F(1)*(X-XOLD)
          F2SUM=F2SUM+F(2)*(X-XOLD)
          F3SUM=F3SUM+F(3)*(X-XOLD)
          ERROR=Y(1)-P2OLD-F1SUM
          ERRORC=ERROR/P2OLD*100.
          E2=Y(2)-P3OLD-F2SUM
          E3=Y(3)-P4OLD-F3SUM
          E2C=E2/P3OLD*100.
          E3C=E3/P4OLD*100.
          IF(INTRVL.GT.200)GOTO 23
          IF(ABS(ERRORC).GT.1.)GOTO 5
          IF(ABS(E2C).GT.1.)GOTO5
          IF(ABS(E3C).GT.1.)GOTO 5
23        CONTINUE
C         WRITE(5,16)X,PINTVL,Y(1),Y(2),Y(3),ERRORC,E2C,E3C,DOTM13,
C         1 DOTM35,DOTM34
          E1CMAX=AMAX1(ABS(ERRORC),E1CMAX)
          E2CMAX=AMAX1(ABS(E2C),E2CMAX)
          E3CMAX=AMAX1(ABS(E3C),E3CMAX)
C16       FORMAT(F12.10,4F10.3,3F8.2,3F8.4)
```

```
          CALL MDOT(PINTVL,Y(2),DOTM13)
          DOTM13=DOTM13*A13
          CALL MDOT(Y(2),P5,DOTM35)
          DOTM35=DOTM35*A35
          DOTM12=FLOW(CT11,PINTVL,Y(1),RW1)
          DOTM23=FLOW(CB11,Y(1),Y(2),RW1)
          DOTM34=FLOW(CT22,Y(2),Y(3),RW2)
          DOTM45=FLOW(CB22,Y(3),P5,RW2)
          CHK12=DOTM12
          IF(CT11.GT..0.AND.CB11.GT.0.
         1 .AND.(P1.GT.1.5.OR.Y(1).GT.1.5))GOTO 33
          GOTO 34
33        CALL MDOT(PINTVL,Y(1),DOTM12)
          DOTM12=.6*3.14*BORE*(CT11*10000.)*DOTM12
          CALL MDOT(Y(1),Y(2),DOTM23)
          DOTM23=.6*3.14*BORE*(CB11*10000.)*DOTM23
34        IF(Y(2).GT.1.5.AND.CT22.GT.0..AND.CB22.GT.0.)GOTO 36
          GOTO 35
36        CALL MDOT(Y(2),Y(3),DOTM34)
          DOTM34=.6*3.14*BORE*(CT22*10000.)*DOTM34
          CALL MDOT(Y(3),P5,DOTM45)
          DOTM45=.6*3.14*BORE*(CB22*10000.)*DOTM45
35        CONTINUE
C         F(1)=DP2/DT
          F(1)=P0/M02*(DOTM12-DOTM23)
          F(2)=P0/M03*(DOTM13+DOTM23-DOTM34-DOTM35)
          F(3)=P0/M04*(DOTM34-DOTM45)
          TOPFLW=DOTM12+DOTM13
          BLOWBY=DOTM35+DOTM45
          FLOWC=DOTM13+DOTM23
          IF(TOPFLW.GT.0.)X1=X1+TOPFLW*(X-XOLD)
          IF(TOPFLW.LT.0.)X2=X2-TOPFLW*(X-XOLD)
          IF(BLOWBY.GT.0.)X3=X3+BLOWBY*(X-XOLD)
          IF(BLOWBY.LT.0.)X4=X4-BLOWBY*(X-XOLD)
          IF(FLOWC.GT.0.)X5=X5+FLOWC*(X-XOLD)
          IF(FLOWC.LT.0.)X6=X6-FLOWC*(X-XOLD)
          X7=X7+DOTM13*(X-XOLD)
          XOLD=X
C         ERRORC=ERROR/P2OLD*100.
C         WRITE(5,30)ERROR,ERRORC,F(1),F1SUM
C30       FORMAT(4F15.5)
          GOTO 6
C         CALCULATE THE BLOWUP & BLOWBY MASSES
20        CONTINUE
C         CALL MDOT(PINTVL,Y(2),DOTM13)
C         IF(BLOWBY.LT.0.)X4=X4-BLOWBY*H
7         CONTINUE
C         WHEN OUT OF DO LOOP ONE DT IS MARCHED;ASSAIGN P2,P3,P4
```

```
         P2=Y(1)
       . P3=Y(2)
         P4=Y(3)
C        ASSAIGN THE OLD VALUES FOR NEXT DT
C        P1OLD IS CHANGED IN MAIN
         CT1OLD=CT1
         CT2OLD=CT2
         CB1OLD=CB1
         CB2OLD=CB2
C        ADD THE NEW MASS FLOW TO THE PREVIOUS ONE
         TOPMIN=TOPMIN+X1
         TOPMOT=TOPMOT+X2
         DWNMOT=DWNMOT+X3
         DWNMIN=DWNMIN+X4
         CMIN=X5+CMIN
         CMOT=X6+CMOT
         ONE3M=ONE3M+X7
         WRITE(7,100)TH,DOTM12,DOTM23,DOTM34,DOTM45,DOTM13,DOTM35
100      FORMAT(F7.2,6F10.6)
         RETURN
         END
```

```
C       UNBL.FTN
C       TO CALCULATE THE PORTION OF THE TOP LAND CREVICE
C       WHICH IS EXPOSED TO UNBURNED GAS
        SUBROUTINE UNBL(XB,LU,PREF,P1)
        REAL LU,LT
        COMMON /COM9/CRVH,DELTA,LT,B
        TOWPI=2.*3.14159265
        GAMA=TOWPI*(1.-XB)/(P1/PREF)**.714
        DO 10 J=1,361
        JJ=361-J
        BETA=JJ*TOWPI/360.
        IF((BETA-SIN(BETA)).LE.GAMA)GOTO 20
10      CONTINUE
20      LU=B*BETA/2
        RETURN
        END
```

```
C       RUNGE.FTN
    -   SUBROUTINE RUNGE(N1,Y,F,X,H,M,K)
C       THIS ROUTINE PERFORMS RUNGE-KUTTA CALCULATION BY GILLS METHOD
C       THE CODE IS TAKEN FROM VISCOUS FLUID FLOW; FRANK WHITE
        DIMENSION Y(3),F(3),Q(3)
        DOUBLE PRECISION H,X
        M=M+1
        GOTO (1,4,5,3,7),M
1       DO 2 I=1,N1
2       Q(I)=0.
        A=.5
        GOTO 9
3       A=1.707107
4       X=X+.5*H
5       DO 6 I=1,N1
        Y(I)=Y(I)+A*(F(I)*H-Q(I))
6       Q(I)=2.*A*H*F(I)+(1.-3.*A)*Q(I)
        A=.2928932
        GOTO 9
7       DO 8 I=1,N1
8       Y(I)=Y(I)+H*F(I)/6.-Q(I)/3.
        M=0
        K=2
        GOTO 10
9       K=1
10      RETURN
        END
```

```
C       MDOTNW.FTN
C    -  SUBROUTINE MDOT CALCULATES THE MASS FLOW THROUGH THE ORIFICE
C       CARE; MDOT RETURNED FROM THIS PROGRAM IS PER UNIT AREA(CM**2)
        SUBROUTINE MDOT(PP1,PP2,DOTM)
        REAL NUO
        COMMON /COM1/PO,ROHO,DT
        COMMON /COM2/TW,WTMOL
        COMMON/COM4/VOL2,VOL3,VOL4,A13,A35,G,CD,NUO
        ROHISO(PP)=PP/PO*ROHO
        CISO(PP)=SQRT(G*8.3*1000.*TW/WTMOL)*100.
C       NO AREA IN MDOT
        ETA(PH,PL)=SQRT(2./(G-1.)*((PH/PL)**(2./G)-(PH/PL)**((G+1.)/G)))
        DMDOT(P11,P22)=CD*ROHISO(AMAX1(P11,P22))
      1 *CISO(AMAX1(P11,P22))*ETA(AMIN1(P11,P22),AMAX1(P11,P22))
        DOTM=DMDOT(PP1,PP2)
        IF(AMIN1(PP1,PP2)/AMAX1(PP1,PP2).LE.0.5)
      1 DOTM=DOTM*.57/ETA(AMIN1(PP1,PP2),AMAX1(PP1,PP2))
        IF(PP2.GT.PP1)DOTM=-DOTM
        RETURN
        END
```